

Mean spherical approximation algorithm for multicomponent multiYukawa fluid mixtures: Study of vapor–liquid, liquid–liquid, and fluid–glass transitions

E. Arrieta, C. Jedrzejek, and K. N. Marsh

Citation: *The Journal of Chemical Physics* **95**, 6806 (1991); doi: 10.1063/1.461493

View online: <http://dx.doi.org/10.1063/1.461493>

View Table of Contents: <http://scitation.aip.org/content/aip/journal/jcp/95/9?ver=pdfcov>

Published by the [AIP Publishing](#)

Articles you may be interested in

[Solution of the mean spherical approximation for polydisperse multi-Yukawa hard-sphere fluid mixture using orthogonal polynomial expansions](#)

J. Chem. Phys. **124**, 114509 (2006); 10.1063/1.2176677

[First-order mean spherical approximation for attractive, repulsive, and multi-Yukawa potentials](#)

J. Chem. Phys. **122**, 184505 (2005); 10.1063/1.1895720

[Solution of the associative mean spherical approximation for a multicomponent dimerizing hard-sphere multi-Yukawa fluid](#)

J. Chem. Phys. **113**, 1135 (2000); 10.1063/1.481892

[Thermodynamic properties of an asymmetric fluid mixture with Yukawa interaction in the mean spherical approximation](#)

J. Chem. Phys. **105**, 9288 (1996); 10.1063/1.472759

[Monte Carlo results for binary multiYukawa mixtures. Evaluation of the accuracy of the mean spherical approximation for realistic hardcore potentials](#)

J. Chem. Phys. **95**, 6838 (1991); 10.1063/1.461494



Mean spherical approximation algorithm for multicomponent multi-Yukawa fluid mixtures: Study of vapor–liquid, liquid–liquid, and fluid–glass transitions

E. Arrieta

Department of Chemical Engineering, Texas A&M University, College Station, Texas 77843

C. Jedrzejek

Department of Physics, Jagellonian University, Cracow, Poland

K. N. Marsh

Thermodynamics Research Center, Texas A&M University, College Station, Texas 77843

(Received 18 July 1990; accepted 2 July 1991)

An efficient algorithm is given to find the Blum and Høye mean spherical approximation (MSA) solution for mixtures of hard-core fluids with multi-Yukawa interactions. The initial estimation of the variables is based on the asymptotic high-temperature behavior of the fluid. From this initial estimate only a few Newton–Raphson iterations are required to reach the final solution. The algorithm consistently yields the unique thermodynamically stable solution, whenever it exists, i.e., whenever the fluid appears as a single, homogeneous phase. For conditions in which no single phase can appear, the algorithm will declare the absence of solutions or, less often, produce thermodynamically unstable solutions. A simple criterion reveals the instability of those solutions. Furthermore, this Yukawa-MSA algorithm can be used in a most simple way to estimate the onset of thermodynamic instability and to predict the nature of the resulting phase separation (whether vapor–liquid or liquid–liquid). Specific results are presented for two binary multi-Yukawa mixtures. For both mixtures, the Yukawa interaction parameters were adjusted to fit, beyond the hard-core diameters σ , Lennard-Jones potentials. Therefore the potentials studied, although strictly negative, included a significant repulsion interval. The characteristics of the first mixture were chosen to produce a nearly ideal solution, while those of the second mixture favored strong deviations from ideality. The MSA algorithm was able to reflect correctly their molecular characteristics into the appropriate macroscopic behavior, reproducing not only vapor–liquid equilibrium but also liquid–liquid separations. Finally, the high-density limit of the fluid phase was determined by requiring the radial distribution function to be non-negative. A case is made for interpreting that limit as the fluid–glass transition.

I. INTRODUCTION

In a recent article, Rowlinson¹ analyzes the mathematical properties of the Yukawa potential and explains why those properties enable it to describe a variety of physical phenomena. The property of interest here is that the screened Coulomb (or damped exponential) form of the Yukawa potential allows, in the mean spherical approximation (MSA), an almost analytic solution of the Ornstein–Zernike² equation.

This simple solution provided by the Yukawa-MSA combination allows thermodynamicists to put into practical use the theoretical advantages of statistical mechanics over the traditional equation-of-state (EOS) approach. These advantages include a better, more direct description of dense fluids, independence from empirical mixing rules, and an essentially predictive nature (as opposed to the correlative spirit of EOS).

The immediate objective of this work is to develop the Yukawa-MSA method into a practical tool for the study of simple fluids and to provide a qualitative physical interpretation for its numerical results. The ultimate objective is to offer an alternative to classical EOS for engineering applica-

tions involving fluid mixtures such as natural gas. A subsequent paper will investigate the quantitative accuracy of the Yukawa-MSA method by comparison to Monte Carlo simulations.

The MSA equations for mixtures of Yukawa fluids were first formulated, from a theoretical standpoint, by Blum and Høye (BH).³ Their analysis showed how to transform the problem into a system of nonlinear equations. Ginoza⁴ simplified those equations and studied their properties. For the simplest case (binary one-Yukawa mixtures), the first numerical results of the BH equations were obtained by Giunta, Abramo, and Caccamo.⁵ They applied a slow, step-wise solution scheme which made their procedure rather cumbersome even for mixtures with very short-ranged interactions, for which the nonlinear equations become almost linear. Also for one-Yukawa mixtures, Arrieta, Jedrzejek, and Marsh⁶ provided a general, direct solution algorithm.

Here the work of Arrieta, Jedrzejek, and Marsh⁶ is extended by presenting an efficient, reliable solution algorithm for the most general case of the BH equations: multicomponent mixtures interacting through any number of Yukawa tails, both attractive and repulsive. This algorithm is quasianalytic in that its only numerical part, the solution of a

system of nonlinear equations, takes just a few iterations to yield the unique, stable solution, whenever such a solution exists.

The Yukawa interaction is composed of a linear combination of several terms, called "tails", which decrease exponentially with intermolecular distance. The simplest case consists of one Yukawa tail, whose form, beyond the hard-core diameter σ , is given by $\phi(r) = -\sigma\epsilon \exp[-z(r - \sigma)]/r$. Although a hard core plus one attractive Yukawa tail account for the basic elements in real potentials (short-range repulsion and long-range attraction), they combine those elements in an obviously artificial way (the infinite repulsion of the hard core is joined by the Yukawa potential at its most strongly attractive point). This undesirable characteristic can be avoided through the use of multiple Yukawa tails. By the appropriate choice of the hard-core diameter and combination of sufficient attractive and repulsive Yukawa tails, any smooth, realistic isotropic potential can be reproduced with arbitrary accuracy (within a given distance range).

However, the reliability of the MSA for any such combined potential is not guaranteed. It is well known that the MSA fails for significantly positive (repulsive) potentials. This can be best seen in the zero density limit. In this case, for a given interaction potential $\phi(r)$, the exact radial distribution function (RDF), Eq. (1) below, is approximated in the MSA by Eq. (2),

$$\text{exact } g(r) = \exp[-\phi(r)/kT] \quad (\rho = 0), \quad (1)$$

$$\text{MSA } g(r) = 1 - \phi(r)/kT \quad (\rho = 0). \quad (2)$$

Thus positive potentials may lead, in the MSA, to negative RDFs—a nonphysical result.

On the other hand, the MSA is known to yield accurate thermodynamic properties for hard-core components with purely attractive soft interactions. This accuracy has been established for pure components by Henderson *et al.*⁷ (one-Yukawa potential), by Stell and Weis⁸ [hard-core attractive Lennard-Jones, $\phi(r) = -\epsilon^{LJ}$ for $\sigma \leq r \leq r_{\min}$], and by Konior and Jedrzejek⁹ (two-Yukawa fitted to the Lennard-Jones interaction used by Stell and Weis).

This work investigates the validity of the MSA for binary mixtures with an intermediate type of potential. Positive values of the interaction potential are avoided altogether, substituting them with hard cores; however, the potential includes a significant repulsion (negative slope) interval. Specifically, three- and four-Yukawa interactions are fitted to two different truncated Lennard-Jones [$\phi_{ij}(r) = \infty$ for $r < \sigma_{ij}$, $\phi_{ij}(r) = \phi_{ij}^{LJ}(r)$ for $r \geq \sigma_{ij}$] mixtures. The characteristics of these two mixtures are selected to provide a thorough qualitative test for the Yukawa-MSA algorithm. In the first mixture, the ratios σ_{22}/σ_{11} and $\epsilon_{22}^{LJ}/\epsilon_{11}^{LJ}$, with Lorentz-Berthelot combining rules [$\sigma_{12} = \frac{1}{2}(\sigma_{11} + \sigma_{22})$, $\epsilon_{12}^{LJ} = \sqrt{\epsilon_{11}^{LJ}\epsilon_{22}^{LJ}}$], are chosen to produce a fairly ideal mixture resembling argon-xenon. In contrast, the components of the second mixture have a large size difference, and a relatively weak cross interaction is chosen to induce a tendency towards liquid-liquid phase separation.

Section II presents the BH equations for multicomponent multi-Yukawa mixtures, indicating how to transform

the original three-dimensional, integrodifferential equations in functional unknowns into a system of ordinary, algebraic, nonlinear equations. Section III gives the solution procedure, discusses its efficiency, and examines the physical meaning of the lack of real solutions for certain thermodynamic conditions. Based on the shape of the regions of no solution, an immediate qualitative difference can be established between ideal and nonideal mixtures. Section III also includes a sample of numerical results obtained for the two mixtures studied here. In Sec. IV the correlation coefficients are calculated and analytic expressions are given for the MSA thermodynamic properties. Section V analyzes the thermodynamic stability of the results provided by the MSA algorithm. Under some conditions, the fluid cannot appear as a single, homogeneous phase. In such a case, the algorithm may yield an unstable solution; a simple criterion is given to detect these nonphysical solutions. For stable solutions, the algorithm indicates proximity of a phase separation and of the nature of such a separation (whether vapor-liquid or liquid-liquid). This information can be used to great advantage in equilibrium calculations. Section VI determines the high density limits beyond which the MSA yields nonphysical results. The most important of these limits corresponds to a zero value for the first depression of the radial distribution function. A case is made for interpreting that limit as the second order transition from (metastable) liquid to glass. Finally, Sec. VII presents a summary of conclusions.

In addition, Appendix A gives explicit expressions for the coefficients needed to obtain the MSA solutions. Appendix B presents the MSA energy-derived second virial coefficients for the mixtures studied here. Appendix C calculates some quantities needed in the computation of pressures. Appendix D provides a simple algorithm for the pointwise calculation of radial distribution functions; this algorithm is based on Perram's method¹⁰ for hard spheres. Last, a theoretical analysis in Appendix E shows that for any Yukawa tail ν for which the cross interactions satisfy the condition $K_{vij} = \pm \sqrt{K_{vii}K_{vjj}}$, (see Sec. II), the coefficients D_{vij} of the factor correlation functions outside the core are related according to $D_{v1i}/K_{v1i} = D_{v2i}/K_{v2i} = \dots = D_{vni}/K_{vni}$, for $i = 1, 2, \dots, n$ (n being the number of chemical species in the mixture). This relation is specific to each tail ν , and does not require that the K_{rij} parameters of other Yukawa tails $\tau \neq \nu$ satisfy the same condition.

II. BLUM AND HØYE'S YUKAWA-MSA EQUATIONS

The interaction potential for a mixture of hard spheres of diameter σ_i with ω Yukawa tails outside the core is

$$\phi_{ij}(r) = \begin{cases} \infty & \text{for } r < \sigma_{ij}, \\ -\sigma_{ij} \sum_{\nu=1}^{\omega} \epsilon_{vij} \frac{e^{-z_{\nu}(r-\sigma_{ij})}}{r} & \text{for } r \geq \sigma_{ij}, \end{cases} \quad (3)$$

where $\sigma_{ij} = \frac{1}{2}(\sigma_i + \sigma_j)$ (the additive hard-core assumption), ϵ_{vij} are the magnitudes of the interactions at the hard-core distances, and for each Yukawa tail ν (Greek subindices will be used to designate the different tails) the

exponent, or inverse range parameter, z_v is common for all i, j pairs.

In the mean spherical approximation (MSA) the Ornstein-Zernike (OZ) equation for mixtures

$$h_{ij}(r) = c_{ij}(r) + \sum_l \rho_l \int c_{il}(s) h_{lj}(|r-s|) ds, \quad (4)$$

is given the following two-part closure:

$$h_{ij}(r) = -1 \quad \text{for } r < \sigma_{ij}, \quad (5)$$

$$c_{ij}(r) = \sum_{v=1}^{\omega} K_{vij} \frac{e^{-z_v(r-\sigma_{ij})}}{r} \quad \text{for } r \geq \sigma_{ij}, \quad (6)$$

where Eq. (5) reflects the impenetrability of the hard cores and Eq. (6) accounts for the influence of the interaction potential outside the cores, with

$$K_{vij} = \frac{\sigma_{ij} \epsilon_{vij}}{kT}. \quad (7)$$

In these equations, $h_{ij}(r) = g_{ij}(r) - 1$ are the total correlation functions (TCF), $g_{ij}(r)$ are the two-body radial distribution functions (RDF) between particles of species i and j , and $c_{ij}(r)$ are the direct correlation functions (DCF). The densities of the components in the mixture are represented by ρ_i . In Eq. (7) k is Boltzmann's constant and T is the temperature. One can also disregard Eq. (7) and treat Eqs. (5) and (6) as a generalized mean-spherical-approximation (GMSA) closure.

To calculate the thermodynamic properties of this mix-

ture, the total number density ρ , composition x_i (or, alternatively, the number densities of the components $\rho_i = \rho x_i$) and temperature T must be specified.

Using Baxter's factorization,¹¹ in Blum and Høye's version,³ the OZ equation² for mixtures becomes

$$\begin{aligned} 2\pi r c_{ij}(r) &= -Q'_{ij}(r) \\ &+ \sum_l \rho_l \int_{\lambda_{jl}}^{\infty} Q_{jl}(t) Q'_{il}(r+t) dt, \\ 2\pi r h_{ij}(r) &= -Q'_{ij}(r) \\ &+ 2\pi \sum_l \rho_l \int_{\lambda_{jl}}^{\infty} (r-t) h_{il}(|r-t|) Q_{lj}(t) dt, \end{aligned} \quad (8) \quad (9)$$

where $\lambda_{ji} = \frac{1}{2}(\sigma_j + \sigma_i)$, the range of the interaction potential has been extended to infinity, and $Q_{ij}(r)$ are the factor correlation functions (FCF). Thus for n -component mixtures, there are two sets of n^2 equations each, Eqs. (8) and (9), in $3n^2$ functional unknowns: $\{c_{ij}(r)\}$, $\{h_{ij}(r)\}$, and $\{Q_{ij}(r)\}$. The additional set of n^2 equations needed to make the problem solvable is provided by Eq. (5) within the core, and by Eq. (6) outside it.

From Eqs. (8) and (9) subject to the conditions given by Eqs. (5) and (6), $Q_{ij}(r)$ must have the following form:

$$Q_{ij}(r) = Q_{ij}^0(r) + \sum_{v=1}^{\omega} \frac{1}{z_v} D_{vij} e^{-z_v(r-\sigma_{ij})}, \quad (10)$$

where

$$Q_{ij}^0(r) = \begin{cases} \frac{a_{ij}}{2} (r - \sigma_{ij})^2 + b_{ij} (r - \sigma_{ij}) + \sum_{v=1}^{\omega} \frac{C_{vij}}{z_v} [e^{-z_v(r-\sigma_{ij})} - 1], & (\lambda_{ji} \leq r < \sigma_{ij}) \\ 0, & (r \geq \sigma_{ij}) \end{cases} \quad (11)$$

The need for this mathematical form is especially clear at zero density. For this case, it is obvious that $Q_{ij}^0(r)$ in Eq. (10) must vanish outside the core leaving only the exponential term, since otherwise Eq. (8) could not agree with Eq. (6). On the other hand, to satisfy Eq. (5) inside the core, $Q'_{ij}(r)$ in Eq. (9) must be linear in r . In other words, $Q_{ij}(r)$ must be a second degree polynomial inside the core. This explains the form of $Q_{ij}^0(r)$ for $r < \sigma_{ij}$ in Eq. (11), where the C_{vij} exponential terms are needed to cancel out the analogous D_{vij} terms from Eq. (10). Finally, the use of the $(r - \sigma_{ij})$ and $[e^{-z_v(r-\sigma_{ij})} - 1]$ terms in Eq. (11) is dictated by the requirement that $Q_{ij}^0(r)$, as it vanishes at $r = \sigma_{ij}$, should not introduce a discontinuity in $Q_{ij}(r)$.

In principle, for n components in the mixture interacting through ω Yukawa tails, there are $n^2(2 + 2\omega)$ unknowns: the coefficients of the $Q_{ij}(r)$. In addition, the integrations involving the unknown functions $h_{ij}(r)$, or equivalently $g_{ij}(r)$, create $n^2\omega$ more unknowns, denoted by

$$\hat{g}_{vij} = \hat{g}_{ij}(z_v) = \int_0^{\infty} r e^{-z_v r} g_{ij}(r) dr. \quad (12)$$

As a result, $n^2(2 + 3\omega)$ quantities must be found to solve the problem

$$\{a_{ij}\}, \{b_{ij}\}, \{C_{vij}\}, \{D_{vij}\}, \{\hat{g}_{vij}\}.$$

Using Eq. (9) within the core, with the left-hand side given by Eq. (5), and the right-hand side given by Eqs. (10) and (11), one gets $2 + \omega$ kinds of terms: terms in r , constant terms, and ω different $e^{-z_v r}$ exponential terms. Equating both sides of Eq. (9) for each of these kinds, $2 + \omega$ sets of n^2 equations are obtained. They permit $\{a_{ij}\}$, $\{b_{ij}\}$, and $\{C_{vij}\}$ to be expressed as functions of $\{D_{vij}\}$ and $\{\hat{g}_{vij}\}$. Consequently, the problem is reduced to the determination of these last $2n^2\omega$ unknowns from $2n^2$ equations, Eqs. (8) and (9), both for $r \geq \sigma_{ij}$.

Again, in Eq. (8) for $r \geq \sigma_{ij}$, each $e^{-z_v r}$ factor requires a separate equality for its coefficients, which results in $n^2\omega$ relations between the unknowns. On the other hand, the direct use of Eq. (9) presents some mathematical inconvenience. It is better to take Eq. (9) for $r < \sigma_{ij}$, extend it analytically outside the core, and subtract it from the original version of Eq. (9). Then, the resulting relation is multiplied

by each of the ω exponentials $e^{-z_\nu(r-\sigma_{ij})}$, and integrated from σ_{ij} to ∞ ; thus the integral in Eq. (9) is separated (through the convolution theorem) into the product of two integrals, one of them yielding \hat{g}_{ij} . This gives the remaining $n^2\omega$ equations needed to solve the problem.

Blum and Høye³ (BH) explain fully the procedure summarized above. Following it, the entire problem can be described by a system of $2n^2\omega$ nonlinear equations in $2n^2\omega$ unknowns. Once BH's method is completely developed, the final system can be divided into two subsets of $n^2\omega$ equations (each of these equations corresponding to a given vij combination),

$$\sum_{\tau} \sum_{lmk} A_{\tau vmkjl}^{(1)} G_{\tau km} D_{\tau ml} D_{vil} + \sum_{\tau} \sum_{lm} A_{\tau vmjl}^{(2)} D_{\tau ml} D_{vil} + \sum_{\tau} A_{vijl}^{(3)} D_{vil} + A_{vij}^{(4)} = 0, \quad (13)$$

$$\sum_{\tau} \sum_{lmk} B_{\tau vmklj}^{(1)} G_{\tau km} D_{\tau mj} G_{vil} + \sum_{\tau} \sum_{mk} B_{\tau vmkij}^{(2)} G_{\tau km} D_{\tau mj} + \sum_{\tau} \sum_{lm} B_{\tau vmlij}^{(3)} D_{\tau mj} G_{vil} + \sum_{\tau} \sum_m B_{\tau vmij}^{(4)} D_{\tau mj} + \sum_{\tau} B_{vij}^{(5)} G_{vil} + B_{vij}^{(6)} = 0. \quad (14)$$

Roman subindices vary between 1 and n , denoting specific components in the mixture; Greek subindices (τ and ν) vary between 1 and ω , denoting specific Yukawa tails in the interaction potential. The $A^{(\gamma)}$ and $B^{(\gamma)}$ coefficients are calculated from the data (σ_i , ϵ_{vij} , z_ν , ρ_i , T) using the explicit expressions given in Appendix A. The only unknown quantities are the $\{D_{vij}\}$ parameters of the factor correlation functions and the $\{G_{vij}\}$ transforms of the radial distribution functions given by

$$G_{vij} = z_\nu \hat{g}_{vij} e^{z_\nu \sigma_{ij}} = z_\nu \int_{\sigma_{ij}}^{\infty} r e^{-z_\nu(r-\sigma_{ij})} g_{ij}(r) dr. \quad (15)$$

The change of variable introduced by Eq. (15), relative to Eq. (12), allows the elimination of most exponentials (and in particular, all having positive exponents) when calculating the coefficients of Eqs. (13) and (14).

III. SOLUTION METHOD

To calculate the properties of a Yukawa mixture in the MSA, the solution of a system of $2\omega n^2$ nonlinear equations, represented by Eqs. (13) and (14), in as many unknowns ($\{D_{vij}\}$, $\{G_{vij}\}$) is required. This is the only nonanalytical part of the problem.

From a computational point of view, it is better to express these equations as functions that must be driven to zero. A convenient way of doing this is as follows:

$$\Theta_{vij}^{(a)} = \sum_{\tau} (\rho_l \hat{Q}_{vijl} - \delta_{ij}) D_{vil} + A_{vij}^{(4)}, \quad (16)$$

$$\Theta_{vij}^{(b)} = \sum_{\tau} (\rho_l \hat{Q}_{vijl} - \delta_{ij}) G_{vil} + P_{vij}, \quad (17)$$

where

$$\hat{Q}_{vij} = \sum_{\tau} \sum_k [C_{\tau vkij}^{(a)} f_{\tau kj} + D_{\tau vkij}^{(a)} D_{\tau kj}] + \frac{1}{z_\nu^3} H_{vij}^{(a)}, \quad (18)$$

$$P_{vij} = \sum_{\tau} \sum_k [C_{\tau vkij}^{(b)} f_{\tau kj} + D_{\tau vkij}^{(b)} D_{\tau kj}] + \frac{1}{2\pi} H_{vij}^{(b)}, \quad (19)$$

and

$$f_{\tau kj} = \frac{2\pi}{z_\tau^2} \sum_m \rho_m G_{\tau km} D_{\tau mj}. \quad (20)$$

The quantity \hat{Q}_{vij} is basically a Laplace transform of the corresponding factor correlation function

$$\hat{Q}_{vij} = \int_{\lambda_{ij}}^{\infty} Q_{vij}(r) e^{-z_\nu(r-\lambda_{ij})} dr. \quad (21)$$

Again, the $C^{(\gamma)}$, $D^{(\gamma)}$, and $H^{(\gamma)}$ parameters can be determined explicitly from the data, see Appendix A. The symmetrical structure of the equations above makes them well suited to numerical calculation.

Equations (13) and (14) [or equivalently the $\Theta_{vij}^{(\gamma)}$ functions given by Eqs. (16) and (17) and equated to zero] are solved using the Newton–Raphson technique, with the partial derivatives evaluated analytically. This iterative technique provides a fast and reliable convergence to the final solution. As Pastore¹² suggested, there are other methods to solve Eqs. (13) and (14). In particular, given that Eq. (14) is linear in the $\{D_{\tau mj}\}$, one can use Eq. (14) to express those parameters in terms of the $\{G_{vil}\}$ and substitute them in Eq. (13). Altogether, since $\{G_{vij}\} = \{G_{vji}\}$ for all ν , one can reduce the system to $\omega n(n+1)/2$ equations. However, a simplification of the system is possible only through the use of a symbolic manipulation program and leads to a very considerable complication of the remaining equations. In the process, the symmetric structure of the equations—which facilitates their evaluation—is likely to be lost, and their convergence properties may be altered.

As a measure of the error for any set of values of the variables, the following norm of the deviations is used:

$$\Omega = \sqrt{\frac{1}{2\omega n^2} \sum_{\nu} \sum_{ij} \left(\left\{ \frac{\Theta_{vij}^{(a)}}{\max[1, A_{vij}^{(4)}]} \right\}^2 + \left\{ \frac{\Theta_{vij}^{(b)}}{\max[1, B_{vij}^{(6)}]} \right\}^2 \right)}.$$

A tolerance $\Omega \leq 10^{-6}$ is sufficiently small to determine uniquely the first six significant digits for all thermodynamic properties. The above norm of the error is tested at every Newton–Raphson iteration to avoid overshooting.

An essential part in any iterative method is the initial estimation of the solution. The estimate used in this work is based on the asymptotic behavior of Eqs. (13) and (14) at high temperature. It is worth noting that all energy-related

quantities, ϵ_{vij} and T , take part in the system only through the coefficients $A_{vij}^{(4)} = 2\pi\sigma_{ij}\epsilon_{vij}/kT$. A Taylor series expansion from the infinite temperature (hard-sphere) limit up to the first nonzero terms results in the following two linear systems:

$$\sum_l A_{vijl}^{(3)} D_{vil} = -A_{vij}^{(4)}, \quad (23)$$

$$\sum_l B_{vijl}^{(5)} G_{vil} = -B_{vij}^{(6)}. \quad (24)$$

Equation (24) yields the exact $\{G_{vij}\}$ solution for the hard-sphere RDFs. On the other hand, the solution of Eq. (23) corresponds to the first derivative term of the Taylor series, since at infinite temperature all $\{D_{vij}\}$ would be zero. Together, these two equations provide an excellent initial estimate. In most cases, only two or three iterations are needed to reach the final solution. This estimate can be easily improved by including more expansion terms, but in most cases such an improvement is not cost effective in regard to the total computer time required.

The correctness of the MSA solutions yielded by this multi-Yukawa algorithm was verified by reproducing results obtained previously by Konior and Jedrzejek for pure components with two- and three-Yukawa potentials^{9,13} and for equimolar symmetric binary mixtures (both components having equal like-particle interactions, the cross interaction being different) with a two-Yukawa potential.¹⁴ Also reproduced were the results for general one-Yukawa mixtures by Arrieta *et al.*⁶

This work provides numerical results for two specific binary multi-Yukawa mixtures, designated as M1 and M2, whose molecular characteristics are described in Table I. The interaction potentials of these mixtures are plotted in Figs. 1 and 2, respectively. Additive hard cores, $\sigma_{12} = \frac{1}{2}(\sigma_{11} + \sigma_{22})$, are assumed for both mixtures. Outside the hard cores, the multi-Yukawa interactions were fitted to Lennard-Jones potentials, by means of a direct, point by point, least squares procedure. All three different $\phi_{ij}(r)$ interactions were fitted simultaneously, using 100 points between $r = \sigma_{ij}$ and $r = \sigma_{ij} + 5\sigma_{11}$ for each of them. Al-

TABLE I. Molecular characteristics of the multi-Yukawa mixtures^a studied in this work.

| Mixture | σ_1 | σ_2^b | Y. tail ν | ϵ_{v11} | ϵ_{v12} | ϵ_{v22} | $z_v\sigma_1$ |
|-----------------|------------|--------------|---------------|------------------|------------------|------------------|---------------|
| M1 ^c | 1.000 | 1.167 | 1 | -2.8957 | -3.7691 | -4.8585 | 11.4287 |
| | | | 2 | 2.2992 | 2.4906 | 2.4856 | 4.3536 |
| | | | 3 | 0.6172 | 1.2865 | 2.3628 | 1.9991 |
| M2 ^d | 1.000 | 1.500 | 1 | -6.2557 | -3.6888 | -1.6581 | 10.2547 |
| | | | 2 | 4.8080 | 1.1427 | 3.3630 | 7.8556 |
| | | | 3 | 1.4126 | 2.3672 | 4.2247 | 2.5643 |
| | | | 4 | 0.0447 | 0.1795 | 0.8003 | 1.0894 |

^aBeyond the hard-core diameters σ_{ij} , the Yukawa interactions were fitted to Lennard-Jones (LJ) mixtures with same σ_{ij} diameters.

^b $\sigma_{ij} = \frac{1}{2}(\sigma_{ii} + \sigma_{jj})$.

^cYukawa ϵ_{vij} , z_v fitted to LJ mixture with $\epsilon_{11}^{\text{LJ}} = 1.000$, $\epsilon_{22}^{\text{LJ}} = 1.919$, $\epsilon_{12}^{\text{LJ}} = \sqrt{\epsilon_{11}^{\text{LJ}}\epsilon_{22}^{\text{LJ}}}$.

^dYukawa ϵ_{vij} , z_v fitted to LJ mixture with $\epsilon_{11}^{\text{LJ}} = 1.000$, $\epsilon_{22}^{\text{LJ}} = 2.000$, $\epsilon_{12}^{\text{LJ}} = 0.835\sqrt{\epsilon_{11}^{\text{LJ}}\epsilon_{22}^{\text{LJ}}}$.

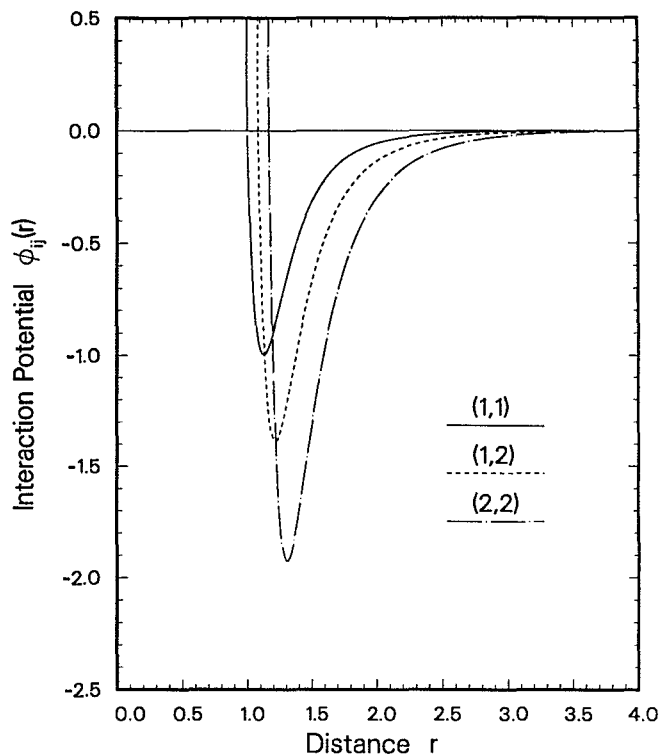


FIG. 1. Three-Yukawa interaction potential, $\phi_{ij}(r)$, for mixture M1. The parameters are given in Table I.

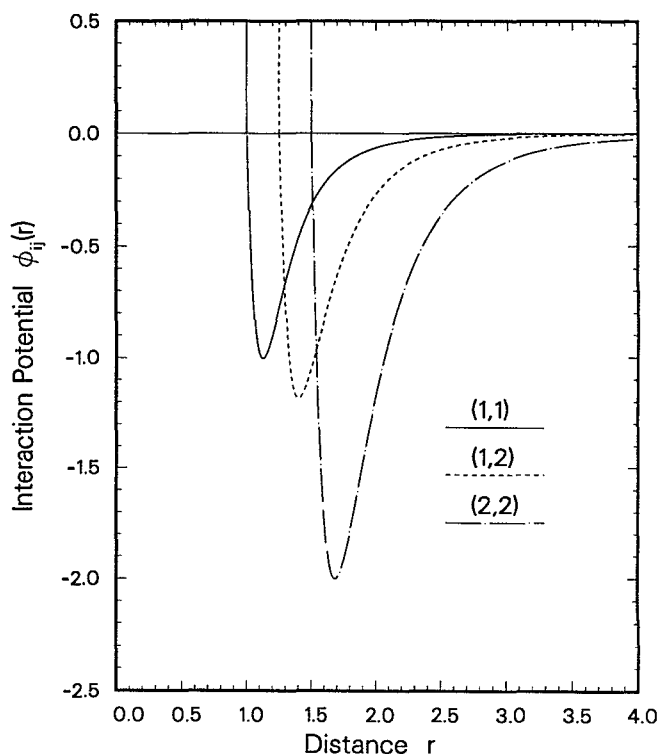


FIG. 2. Four-Yukawa interaction potential, $\phi_{ij}(r)$, for mixture M2. The parameters are given in Table I.

though all points were equally weighted, they were spaced evenly in \sqrt{r} to provide more fitting points at lower values of r . The difference between model and fitted potentials is hardly distinguishable at the scale of Figs. 1 and 2. However, the fit is not perfect, as can be seen by comparing the resulting MSA second virial coefficients. This is done in Appendix B.

Because the MSA is less accurate for soft positive interactions [$\phi(r) > 0$], they were avoided completely. However, the potentials include a significant repulsive (negative slope) interval. Mixture M1 has a three-Yukawa potential with parameters chosen to resemble an argon-xenon mixture: $\sigma_{22}/\sigma_{11} = 1.167$, $\epsilon_{22}^{LJ}/\epsilon_{11}^{LJ} = 1.919$, and $\epsilon_{12}^{LJ} = \sqrt{\epsilon_{11}^{LJ}\epsilon_{22}^{LJ}}$. On the other hand, mixture M2 has a four-Yukawa potential with a large size difference between the molecules of both components, $\sigma_{22}/\sigma_{11} = 1.500$, and a relatively weak cross interaction, $\epsilon_{12}^{LJ} = 0.835\sqrt{\epsilon_{11}^{LJ}\epsilon_{22}^{LJ}}$, chosen to induce nonideal behavior. The size difference in mixture M2 results in a ratio $(\sigma_{12}/\sigma_{11})^3 = 1.953 > 1.30$, where 1.30 corresponds to the limit beyond which the usually accepted mixing rules cannot be trusted, see Shing and Gubbins.¹⁵ (The size difference also required an additional Yukawa tail for mixture M2 to give a good fit to the model Lennard-Jones interaction.)

All specific results given in this work for thermodynamic conditions and properties have been scaled to dimensionless form using σ_{11} and ϵ_{11}^{LJ} . Therefore temperature values are given as kT/ϵ_{11}^{LJ} , pressure values as $P\sigma_{11}^3/\epsilon_{11}^{LJ}$, and density values are expressed in terms of the packing fraction $\eta = \frac{4}{3}\rho\sum_i x_i\sigma_i^3$.

For a specified set of thermodynamic conditions (composition x_i , density ρ , and temperature T), the Yukawa-MSA algorithm [starting from the initial estimate given by Eqs. (23) and (24), and using Newton-Raphson iterations] provides the solution to Eqs. (13) and (14). However, because of their nonlinearity, Eqs. (13) and (14) may not always have real solutions. Figures 3 and 4 delimit under the solid curves the temperature T , packing fraction η , region where no (real) mathematical solution is found for mixtures M1 and M2 at several compositions. (As in most other figures to follow, spline interpolation was used to connect MSA-determined points at narrow intervals of the independent variable; in this case, $\Delta\eta = 0.01$.) Figures 5 and 6 present several composition profiles taken from Figs. 3 and 4, respectively, at selected values of the packing fraction.

In Fig. 3, mixture M1 exhibits a smooth variation from one pure component to the other, with intermediate compositions behaving in the same qualitative way as the pure components do (as could be expected from an ideal mixture). For, say, pure component 1, at a fixed temperature $T = 0.5$, if a packing fraction $\eta = 0.20$ is specified, Eqs. (13) and (14) will not accept it (as neither would a real fluid under similar conditions); their solution would escape in opposite directions—so that an overall $\eta = 0.20$ can be met—to a low density (vapor) phase and a high density (liquid) phase. For M1 mixtures, such an escape would generally involve a secondary variation of composition as well as the main change in density.

Mixture M2 presents the same type of behavior at low densities. But, for intermediate compositions, at higher

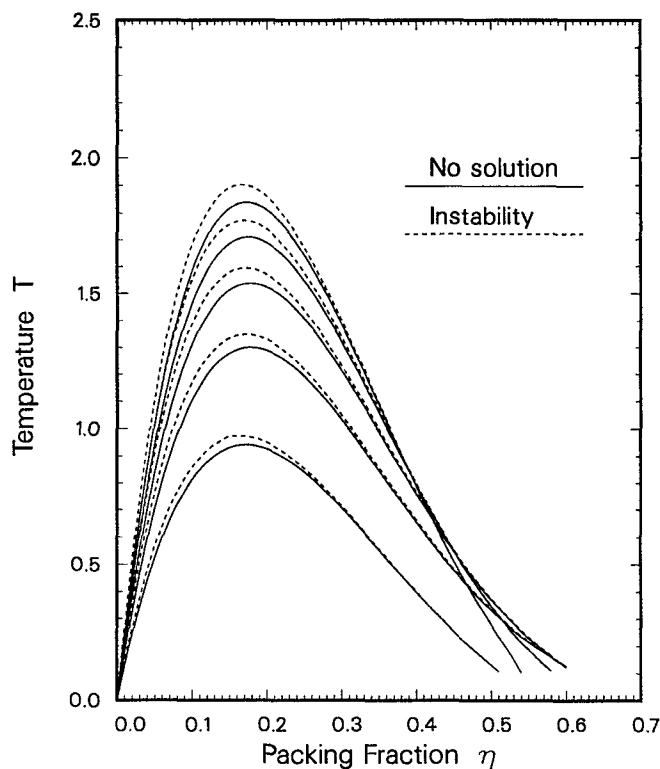


FIG. 3. No solution region (under solid line) and thermodynamic instability line (dashed line) for mixture M1. The five pairs of lines correspond, from top to bottom for $\eta = 0.20$, to the following compositions (given as mole fractions of component 1, x_1): 0.00, 0.25, 0.50, 0.75, 1.00.

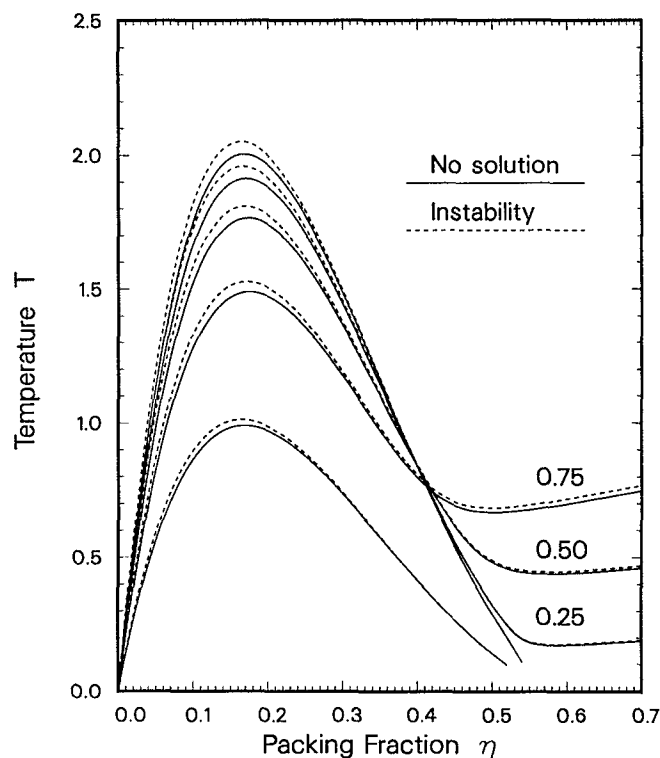


FIG. 4. No solution region (under solid line) and thermodynamic instability line (dashed line) for mixture M2. The five pairs of lines correspond, from top to bottom for $\eta = 0.20$, to the following compositions (given as mole fractions of component 1, x_1): 0.00, 0.25, 0.50, 0.75, 1.00.

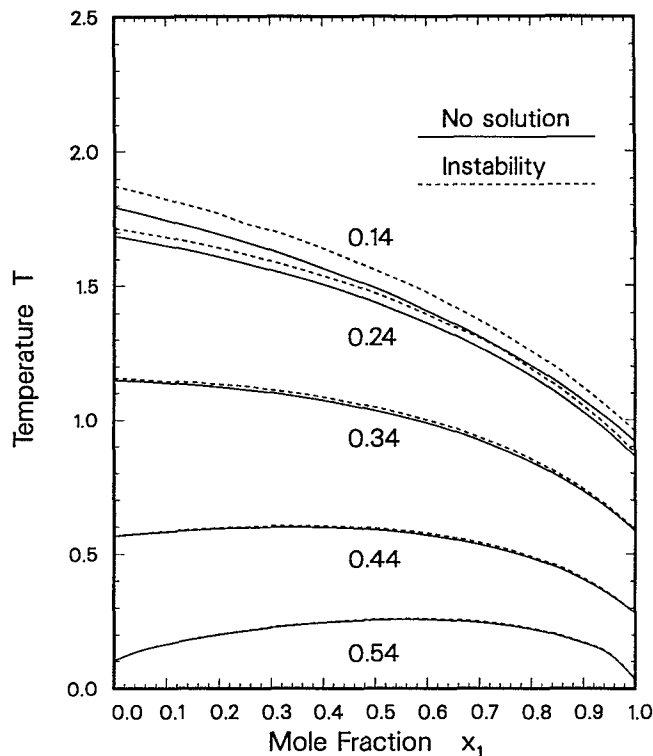


FIG. 5. No solution region (under solid line) and unstable band (between dashed and solid line) for mixture M1. The packing fraction corresponding to each pair of lines is indicated in the plot.

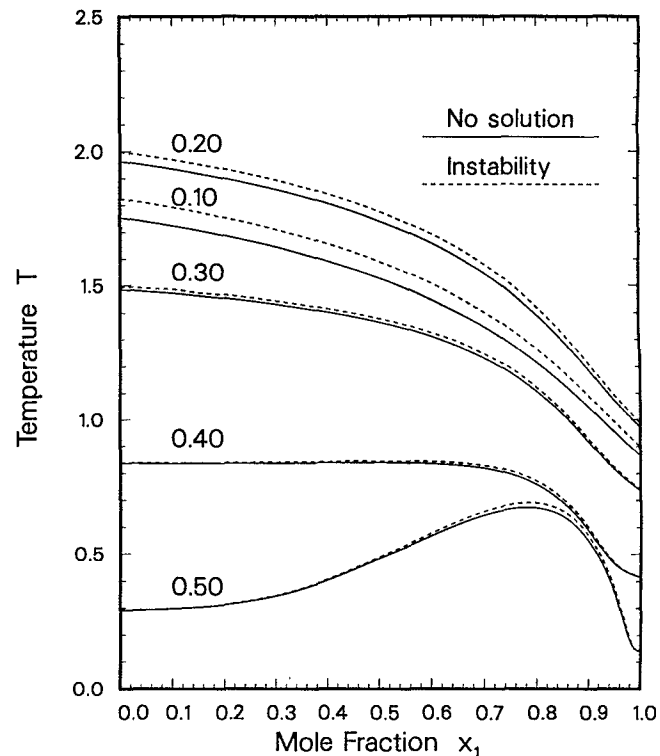


FIG. 6. No solution region (under solid line) and unstable band (between dashed and solid line) for mixture M2. The packing fraction corresponding to each pair of lines is indicated in the plot.

packing fractions a second forbidden region appears, one that offers no escape in the high density direction. In this case, for a fixed $T = 0.5$, if $x_1 = 0.75$ and $\eta = 0.50$ are specified, mixture M2 would escape in opposite directions to a $x_1 > 0.75$ phase and a $x_1 < 0.75$ phase, with a secondary change in density being also involved. It is the “hump” shown in Fig. 6 for $\eta = 0.50$ that makes possible the coexistence of two high density (liquid) phases of different composition. This hump arises mainly because the unlike-particle attractions (ϵ_{12}^{IJ}) in M2 are relatively weaker than the like-particle interactions (ϵ_{11}^{IJ} , ϵ_{22}^{IJ}).

Around the nonsolution region a thin band, limited by the dashed lines, appears in Figs. 3 to 6. The mathematical solutions inside this band are nonphysical, as they lack thermodynamic stability. Above the dashed lines the existence of a unique physical solution can be assured. The detailed examination of these regions of instability is deferred to Sec. V.

Table II presents the solution values G_{vij} , with $G_{v12} = G_{v21}$, and D_{vij} for Eqs. (13) and (14) for mixtures M1 and M2 for few selected values of compositions, packing fractions, and temperatures.

IV. CALCULATION OF THERMODYNAMIC PROPERTIES

This section follows Blum and Høye’s work, developing their expressions to their final, ready-to-use form. Once the variables $\{D_{vij}\}$, $\{G_{vij}\}$ have been found, the remaining factor correlation function parameters, i.e., $\{a_{ij}\}$, $\{b_{ij}\}$ and $\{C_{vij}\}$, are then determined,

$$C_{vij} = f_{vij} e^{-z_r \sigma_{ij}} - D_{vij}, \quad (25)$$

where f_{vij} is given by Eq. (20), and

$$A_j = A_j^0 (1 + M_j) - \frac{4}{\sigma_j^2} B_j^0 N_j, \quad (26)$$

$$a_{ij} = A_j, \quad (27)$$

$$b_{ij} = b_{ij}^0 (1 + M_j) + A_i^0 N_j, \quad (28)$$

where the M_j and N_j quantities, originally utilized by Blum and Høye, are

$$M_j = - \sum_{\tau} \frac{1}{z_{\tau}^2} \sum_m \rho_m \{ M_{\tau m}^{(a)} D_{\tau m j} + [1 - M_{\tau m}^{(a)} e^{-z_r \sigma_m}] f_{\tau m j} \}, \quad (29)$$

$$N_j = \sum_{\tau} \frac{1}{z_{\tau}^3} \sum_m \rho_m \{ L_{\tau m j}^{(a)} D_{\tau m j} + [1 + z_r \lambda_{jm} - L_{\tau m j}^{(a)} e^{-z_r \sigma_m}] f_{\tau m j} \}. \quad (30)$$

In these equations, all coefficients whose superscript is between parentheses or equal to zero are defined in Appendix A.

From Eq. (9), the radial distribution function contact values, $g_{ij}(\sigma_{ij})$, are produced by the discontinuity of $Q'_{ij}(r)$ at contact. Therefore

$$g_{ij}(\sigma_{ij}) = \frac{1}{2\pi\sigma_{ij}} \left(b_{ij} - \sum_{\tau} C_{\tau ij} \right), \quad (31)$$

TABLE II. Solutions for the system of nonlinear equations.

| Mixture | x_i | η | kT/ϵ_{11}^L | ν | G_{v11} | G_{v12} | G_{v22} | D_{v11} | D_{v12} | D_{v21} | D_{v22} |
|---------|-------|--------|----------------------|-------|-----------|-----------|-----------|-----------|-----------|-----------|-----------|
| M1 | 0.25 | 0.34 | 1.40 | 1 | 2.1779 | 2.3669 | 2.5682 | -10.1766 | -15.3965 | -14.4028 | -21.3630 |
| | | | | 2 | 2.0022 | 2.1807 | 2.4060 | 6.6170 | 8.0993 | 8.0526 | 8.6101 |
| | | | | 3 | 1.9349 | 2.0665 | 2.2531 | 0.5525 | 3.8362 | 1.7864 | 7.4788 |
| | 0.50 | 0.34 | 1.40 | 1 | 2.1933 | 2.3876 | 2.5928 | -10.2078 | -15.3869 | -14.4328 | -21.3348 |
| | | | | 2 | 2.0011 | 2.1849 | 2.4142 | 6.5020 | 7.8977 | 7.8359 | 8.2846 |
| | | | | 3 | 1.9290 | 2.0675 | 2.2594 | 0.7825 | 4.0566 | 2.1457 | 7.7948 |
| | 0.50 | 0.34 | 1.70 | 1 | 2.2110 | 2.4113 | 2.6160 | -8.3503 | -12.5235 | -11.8076 | -17.3638 |
| | | | | 2 | 2.0037 | 2.1860 | 2.3997 | 5.2754 | 6.2928 | 6.3671 | 6.5930 |
| | | | | 3 | 1.9297 | 2.0678 | 2.2426 | 0.5807 | 3.1578 | 1.6412 | 6.0571 |
| | 0.75 | 0.44 | 1.70 | 1 | 2.8913 | 3.1734 | 3.4446 | -7.2005 | -11.0384 | -10.1815 | -15.2663 |
| | | | | 2 | 2.2892 | 2.4994 | 2.7200 | 3.9058 | 4.4098 | 4.7210 | 4.3512 |
| | | | | 3 | 2.0332 | 2.1802 | 2.3432 | 0.3439 | 2.6815 | 1.0189 | 4.9088 |
| M2 | 0.25 | 0.30 | 2.10 | 1 | 2.0672 | 2.5176 | 3.0477 | -17.2947 | -11.7338 | -12.9650 | -6.2216 |
| | | | | 2 | 2.0620 | 2.5084 | 3.0631 | 13.6563 | 3.1490 | 5.6708 | -13.1626 |
| | | | | 3 | 1.9787 | 2.3404 | 2.8505 | 2.4629 | 5.8886 | 5.0838 | 12.6287 |
| | | | | 4 | 2.2244 | 2.5119 | 2.9139 | -0.0112 | 0.4040 | -0.1032 | 2.1677 |
| | 0.50 | 0.30 | 1.70 | 1 | 2.0752 | 2.5034 | 3.0448 | -21.0266 | -13.9810 | -15.7183 | -7.2123 |
| | | | | 2 | 2.0687 | 2.4954 | 3.0717 | 16.4091 | 3.1060 | 6.5053 | -17.2158 |
| | | | | 3 | 1.9710 | 2.3186 | 2.8718 | 3.1194 | 7.5209 | 6.4587 | 16.1611 |
| | | | | 4 | 2.2178 | 2.4931 | 2.9361 | 0.0089 | 0.5796 | -0.0023 | 3.1202 |
| | 0.50 | 0.40 | 1.70 | 1 | 2.5797 | 3.2102 | 3.9525 | -19.7280 | -11.6647 | -14.9046 | -5.7608 |
| | | | | 2 | 2.5103 | 3.1112 | 3.8485 | 15.6271 | 1.6764 | 7.2946 | -15.7789 |
| | | | | 3 | 2.1401 | 2.5506 | 3.1121 | 2.1366 | 5.2655 | 4.3623 | 11.3513 |
| | | | | 4 | 2.2797 | 2.5817 | 2.9921 | -0.0586 | 0.3767 | -0.3622 | 2.0393 |
| | 0.75 | 0.40 | 1.70 | 1 | 2.5699 | 3.2224 | 4.0462 | -18.6157 | -9.7903 | -13.9699 | -4.1954 |
| | | | | 2 | 2.4841 | 3.1002 | 3.9079 | 14.2714 | -0.6312 | 6.0494 | -17.8425 |
| | | | | 3 | 2.0855 | 2.4964 | 3.0984 | 2.1189 | 5.1529 | 4.3608 | 11.1867 |
| | | | | 4 | 2.2448 | 2.5484 | 2.9906 | -0.0263 | 0.4539 | -0.1800 | 2.4778 |

while the MSA, or PY, hard-sphere contact values are

$$g_{ij}^0(\sigma_{ij}) = \frac{b_{ij}^0}{2\pi\sigma_{ij}}. \quad (32)$$

Table III presents the MSA contact values for both mixtures, M1 and M2, under a variety of conditions.

From the correlation parameters, three thermodynamic properties can be calculated directly: configurational energy, isothermal compressibility, and pressure. The configurational energy U^c per molecule is equal to

$$\frac{U^c}{N} = -2\pi\rho \sum_{ij} x_i x_j \sigma_{ij} \left(\sum_{\tau} \frac{1}{z_{\tau}} \epsilon_{\tau ij} G_{\tau ij} \right), \quad (33)$$

N being the total number of molecules in the system, and $\{x_i\}$ representing the mole fractions. The inverse isothermal compressibility calculated through the fluctuation theorem is given by

$$\chi^{-1} = \frac{1}{kT} \left(\frac{\partial P}{\partial \rho} \right)_T = 1 - \rho \sum_{ij} x_i x_j \tilde{c}_{ij}(0) = \sum_j x_j \left(\frac{A_j}{2\pi} \right)^2, \quad (34)$$

where the $\tilde{c}_{ij}(0)$ are defined by Eq. (42) below. The corresponding hard-sphere quantity is

$$\chi_0^{-1} = \sum_j x_j \left(\frac{A_j^0}{2\pi} \right)^2. \quad (35)$$

Finally, the virial pressure, P^v is obtained through

$$\frac{P^v}{\rho kT} = 1 + \frac{2\pi}{3} \rho \sum_{ij} x_i x_j \sigma_{ij}^3 g_{ij}(\sigma_{ij}) + J, \quad (36)$$

where

$$J = \frac{2\pi}{3} \rho \sum_{ij} x_i x_j \sum_{\tau} K_{\tau ij} \left(G'_{\tau ij} - \frac{1}{z_{\tau}} G_{\tau ij} \right), \quad (37)$$

TABLE III. MSA radial distribution function contact values.

| Mixture | x_i | η | kT/ϵ_{11}^L | $g_{11}(\sigma_{11})$ | $g_{12}(\sigma_{12})$ | $g_{22}(\sigma_{13})$ |
|---------|-------|--------|----------------------|-----------------------|-----------------------|-----------------------|
| M1 | 0.25 | 0.34 | 1.40 | 1.9143 | 1.7562 | 1.5307 |
| | | 0.34 | 1.70 | 2.0241 | 1.9046 | 1.7239 |
| | | 0.44 | 1.40 | 3.0600 | 2.9562 | 2.7583 |
| | | 0.44 | 1.70 | 3.1618 | 3.1012 | 2.9661 |
| | 0.50 | 0.34 | 1.40 | 1.9531 | 1.7990 | 1.5757 |
| | | 0.34 | 1.70 | 2.0620 | 1.9461 | 1.7691 |
| | | 0.44 | 1.40 | 3.1202 | 3.0196 | 2.8261 |
| | | 0.44 | 1.70 | 3.2227 | 3.1655 | 3.0350 |
| | 0.75 | 0.34 | 1.40 | 2.0008 | 1.8501 | 1.6275 |
| | | 0.34 | 1.70 | 2.1091 | 1.9970 | 1.8233 |
| | | 0.44 | 1.40 | 3.1958 | 3.0991 | 2.9107 |
| | | 0.44 | 1.70 | 3.2992 | 3.2462 | 3.1211 |
| M2 | 0.25 | 0.30 | 1.70 | 1.7210 | 1.6403 | 1.4063 |
| | | 0.30 | 2.10 | 1.7843 | 1.7400 | 1.5707 |
| | | 0.40 | 1.70 | 2.4649 | 2.4884 | 2.3485 |
| | | 0.40 | 2.10 | 2.5330 | 2.5962 | 2.5475 |
| | 0.50 | 0.30 | 1.70 | 1.7334 | 1.6613 | 1.4481 |
| | | 0.30 | 2.10 | 1.8021 | 1.7671 | 1.6196 |
| | | 0.40 | 1.70 | 2.5071 | 2.5464 | 2.4475 |
| | | 0.40 | 2.10 | 2.5817 | 2.6610 | 2.6496 |
| | 0.75 | 0.30 | 1.70 | 1.7599 | 1.7060 | 1.5305 |
| | | 0.30 | 2.10 | 1.8376 | 1.8210 | 1.7129 |
| | | 0.40 | 1.70 | 2.5899 | 2.6626 | 2.6410 |
| | | 0.40 | 2.10 | 2.6743 | 2.7861 | 2.8445 |

and the symbol $G'_{\tau ij}$ represents

$$G'_{\tau ij} = z_{\tau} \left[\frac{\partial g_{ij}(s)}{\partial s} \right]_{s=z_{\tau}} e^{z_{\tau} \sigma_{ij}} \\ = -z_{\tau} \int_{\sigma_{ij}}^{\infty} r^2 e^{-z_{\tau}(r-\sigma_{ij})} g_{ij}(r) dr. \quad (38)$$

The computation of these derivatives is presented in Appendix C.

Each of these three thermodynamic properties (along with the temperature, density and composition) provides a route for the calculation of all other properties. Since MSA is an approximate method it does not provide thermodynamic inconsistency giving different results with the use of different routes. Within the MSA, it has been established⁷ that the properties calculated from the energy equation are more accurate than those obtained from the (virial) pressure or the isothermal compressibility equations. In addition, the *incremental* values (i.e., the difference with respect to the hard-sphere results) of these MSA energy-derived properties are given by closed form expressions.

The incremental energy pressure P^E (which should be preferred over P^V) is found from

$$\frac{\Delta P^E}{\rho kT} = \frac{\pi}{3} \rho \sum_{ij} x_i x_j \sigma_{ij}^3 \{ [g_{ij}(\sigma_{ij})]^2 - [g_{ij}^0(\sigma_{ij})]^2 \} + J, \quad (39)$$

where the RDF contact values are given by Eqs. (31) and (32), and J results from Eq. (37). The incremental Helmholtz free energy is yielded by

$$\frac{\Delta A}{NkT} = \frac{U^c}{NkT} - \frac{\Delta P^E}{\rho kT} + \frac{1}{2} (\chi^{-1} - \chi_0^{-1}). \quad (40)$$

Last, the incremental chemical potentials $\Delta\mu_i$, calculated from the energy equation, can be obtained from

$$\frac{\Delta\mu_i}{kT} = -2\pi \sum_j \rho_j \sum_{\tau} \frac{1}{z_{\tau}} K_{\tau ij} G_{\tau ij} \\ - \frac{1}{2} \sum_j \rho_j [\tilde{c}_{ij}(0) - \tilde{c}_{ij}^0(0)], \quad (41)$$

while $\tilde{c}_{ij}^0(0)$ correspond to the hard-sphere case. These quantities are calculated through their relation to the factor correlation functions,

$$\tilde{c}_{ij}(0) = 4\pi \int_0^{\infty} r^2 c_{ij}(r) dr, \quad (42)$$

while $\tilde{c}_{ij}^0(0)$ correspond to the hard-sphere case. These quantities are calculated through their relation to the factor correlation functions,

$$\tilde{c}_{ij}(0) = \bar{Q}_{ij} + \bar{Q}_{ji} - \sum_l \rho_l \bar{Q}_{il} \bar{Q}_{jl}, \quad (43)$$

[and similarly for $\tilde{c}_{ij}^0(0)$] where

$$\bar{Q}_{ij} = \int_{\lambda_{ij}}^{\infty} Q_{ij}(r) dr, \quad (44)$$

and therefore

$$\bar{Q}_{ij} = \frac{1}{2} a_{ij} \sigma_i^3 - \frac{1}{2} b_{ij} \sigma_i^2 - \sum_{\tau} \frac{1}{z_{\tau}^2} (C_{\tau ij} M_{\tau i}^{(a)} + f_{\tau ij}), \quad (45)$$

$$\bar{Q}_{ij}^0 = \frac{1}{2} a_{ij}^0 \sigma_i^3 - \frac{1}{2} b_{ij}^0 \sigma_i^2. \quad (46)$$

The equations above have been written so that numerical difficulties are avoided should any ρ_i approach zero.

Table IV gives results for the MSA energy-derived configurational energy, pressure and chemical potentials for a variety of compositions, packing fractions, and tempera-

TABLE IV. MSA energy-derived thermodynamic properties.

| Mixture | x_i | η | $kT/\epsilon_{11}^{\dagger}$ | $-U^c/N\epsilon_{11}^{\dagger}$ | $P/\rho kT$ | μ_1^c/kT | μ_2^c/kT |
|---------|-------|--------|------------------------------|---------------------------------|-------------|--------------|--------------|
| M1 | 0.25 | 0.34 | 1.40 | 7.730 | -0.876 | -2.179 | -5.900 |
| | | 0.34 | 1.70 | 7.664 | 0.113 | -0.932 | -3.704 |
| | | 0.44 | 1.40 | 10.003 | 1.946 | 0.209 | -3.238 |
| | | 0.44 | 1.70 | 9.958 | 3.141 | 1.769 | -0.487 |
| | 0.50 | 0.34 | 1.40 | 6.634 | -0.107 | -1.695 | -5.216 |
| | | 0.34 | 1.70 | 6.585 | 0.754 | -0.472 | -3.050 |
| | | 0.44 | 1.40 | 8.598 | 2.875 | 1.059 | -2.014 |
| | | 0.44 | 1.70 | 8.563 | 3.902 | 2.579 | 0.682 |
| | 0.75 | 0.34 | 1.40 | 5.530 | 0.691 | -1.079 | -4.338 |
| | | 0.34 | 1.70 | 5.498 | 1.421 | 0.114 | -2.215 |
| | | 0.44 | 1.40 | 7.182 | 3.857 | 2.149 | -0.442 |
| | | 0.44 | 1.70 | 7.158 | 4.714 | 3.621 | 2.185 |
| M2 | 0.25 | 0.30 | 1.70 | 6.908 | -0.406 | -0.692 | -4.486 |
| | | 0.30 | 2.10 | 6.826 | 0.374 | -0.061 | -2.631 |
| | | 0.40 | 1.70 | 9.268 | 1.115 | 0.197 | -3.103 |
| | | 0.40 | 2.10 | 9.224 | 2.168 | 1.058 | -0.604 |
| | 0.50 | 0.30 | 1.70 | 5.691 | 0.212 | -0.613 | -3.954 |
| | | 0.30 | 2.10 | 5.636 | 0.871 | 0.065 | -2.045 |
| | | 0.40 | 1.70 | 7.673 | 1.854 | 0.479 | -1.882 |
| | | 0.40 | 2.10 | 7.639 | 2.734 | 1.399 | 0.673 |
| | 0.75 | 0.30 | 1.70 | 4.624 | 0.819 | -0.448 | -2.976 |
| | | 0.30 | 2.10 | 4.591 | 1.370 | 0.310 | -0.978 |
| | | 0.40 | 1.70 | 6.273 | 2.641 | 1.046 | 0.401 |
| | | 0.40 | 2.10 | 6.250 | 3.369 | 2.066 | 3.058 |

tures. The hard-sphere contributions to those properties were calculated through the Carnahan–Mansoori–Starling–Leland (CMSL)¹⁶ equation of state.

Qualitatively, an increase in temperature increases the kinetic energy of the molecules, enabling them to move into configurations of higher potential energy (note the sign). At higher density the molecules are packed more closely, at distances of lower potential (or configurational) energy. Because the second component in both mixtures has a larger (in absolute value) global potential energy, an increase in x_2 results in higher absolute configurational energy.

The variation of pressure is also consistent with the behavior of real fluids. Increases in either density or temperature lead (in the liquid region) to higher compressibility factors. Under some conditions, the intermolecular attractions bringing the molecules together prevail over their kinetic energy. As a result, an external force, a negative pressure, is necessary to take the molecules apart from one another, so that they will occupy the full volume specified by the density. This explains the appearance of negative pressures.

Table IV shows the density residual values of the chemical potentials, i.e.,

$$\mu^r(\rho, T, x_i) = \mu(\rho, T, x_i) - \mu^*(\rho, T, x_i), \quad (47)$$

with $\mu^*(\rho, T, x_i)$ corresponding to the equivalent perfect gas mixture. Within a homogeneous phase, the chemical potentials usually increase with higher density (at constant temperature and composition). On the other hand, an increase in temperature gives rise to higher values of μ_i^r/kT . In all cases, an increase in the mole fraction of the smaller component (which, at constant packing fraction, augments the density) leads to higher chemical potentials.

Figures 7 to 16 analyze the behavior of the radial distribution functions. These RDFs have been obtained through an algorithm (given in Appendix D) based on Perram's procedure¹⁰ for hard spheres.

Figures 7 and 8 present the three different $g_{ij}(r)$ for binary mixtures M1 and M2, respectively, for the conditions specified in the figure captions. Figure 7 shows the effect of the short-range repulsion in the interaction potential, forcing the RDFs to bend downward as they approach contact. The same effect also appears in Fig. 8, although here it is partly opposed by an increased packing fraction η . This higher η , together with the larger size difference in M2, contributes to the more complex structure of the second peak.

Figures 9 to 16 focus on the response of the cross radial distribution function $g_{12}(r)$ to changing conditions. The other two RDFs behave in a qualitatively similar way, and have been omitted to avoid cluttering. In Fig. 9, η and T have been fixed to study the change of $g_{12}(r)$ with composition for M2. Such change is minimal up to the first depression, but then becomes significant in the medium and long range. Particularly, the character of the second peak is completely altered.

Figures 10 to 14 examine the variation of $g_{12}(r)$ with temperature for equimolar mixtures at low, moderate, and high values of the packing fraction. Figure 10 corresponds to mixture M1 at $\eta = 0.20$. As could be expected, at lower tem-

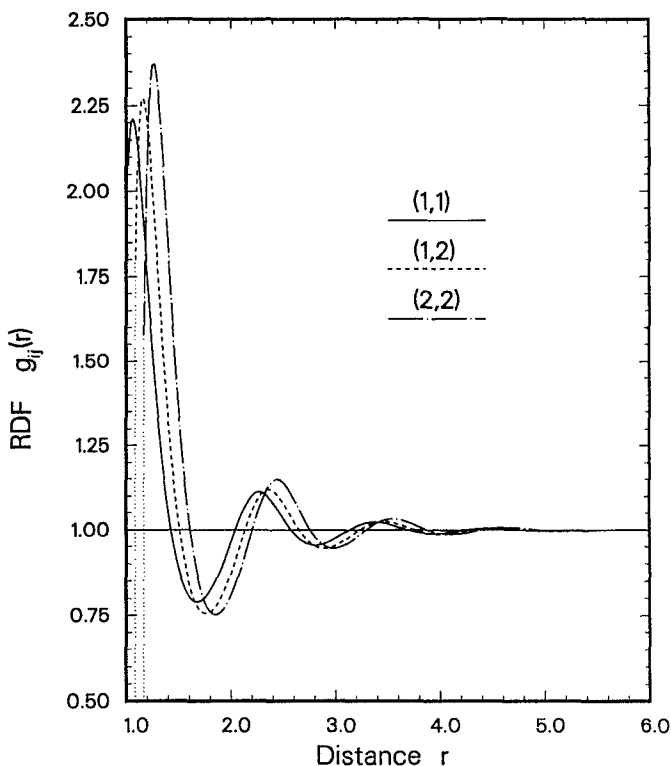


FIG. 7. Radial distribution functions $g_{ij}(r)$ for mixture M1 at $x_1 = 0.50$, $\eta = 0.34$, $T = 1.40$.

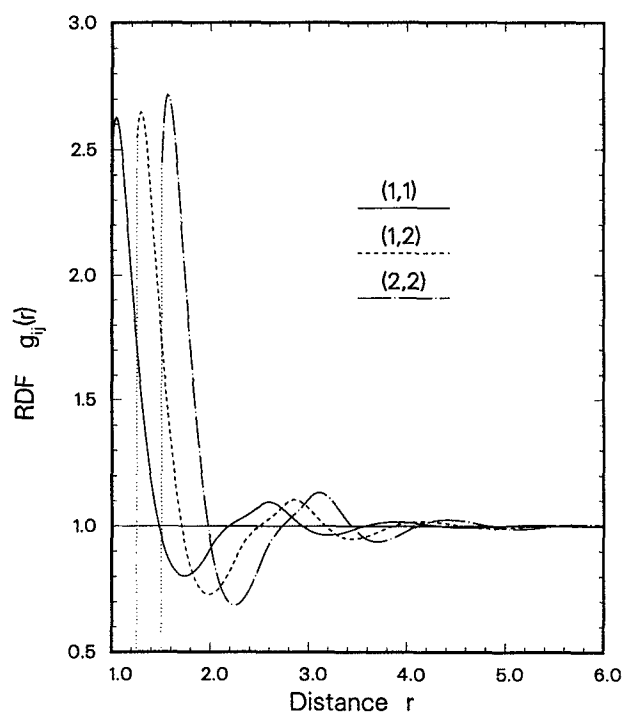


FIG. 8. Radial distribution functions $g_{ij}(r)$ for mixture M2 at $x_1 = 0.50$, $\eta = 0.40$, $T = 1.70$.

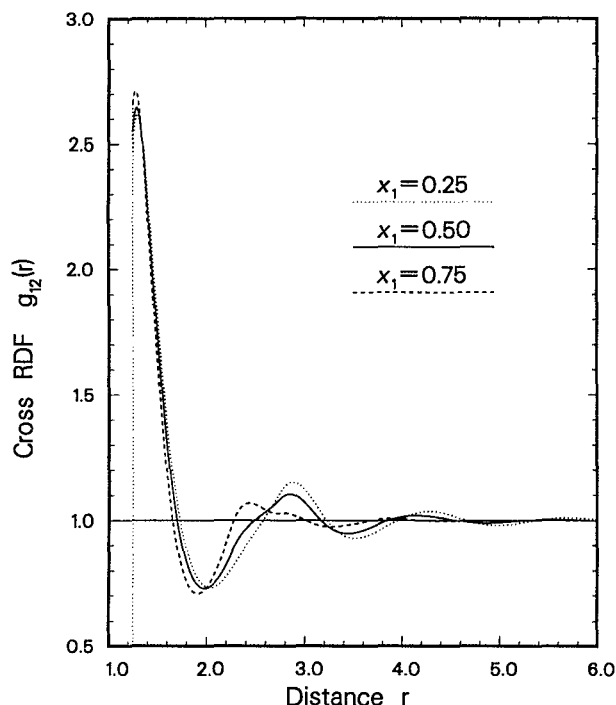


FIG. 9. Cross radial distribution function $g_{12}(r)$ for mixture M2 at $\eta = 0.40$, $T = 1.70$, and the three compositions indicated.

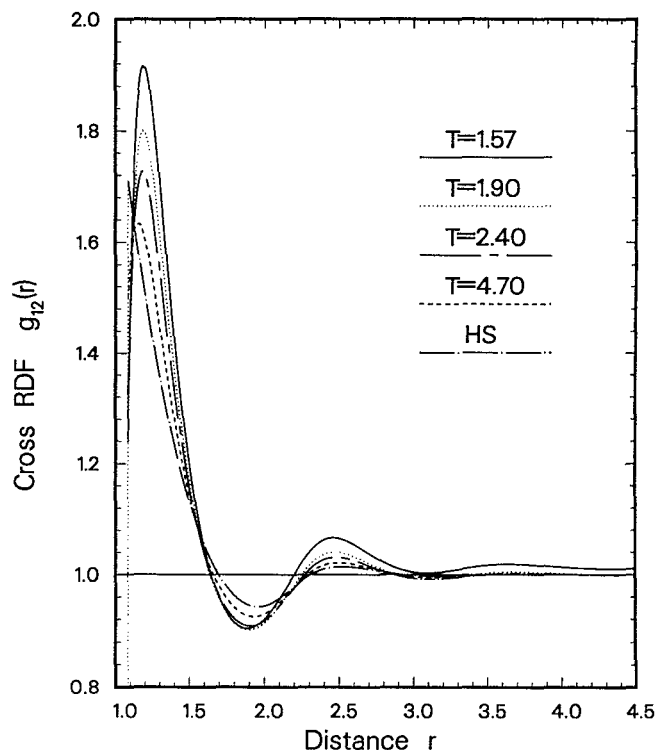


FIG. 10. Cross radial distribution function $g_{12}(r)$ for mixture M1 at $x_1 = 0.50$, $\eta = 0.20$, and the temperatures indicated. HS denotes the hard-sphere or infinite temperature limit. $T = 1.57$ falls on the spinodal line and produces an unstable, nonconvergent RDF.

peratures the molecules are more influenced by the interaction potential, resulting in lower contact values and higher rounded peaks. These rising peaks are produced by the concentration of molecules in the lowest energy region of the potential. Another result of the decrease in T is the increase in the range of the correlations. In the extreme, for $T = 1.57$ the RDFs do not converge. That temperature falls on the instability line drawn in Fig. 3. The question of thermodynamic stability is treated in depth in the next section.

Figure 11 depicts $g_{12}(r)$ for M2 at $\eta = 0.40$ and several temperatures. The same changes obvious in Fig. 10 appear here. At this higher density, the structure of the RDFs is dominated by the hard cores. A decrease in T produces an increase in the amplitude of the fluctuations (over those for the hard-sphere RDFs) that is roughly proportional to $1/T$. Again, the lowest temperature produces unstable, infinitely-ranged RDFs. A short-range detail of these RDFs is given in Fig. 12.

Figures 13 and 14 show $g_{12}(r)$ for M1 at a very high packing fraction $\eta = 0.64$, and some extremely low temperatures. In this case—especially in the amplified, long-range view given by Fig. 14—the periodicity of the RDFs is almost completely determined by the hard cores. Despite the very low temperatures, all these RDFs are convergent.

Figure 15 presents the response of $g_{12}(r)$ to increasing density for M1 at a constant temperature of $T = 1.00$. As η increases, the molecules are pushed closer together, overcoming the limited short-range repulsion. Other changes

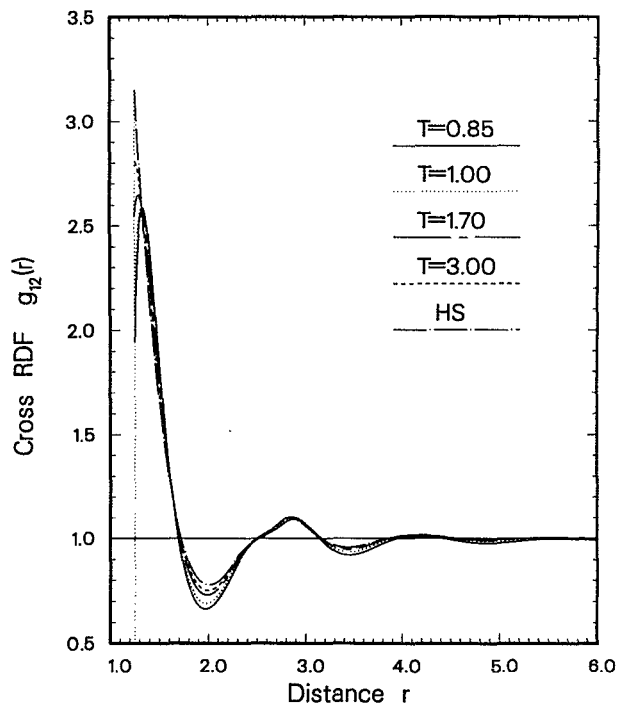


FIG. 11. Cross radial distribution function $g_{12}(r)$ for mixture M2 at $x_1 = 0.50$, $\eta = 0.40$, and the temperatures indicated. HS denotes the hard-sphere or infinite temperature limit. $T = 0.85$ falls on the spinodal line and produces an unstable, nonconvergent RDF.

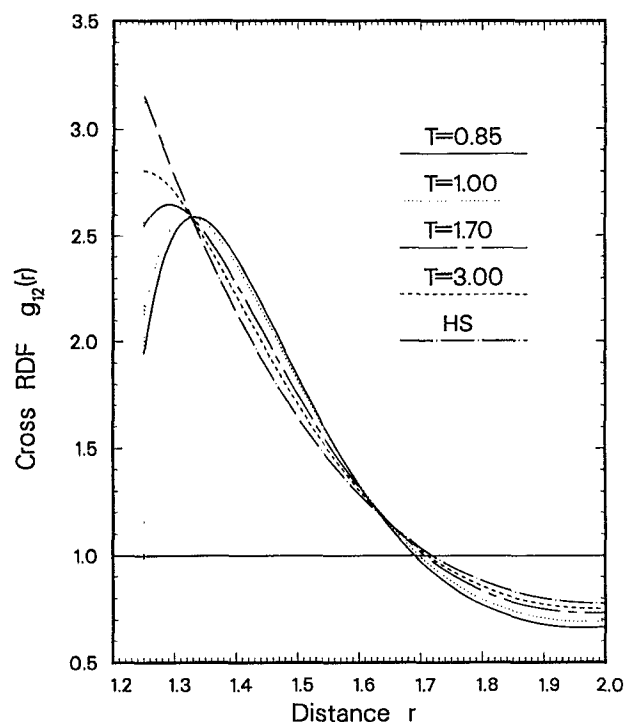


FIG. 12. Short-range detail of the RDF shown in Fig. 11.

produced by increasing values of η are shorter periods, wider fluctuations, and a more complex structure for the second peak. The conditions for $\eta = 0.35$ fall on the instability line. Only the highly amplified, long-range view in Fig. 16 reveals

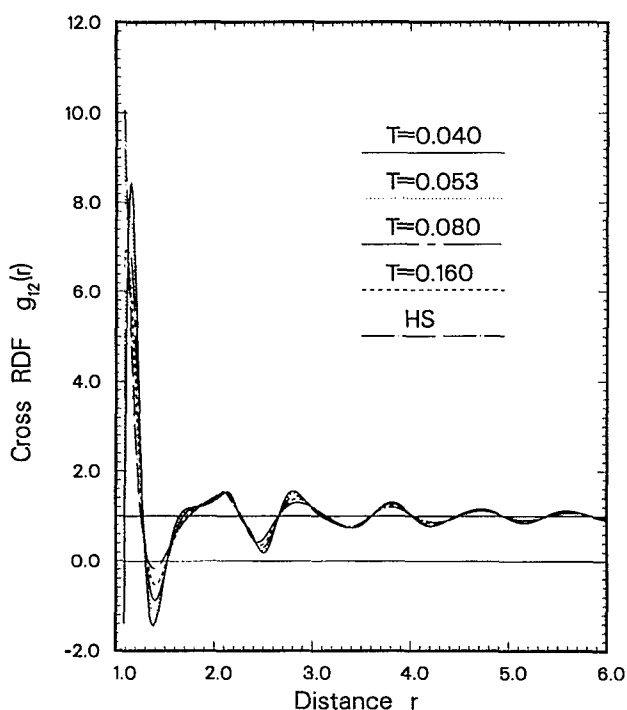


FIG. 13. Cross radial distribution function $g_{12}(r)$ for mixture M1 at $x_1 = 0.50$, $\eta = 0.64$, and the temperatures indicated. HS denotes the hard-sphere or infinite temperature limit.

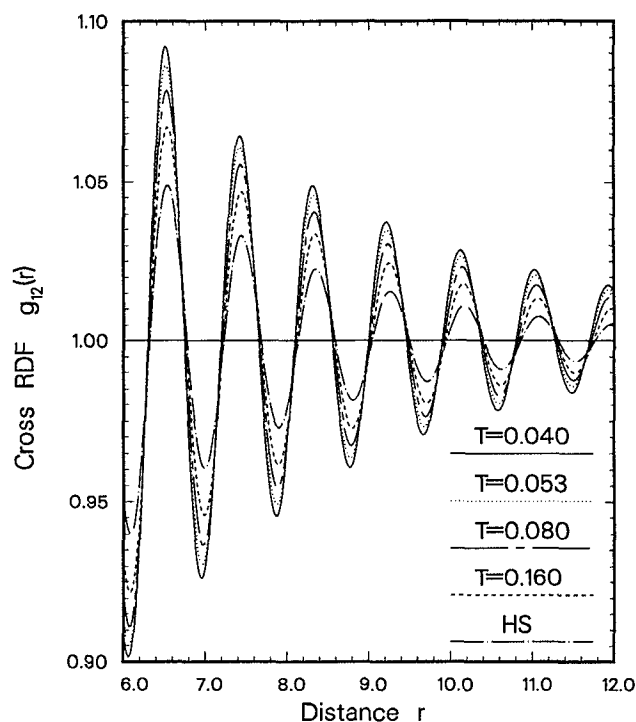


FIG. 14. Long-range detail of the RDF shown in Fig. 13.

the unstable character of the corresponding RDF. Figures 15 and 16 make obvious the need for a nonvisual criterion to distinguish between stable and unstable solutions. Such a criterion is given in Sec. VI.

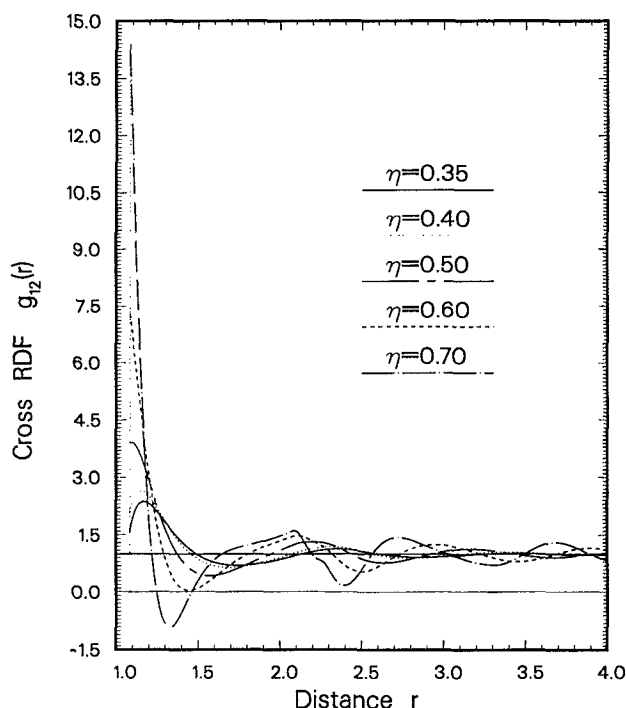


FIG. 15. Cross radial distribution function $g_{12}(r)$ for mixture M1 at $x_1 = 0.50$, $T = 1.00$, and the packing fractions indicated. $\eta = 0.35$ falls on the spinodal line and produces an unstable, nonconvergent RDF.

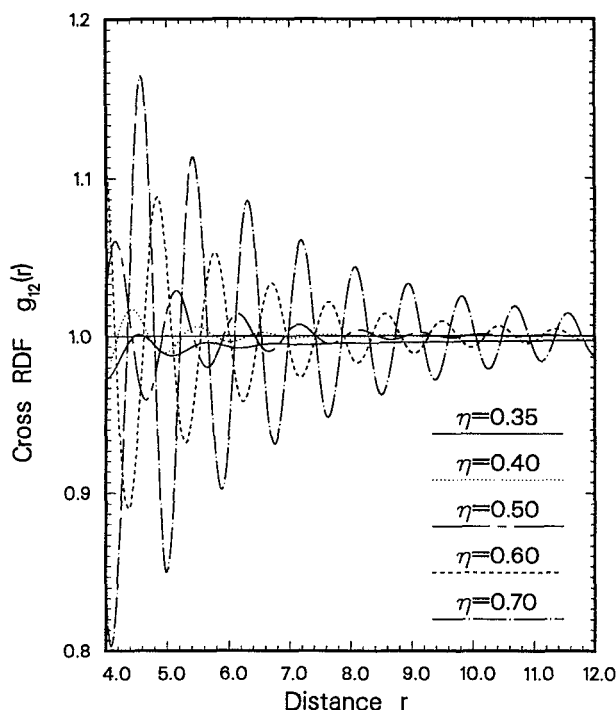


FIG. 16. Long-range detail of the RDF shown in Fig. 15.

V. THERMODYNAMIC STABILITY OF SOLUTIONS

Once a solution is found for the nonlinear system given by Eqs. (13) and (14), one should ask whether that solution is unique and whether it has physical significance. This most important question was already answered by Pastore,¹² who proved that whenever the Ornstein–Zernike equation with MSA closure has a solution, such a solution is unique (within the class of correlation functions corresponding to positive, finite structure factors) and physical. Therefore, for a given set of conditions, any solution of the OZ equation is guaranteed to be unique and physical. However, the Yukawa-MSA algorithm does not solve the OZ equation itself [Eq. (4) in the total correlation functions $h_{ij}(r)$] but its (Baxter) factorized form [Eqs. (8) and (9) in the factor correlation functions $Q_{ij}(r)$] which for the Yukawa-MSA problem can be expressed as Eqs. (13) and (14). As noted by Baxter,¹¹ the factorization of the OZ equation requires the matrix of factor correlation functions [see Eq. (53) below] to be invertible. This condition is equivalent to the absence of infinitely ranged correlation functions.

Therefore the first thing to check in any solution—given by a set of coefficients of the factor correlation functions $Q_{ij}(r)$ —is whether it corresponds to an invertible matrix. Unfortunately, this was not done in Ref. 6 as pointed out by Pastore.¹²

We begin by proposing a simplified criterion to determine the acceptability of solutions. A general discussion of range of correlation functions and thermodynamic stability will follow.

Based on the work by Pastore,¹² the following simplified criterion can be used to detect nonphysical solutions:

$$\text{If } \Delta(0) = \det[\delta_{ij} - (\rho_i \rho_j)^{1/2} \bar{Q}_{ij}] < 0 \Rightarrow \text{reject solution}, \quad (48)$$

where the \bar{Q}_{ij} quantities are given by Eqs. (44) and (45). Otherwise, the solution satisfies both the factorized and original OZ equations, and hence such a solution is both unique and physical.

The first (rejecting) part of this criterion is taken directly from Pastore and is rigorously exact. The second (accepting) part is not necessarily true from a theoretical point of view; it is rather a practical rule that we have found reliable in working with a variety of pure components and mixtures.

Actually, the invertibility of the $Q_{ij}(r)$ matrix requires that $\Delta(s)$ have no zeros in the right half-plane of the s variable, where $\Delta(s)$ is defined as

$$\Delta(s) = \det[\delta_{ij} - (\rho_i \rho_j)^{1/2} \hat{Q}_{ij}(s)] \quad (49)$$

and $\hat{Q}_{ij}(s)$ are the Laplace transforms of the factor correlation functions, i.e.,

$$\hat{Q}_{ij}(s) = \int_{\lambda_{ij}}^{\infty} e^{-sr} Q_{ij}(r) dr. \quad (50)$$

For s real, $\Delta(s)$ is real and continuous, and $\lim_{s \rightarrow \infty} \Delta(s) = 1$. Therefore, if $\Delta(0) < 0$, then $\Delta(s)$ must have at least one zero on the real axis and the solution is nonphysical. However, $\Delta(0) > 0$ does not guarantee the absence of zeros at any other point in the right half-plane. To find out if such zeros exist, Pastore proposes a second check in which the total variation of the argument of $\Delta(s)$ is calculated on a closed half-circle (in the right half-plane) centered on $s = 0$. The radius of that circle must be sufficiently large to enclose the nearest zero (when such zeros exist).

Pastore's second check is relatively easy to implement but (using the recommended interval lengths along the half-circle) it takes considerably longer than the solution itself. We have found no realistic cases in which the second check disagrees with the simpler first one, Eq. (48). The only exception (in agreement with Pastore) was obtained for negative G_{vij} solutions, whose nonphysical character is self-evident since they imply negative radial distribution functions, see Eq. (15). These negative G_{vij} solutions cannot be reached by the Yukawa-MSA algorithm [i.e., starting from the initial estimate given by Eqs. (23) and (24) and using Newton–Raphson iterations]. In addition, as will be discussed below, the most appropriate value of s to detect the divergence of fluid solutions is $s = 0$.

A. Discussion of correlation range and thermodynamic stability

The Fourier-transformed OZ equation is given by

$$\sum_j [\delta_{ij} - \rho_i \tilde{c}_{ij}(k)] \tilde{h}_{ij}(k) = \tilde{c}_{ij}(k), \quad (51)$$

where

$$\tilde{h}_{ij}(k) = 4\pi \int_0^{\infty} \frac{\sin kr}{kr} r^2 h_{ij}(r) dr \quad (52)$$

are the three-dimensional Fourier-transformed total correlation functions (or FTCTF, for brevity), and $\tilde{c}_{ij}(k)$ are simi-

larly defined. In the absence of infinitely ranged correlations, i.e., if $\tilde{h}_{ij}(k) < \infty$ for all real values of k , the Fourier-transformed direct correlation functions can be factorized according to

$$\delta_{ij} - (\rho_i \rho_j)^{1/2} \tilde{c}_{ij}(k) = \sum_l [\delta_{il} - (\rho_i \rho_l)^{1/2} \hat{Q}_{il}(-ik)] \times [\delta_{jl} - (\rho_j \rho_l)^{1/2} \hat{Q}_{jl}(ik)], \quad (53)$$

where the Laplace transforms $\hat{Q}_{ij}(s) = \pm ik$ are given by Eq. (50) (the i 's inside the parenthesis denote the imaginary unit, as opposed to the subscript i , which refers to the components in the mixture). After inverse Fourier transformation, Eqs. (51) and (53) give rise to Eqs. (8) and (9) which in turn lead to Eqs. (13) and (14).

The FTCTF are important in the determination of several thermodynamic and structural characteristics of the fluid. The FTCTF values are best calculated analytically in the following way: (1) after obtaining a Yukawa-MSA solution (G_{vij} , D_{vij}) for the nonlinear Eqs. (13) and (14), the other parameters (a_{ij} , b_{ij} , C_{vij}) of the factor correlation functions $Q_{ij}(r)$ are given by Eqs. (25) to (28), while the functions themselves are defined by Eqs. (10) and (11); (2) then Eqs. (50) and (53)—which is more conveniently expressed in the style of Eq. (43)—yield the $\tilde{c}_{ij}(k)$ quantities; (3) finally, the linear system represented by Eq. (51) is solved to produce the FTCTF.

Generally, though, the quantity of interest will not be the specific values of the FTCTF, but rather their order of magnitude. In this sense, it is obvious that the values of all $\tilde{h}_{ij}(k)$ are inversely proportional to the determinant of the matrix of coefficients in Eq. (51). For this reason, that determinant is represented by $R^{-1}(k)$ and is given the name *inverse correlation range* in this work. Thus $R^{-1}(k)$ is defined as

$$R^{-1}(k) = \det[\delta_{ij} - \rho_j \tilde{c}_{ij}(k)]. \quad (54)$$

Since $\det[\delta_{ij} - \rho_j \tilde{c}_{ij}(k)] = \det[\delta_{ij} - (\rho_i \rho_j)^{1/2} \tilde{c}_{ij}(k)]$, then from Eq. (53)

$$R^{-1}(k) = \Delta(ik) \Delta(-ik), \quad (55)$$

where $\Delta(s) = \pm ik$ is given by Eq. (49). This makes evident why the conditions of finite correlation range [$R^{-1}(k) \neq 0$ for any real k] and of $Q_{ij}(r)$ matrix invertibility [$\Delta(s) \neq 0$ in the right half-plane of s] are completely equivalent. When a particular Yukawa-MSA solution meets these conditions, that solution satisfies the OZ equation and consequently it is unique and physical.

Using Eq. (51), the correlation range can be expressed in terms of the FTCTF,

$$R(k) = \det[\delta_{ij} + (\rho_i \rho_j)^{1/2} \tilde{h}_{ij}(k)]. \quad (56)$$

To clarify the following discussion of thermodynamic stability, we will assume that the fluid mixture being studied is binary; in that case, the previous equation results in

$$R(k) = 1 + \rho_1 \tilde{h}_{11}(k) + \rho_2 \tilde{h}_{22}(k) + \rho_1 \rho_2 [\tilde{h}_{11}(k) \tilde{h}_{22}(k) - \tilde{h}_{12}(k) \tilde{h}_{21}(k)]. \quad (57)$$

For a valid Yukawa-MSA solution, the FTCTF, $\tilde{h}_{ij}(k)$,

yielded by Eq. (51) are related to the fluid structure factors. In the case of a binary mixture, these structure factors are given by the following expressions (Bhatia and Thornton¹⁷):

$$S_{CC}(k) = x_1 x_2 \{1 + \rho x_1 x_2 [\tilde{h}_{11}(k) + \tilde{h}_{22}(k) - 2\tilde{h}_{12}(k)]\}, \quad (58)$$

$$S_{NN}(k) = 1 + \rho [x_1^2 \tilde{h}_{11}(k) + x_2^2 \tilde{h}_{22}(k) + 2x_1 x_2 \tilde{h}_{12}(k)], \quad (59)$$

$$S_{NC}(k) = \rho x_1 x_2 \{x_1 [\tilde{h}_{11}(k) - \tilde{h}_{12}(k)] - x_2 [\tilde{h}_{22}(k) - \tilde{h}_{12}(k)]\}. \quad (60)$$

These structure factors are important in the determination of (among other properties) the electrical conductivity of metals (solid or liquid) and fused salts, and also in the evaluation (with $k = 0$) of transport properties of ordinary fluids (see Ref. 17). The thermodynamic significance of these quantities is examined later.

There are two basic kinds of RDF behavior that can lead to infinite FTCTF. Under some conditions (very high densities and low temperatures) the $h_{ij}(r)$ may show strong fluctuations around zero even at large intermolecular distances r . As a result, the amplitude of these fluctuations may decrease too slowly for Eq. (52) to yield a finite $\tilde{h}_{ij}(k)$. In this case, $R^{-1}(k)$ will vanish for some $k \neq 0$. For pure components, the value of k most likely to cancel R^{-1} will be a multiple of $2\pi/\lambda$, where λ is the period of the fluctuations; this period will be approximately equal to that of the PY hard-sphere RDF. This kind of strong periodic arrangement, however, can appear only in solids. Furthermore, not even solids exhibit a sufficiently strong *radial* periodic arrangement to produce infinite $\tilde{h}_{ij}(k \neq 0)$. None of the mixtures studied in this work produced a zero R^{-1} for a $k \neq 0$ in the $0 \leq \eta \leq 0.70$ range (higher packing fractions were not investigated because $\eta = 0.74$ already produces close packing in pure fluids).

The reason for the appearance of infinite FTCTF in fluids is different. In this case, the molecules do not exhibit any particular arrangement and, therefore infinitely ranged *fluctuations* are not possible. However, for some conditions, the RDFs may become essentially monotonic (as in Figs. 10, 11, and 16), producing $h_{ij}(r)$ functions that stay constantly above or below zero. If these functions vanish too slowly with distance, the FTCTF become infinite, and the corresponding RDFs are said to be nonconvergent. From Eq. (52) it is clear that the value of the inverse wavelength k that must be used to detect this lack of convergence is $k = 0$. Therefore $R^{-1}(k = 0)$, or $\Delta(0)$, is all that is needed to determine the physical acceptability of Yukawa-MSA solutions for fluids.

The long-wavelength limit, $k = 0$, presents the case for which the determinant R^{-1} is easiest to calculate: Eqs. (43) and (48) can be combined with Eq. (55) to yield $R^{-1}(0) = [\Delta(0)]^2$. In particular, for pure components [or for pseudomixtures in which all interactions, and therefore all $\tilde{c}_{ij}(0)$, are equal] $R^{-1}(0)$ is equal, see Eq. (54), to their inverse isothermal compressibility,

$$\text{Pure components: } R^{-1}(0) = \chi^{-1}, \quad (61)$$

where χ^{-1} is given by Eq. (34). For either pure components or mixtures, at infinite temperature, the MSA (or Percus–Yevick) solution for hard spheres is obtained, yielding

$$\text{Infinite temperature: } R_{HS}^{-1}(0) = \frac{(1+2\eta)^2}{(1-\eta)^4}, \quad (62)$$

i.e., the Percus–Yevick (PY) compressibility equation. It is interesting to note that, for hard-sphere mixtures, Eq. (62) remains valid regardless of composition or diameter ratio. In other words, for hard spheres there is no difference in $R^{-1}(0)$ between pure components and mixtures. (Consequently, hard-sphere mixtures cannot undergo fluid–fluid separations into phases of different composition.)

In addition, for $k=0$, the structure factors [see Eqs. (58) to (60)] acquire thermodynamic significance. They become related to properties that determine the thermodynamic stability of the fluid.¹⁷ These relations are given by

$$S_{CC}(0) = NkT / \left(\frac{\partial^2 G}{\partial x_i^2} \right)_{T,P,N}, \quad (63)$$

$$S_{NN}(0) = \chi + \delta^2 S_{CC}(0), \quad (64)$$

$$S_{NC}(0) = -\delta S_{CC}(0), \quad (65)$$

where χ is the isothermal compressibility as defined (through its inverse) by Eq. (34), and δ is a dilatation factor defined by

$$\delta = \frac{\bar{v}_1 - \bar{v}_2}{x_1 \bar{v}_1 + x_2 \bar{v}_2} = \rho(\bar{v}_1 - \bar{v}_2), \quad (66)$$

where \bar{v}_i are the partial molar volumes. The quantities $S_{NN}(0)$ and $S_{CC}(0)$ represent, respectively, the mean square fluctuations in the density (or particle number, N) and composition (or concentration, C), and $S_{NC}(0)$ is the correlation between these two fluctuations.

For a given composition, density, and temperature, a fluid can present a single homogeneous phase only if the thermodynamic stability requirements are satisfied. For pure components, the fluid must possess *mechanical* stability,

$$\text{mechanical stability: } \chi^{-1} \geq 0. \quad (67)$$

That is, at constant temperature the pressure cannot decrease with increasing density. For mixtures, the fluid must have both mechanical and *material* (or *diffusional*) stability. The latter requirement can be expressed as

$$\text{material stability: } \left(\frac{\partial^2 G}{\partial x_i^2} \right)_{T,P,N} \geq 0. \quad (68)$$

If, for some particular conditions, the fluid does not satisfy Eq. (68), then its overall Gibbs free energy can be decreased (while maintaining constant temperature and pressure) by splitting it into two phases of different composition. This phase separation may correspond to either vapor–liquid or liquid–liquid equilibria. Generally, before reaching the instability limit fluids undergo phase separation. That limit is reached only at the critical point of the phase separation.

Therefore the onset of mechanical instability can be detected, through Eqs. (64) and (67), by checking whether

$S_{NN} = \infty$. Similarly, the appearance of material instability is revealed by $S_{CC} = \infty$, see Eqs. (63) and (68). However, finding out whether the correlation range is infinite, i.e., $R^{-1}(0) = 0$ or $\Delta(0) = 0$, provides a better way of determining the spinodal limit (separating the thermodynamically stable region from the unstable one) since it combines the strengths of both previous checks.

For pure fluids, mechanical instability, $\chi^{-1} = 0$ (a need to separate into phases of different density), leads through Eq. (61) to $R^{-1}(0) = 0$. For mixtures, material instability (a need to separate into phases of different composition) requires $S_{CC} = \infty$ in Eq. (63), which in turn necessitates infinite $\tilde{h}_{ik}(0)$ and thus $R^{-1}(0) = 0$. A zero inverse correlation range, $R^{-1}(0)$, must also result in the rare cases in which a mixture reaches mechanical instability while remaining materially stable, i.e., in cases of *azeotropic instability*. From Eqs. (63) to (65), the inverse isothermal compressibility can be written as

$$\chi^{-1} = [S_{NN}(0) - S_{NC}^2(0)/S_{CC}(0)]^{-1}. \quad (69)$$

The only way to make the left-hand side zero (mechanical instability) is by having the quantity inside the brackets equal to infinity. This, in turn, requires infinite $\tilde{h}_{ij}(0)$ [see Eqs. (59) and (60)] and therefore $R^{-1}(0) = 0$. Thus the presence in a mixture of mechanical instability (infinite FTCTF) while material instability is preserved [finite $S_{CC}(0)$, see Eq. (63)] requires the FTCTF in Eq. (58) to satisfy

$$\text{azeotropic instability: } \tilde{h}_{12}(0) = \frac{1}{2}[\tilde{h}_{11}(0) + \tilde{h}_{22}(0)]. \quad (70)$$

Consequently, at an azeotropic instability the $S_{CC}(0)$ factor of a mixture is exactly equal to that for a pseudomixture, formed by identical components with equal $\tilde{h}_{ij}(0)$: $S_{CC}(0) = x_1 x_2$. In addition, the difference between the partial molar volumes of the two components in the binary mixture becomes $\bar{v}_1 - \bar{v}_2 = \frac{1}{2}[\tilde{h}_{11}(0) - \tilde{h}_{22}(0)]$. Finally, after substituting the previous results in Eqs. (69) and (57), a simple comparison reveals that at an azeotropic instability $R^{-1}(0) = \chi^{-1} = 0$.

In conclusion, whenever either kind of thermodynamic instability is reached, both $R^{-1}(0)$ and $\Delta(0)$ must become zero. It should be noted, that since $R_{HS}^{-1}(0)$ cannot be zero, see Eq. (62), hard-sphere mixtures cannot undergo any type of fluid–fluid separation. Therefore the mixtures studied here must be thermodynamically stable at the infinite temperature limit.

Previously stability of single-Yukawa-tail mixtures was studied by Abramo, Caccamo, and Giunta¹⁸ (only equidiameter case) and by Arrieta *et al.*⁶ A Monte Carlo study of structure and phase separation (again only equidiameter case) was performed very recently by Hoheisel and Zhang.¹⁹

The dashed lines drawn in Figs. 3 to 6 correspond to conditions for which $\Delta(0)$, or $R^{-1}(0)$, is zero. Therefore these are the thermodynamic instability (or spinodal) lines. The points composing these lines fall inside the phase separation envelope (with the single exception of the critical point). For the pure components, the highest temperature

peak of the instability lines is the compressibility determined critical point. The region between the instability and no-solution lines correspond to unstable, nonphysical solutions for which $\Delta(0)$ is negative. Here solutions to Eqs. (13) and (14) can be found, but none of those solutions satisfy the OZ equation, Eq. (4). By studying two examples, the next subsection will present a simple way to determine these instability or spinodal lines and will investigate how to predict the type of phase separation associated to those lines well before instability is reached.

B. Study of fluid separation as the spinodal temperature is approached

This subsection studies the variation with decreasing temperature of the inverse correlation range, $R^{-1}(0)$, and the FTCF, $\tilde{h}_{ij}(0)$, along the *physical branch* of MSA solutions. The physical branch is defined as the one extrapolating to the correct infinite temperature, Percus-Yevick (PY) limit [$\Delta(0) = + (1 + 2\eta)/(1 - \eta)^2$ and G_{vij} given by Eq. (24)]. Other nonphysical solution branches exist for the nonlinear MSA Eqs. (13) and (14) (but not for the OZ equation). Points along these nonphysical branches are characterized by negative values of either $\Delta(0)$ or G_{vij} . In the range of fluid conditions, the Yukawa-MSA algorithm [which starts at the correct infinite temperature limit, Eqs. (23) and (24)] yields solutions belonging to the physical branch. However, not all solutions along the physical branch are themselves physical. For a given composition x_i and packing fraction η , there is a *spinodal* temperature, T_{sp} , separating the thermodynamically stable region [$T > T_{sp}$, $\Delta(0) > 0$] from the unstable one [$T \leq T_{sp}$, $\Delta(0) \leq 0$]. Although the determination of the spinodal temperature itself should be based on $\Delta(0)$, more physical insight can be gained by observing the variation of the inverse correlation range, $R^{-1}(0) = [\Delta(0)]^2$, as temperature decreases. Two representative cases will be investigated: ideal mixture M1 at moderate density, and nonideal mixture M2 at high density.

Figures 17 to 21 correspond to mixture M1 at $x_1 = 0.50$ and $\eta = 0.17$. For this case, Fig. 17 shows the variation of $R^{-1}(0)$ with temperature. At high temperatures, $T \gg 20.0$, $R^{-1}(0)$ is practically equal to the analogous value for hard spheres, $R_{HS}^{-1}(0)$. As T decreases so does $R^{-1}(0)$ until it vanishes on the spinodal line (at $T_{sp} = 1.595$ in this case). Below this point, the increasing $R^{-1}(0)$ is due to unstable, nonphysical solutions [$\Delta(0) < 0$] which quickly disappear as the no-solution region is entered. Figure 18 is entirely equivalent to the previous graph, but here the inverse temperature has been used as abscissa. Figure 19 presents the concurrent variation of the long wavelength ($k = 0$) FTCF, $\tilde{h}_{ij}(0)$, with temperature. In this case, all three independent $\tilde{h}_{ij}(0)$ diverge to $+\infty$ as T_{sp} is approached. This has a straightforward physical interpretation: as the kinetic energy of the molecules diminishes, the interaction potential draws them towards lower energy, more closely packed configurations, producing thus *molecular aggregation*. Therefore the driving force towards instability, and the consequent phase separation, is a need for greater density. As can be seen in Fig. 3 for $\eta = 0.17$ and $x_1 = 0.50$, at high temperature this

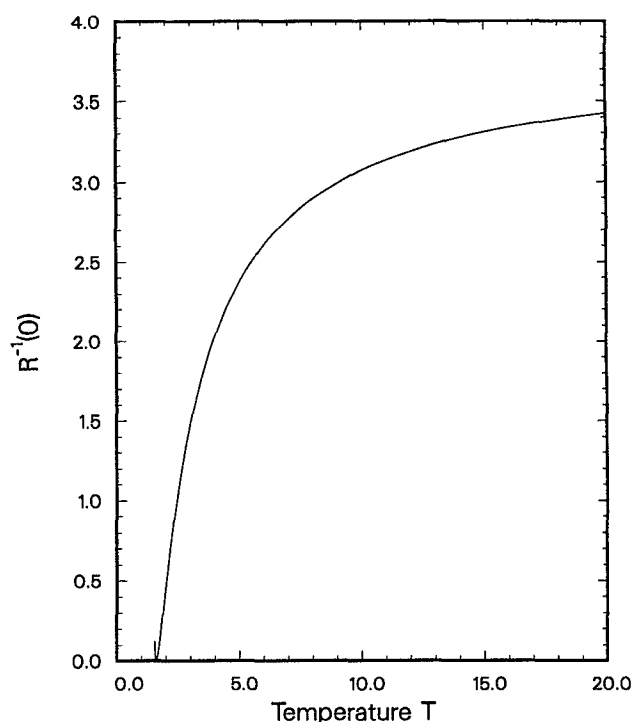


FIG. 17. Variation of the inverse correlation range $R^{-1}(0)$ defined by Eq. (54), with temperature for mixture M1 at $x_1 = 0.50$, $\eta = 0.17$.

mixture appears as a homogeneous vapor phase. If T is lowered sufficiently, this vapor phase will start condensing, thus satisfying that need for higher density.

Figures 20 and 21 compare the RDFs for points above and below the spinodal temperature $T_{sp} = 1.595$. For

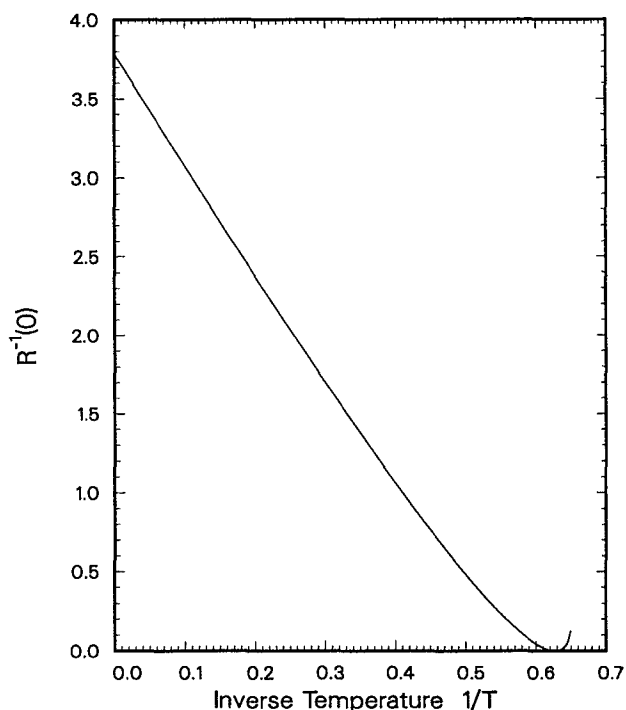


FIG. 18. Variation of the inverse correlation range $R^{-1}(0)$ defined by Eq. (54), with inverse temperature for mixture M1 at $x_1 = 0.50$, $\eta = 0.17$.

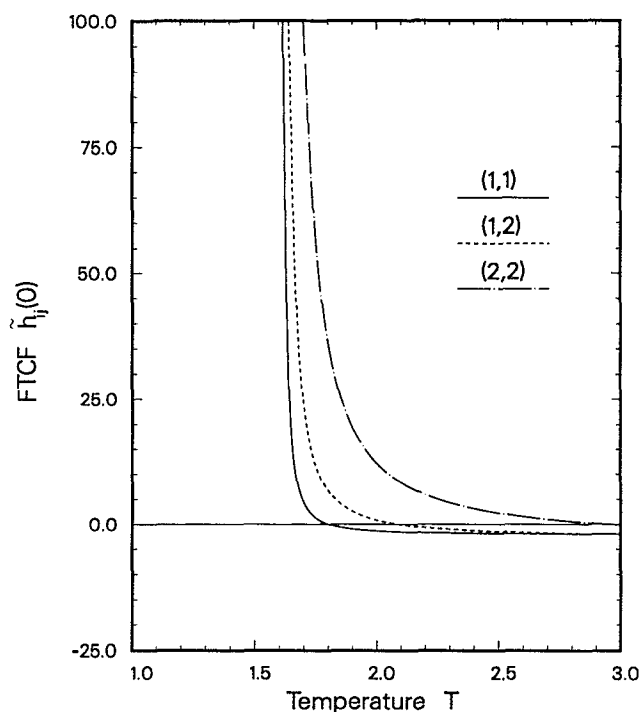


FIG. 19. Variation of the Fourier-transformed ($k = 0$) total correlation functions (FTCF), $\tilde{h}_{ij}(0)$, with temperature for mixture M1 at $x_1 = 0.50$, $\eta = 0.17$. The spinodal (infinite range) temperature is $T_{sp} = 1.595$.

$T = 2.50$, Fig. 20, the RDFs appear completely normal. For $T = 1.570$, however, the RDFs in Fig. 21 are obviously non-convergent, since all three $g_{ij}(r)$ remain above unity as $r \rightarrow \infty$. This is the result of the tendency shown in Fig. 19: as

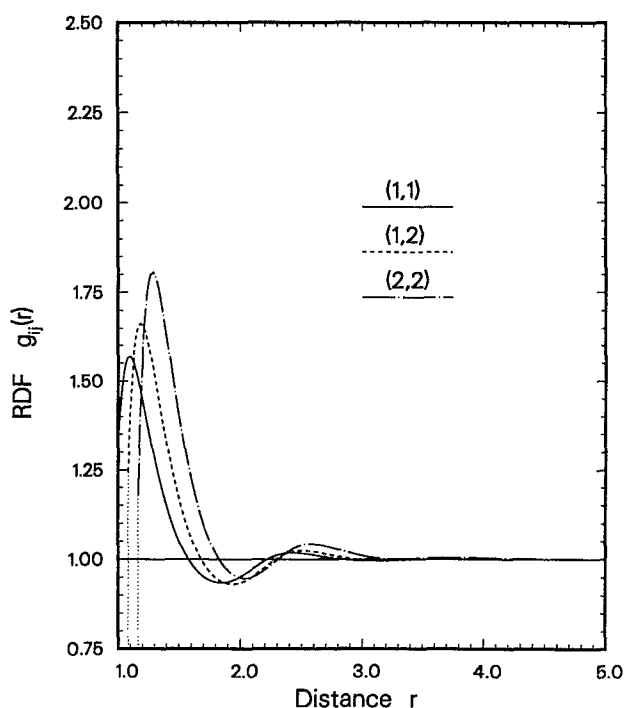


FIG. 20. Stable, convergent RDF for mixture M1 at $x_1 = 0.50$, $\eta = 0.17$, $T = 2.500$.

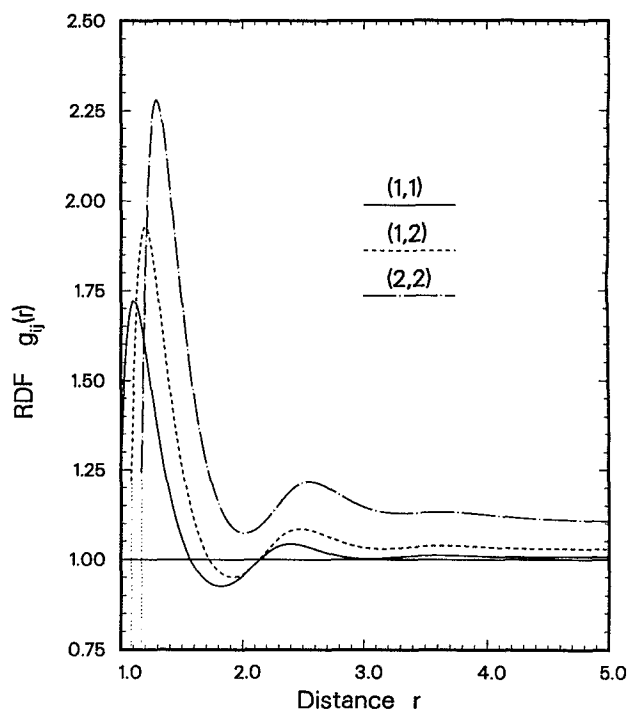


FIG. 21. Unstable, nonconvergent RDF for mixture M1 at $x_1 = 0.50$, $\eta = 0.17$, and $T = 1.570$.

T decreases, each molecule surrounds itself with an increasing number of like- and unlike-particles. For temperatures $T < T_{sp}$, this tendency is so strong that it can no longer be satisfied with the average densities, ρ_i , present in the mixture. In Fig. 21 the interaction potential has forced such a degree of molecular aggregation that the RDFs break through the physical barrier imposed by the average densities. Observe also that the divergence order in Fig. 19 is $\tilde{h}_{22}(0) > \tilde{h}_{12}(0) > \tilde{h}_{11}(0)$, in agreement with the divergence order for the $g_{ij}(r)$ in Fig. 21.

Finally, Fig. 22 shows the change in Gibbs free energy upon mixing, ΔG_{mix} , for mixture M1 for conditions similar to those studied above. This graph shows how the phase separation develops with decreasing temperature. Figure 23 presents the variation in packing fraction needed to keep pressure constant. The pressures were chosen to make all lines pass through $\eta = 0.17$ at $x_1 = 0.50$. Table V gives the approximate equilibrium data (determined graphically). Both the pronounced variation of η in Fig. 23 and its equilibrium values in Table V (compare with Fig. 3) clearly indicate that a vapor-liquid transition is taking place. The relative difference between the equilibrium compositions, x_2^V and x_2^L , is considerably smaller than that between η^V and η^L . This confirms that the main driving force in this phase separation is the change in density, with the change in composition playing a secondary role.

Figures 24 to 30 examine the thermodynamic stability of mixture M2 at $x_1 = 0.75$ and $\eta = 0.54$. For those conditions, Figs. 24 and 25 show the variation of $R^{-1}(0)$ with temperature and with inverse temperature, respectively. The behavior of $R^{-1}(0)$ is smooth and entirely similar to that

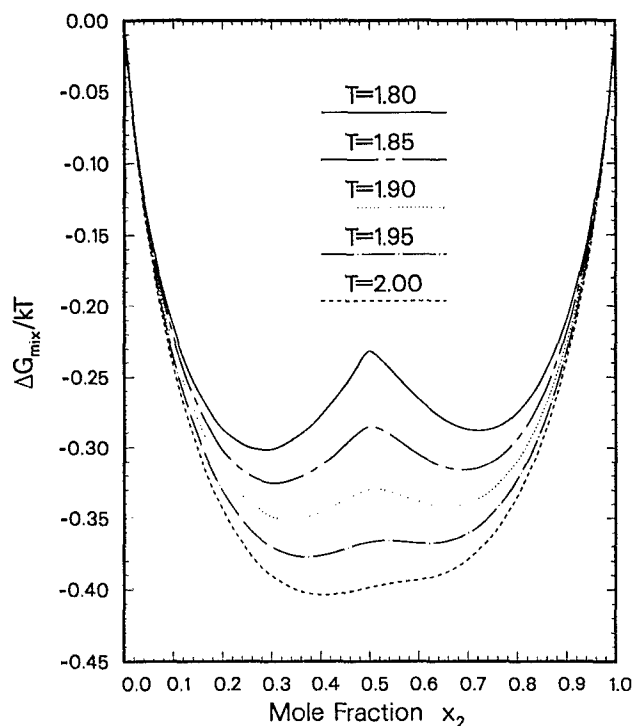


FIG. 22. Change of Gibbs free energy upon mixing $\Delta G_{\text{mix}}/kT$ for mixture M1 at the temperatures indicated. The pressures, packing fraction range, and equilibrium data are given in Table V.

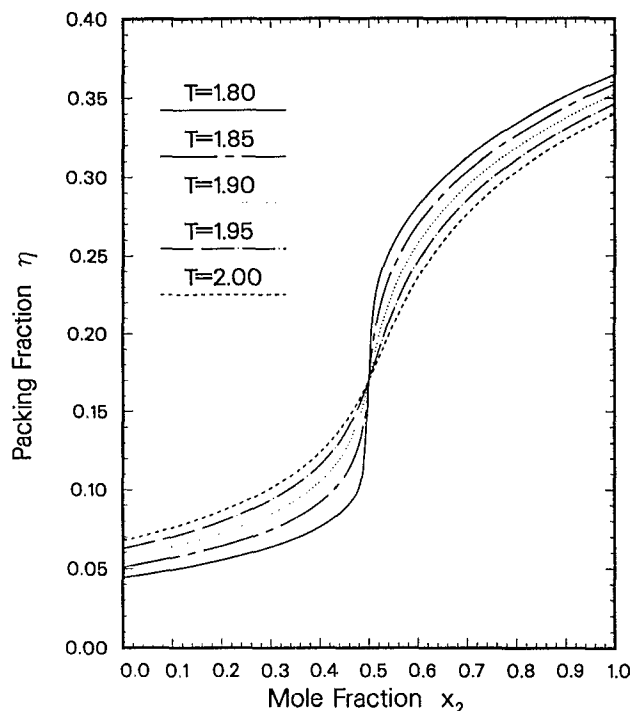


FIG. 23. Isobaric variation of the packing fraction with composition for mixture M1 at the temperatures indicated. The pressures, packing fraction range, and equilibrium data are given in Table V.

TABLE V. Equilibrium properties from change in Gibbs free energy upon mixing.

| Mixture | kT/ϵ_{11}^* | $P\sigma_{11}^3/\epsilon_{11}^*$ | $\eta(x_2=0)$ | $\eta(x_2=1)$ | Equilibrium | | Equilibrium | |
|---------|----------------------|----------------------------------|---------------|---------------|-------------|------------|-------------|-------------|
| | | | | | x_2^I | x_2^{II} | η^I | η^{II} |
| M1 | 2.00 | 0.240 | 0.068 | 0.340 | 0.45 | 0.61 | 0.142 | 0.241 |
| | 1.95 | 0.214 | 0.063 | 0.346 | 0.40 | 0.64 | 0.116 | 0.264 |
| | 1.90 | 0.189 | 0.057 | 0.353 | 0.35 | 0.67 | 0.093 | 0.285 |
| | 1.85 | 0.164 | 0.051 | 0.359 | 0.31 | 0.71 | 0.076 | 0.306 |
| | 1.80 | 0.139 | 0.044 | 0.365 | 0.29 | 0.73 | 0.063 | 0.319 |
| M2 | 1.00 | 6.654 | 0.494 | 0.588 | ... | ... | ... | ... |
| | 0.90 | 5.639 | 0.495 | 0.586 | ... | ... | ... | ... |
| | 0.80 | 4.627 | 0.497 | 0.584 | 0.07 | 0.43 | 0.513 | 0.557 |
| | 0.70 | 3.618 | 0.500 | 0.581 | 0.03 | 0.59 | 0.506 | 0.566 |
| | | | | | | | | |

observed for the ideal mixture M1 at a much lower packing fraction. The spinodal temperature separating the stable and unstable regions is $T_{\text{sp}} = 0.692$. In this case, the width of the unstable band between the spinodal line and the no-solution region is minimal. The corresponding variation of the $\tilde{h}_{ij}(k)$ with temperature is given by Fig. 26. Here $\tilde{h}_{11}(k)$ and $\tilde{h}_{22}(k)$ diverge to $+\infty$ as T_{sp} is approached, but (unlike for mixture M1 in Fig. 19) $\tilde{h}_{12}(k)$ goes to $-\infty$. This indicates that when T decreases, molecules of component 1 tend to surround themselves with like-molecules, molecules of 2 behave in a parallel way, and both types of molecules try to avoid the company of unlike-molecules. The reason for this *molecular segregation* is the interaction potential: as T diminishes the potential becomes more dominant and the effect of all intermolecular attractions is strengthened, but then both like-molecule interactions prevail over the rela-

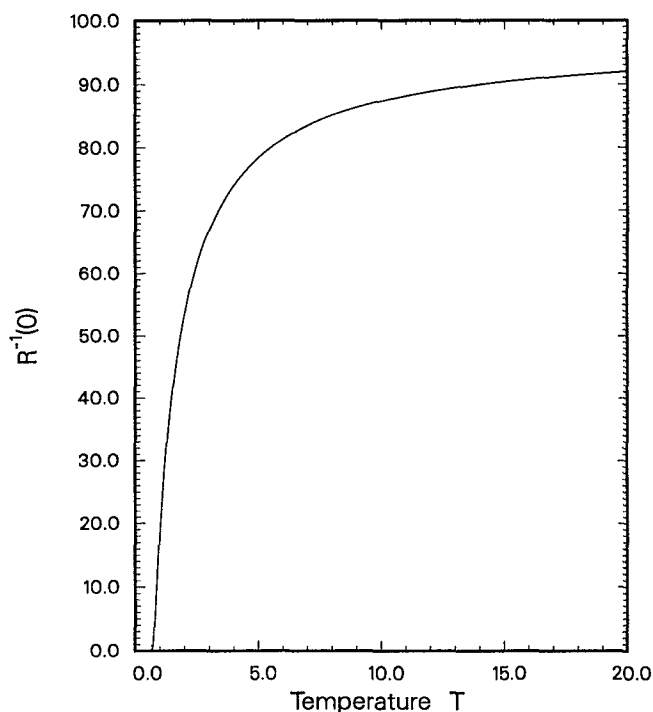


FIG. 24. Variation of the inverse correlation range $R^{-1}(0)$ defined by Eq. (54), with temperature for mixture M2 at $x_1 = 0.75$, $\eta = 0.54$.

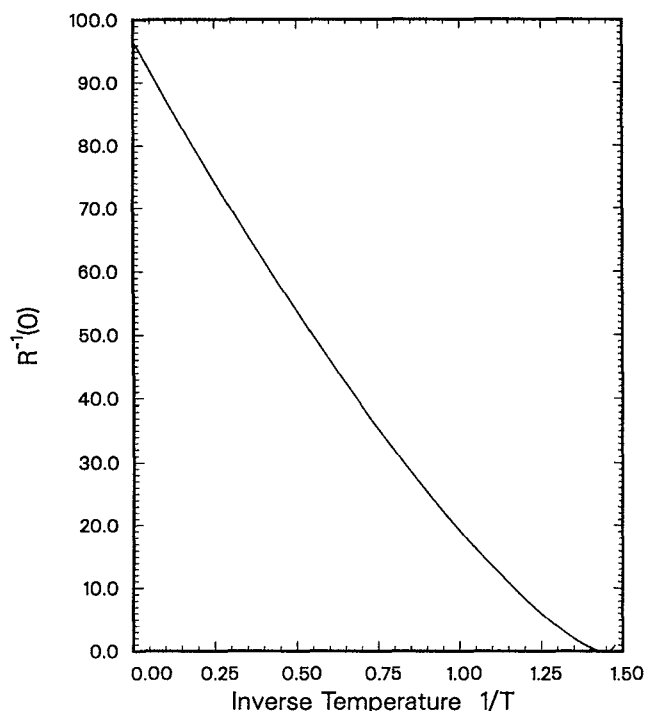


FIG. 25. Variation of the inverse correlation range $R^{-1}(0)$ defined by Eq. (54), with inverse temperature for mixture M2 at $x_1 = 0.75$, $\eta = 0.54$.

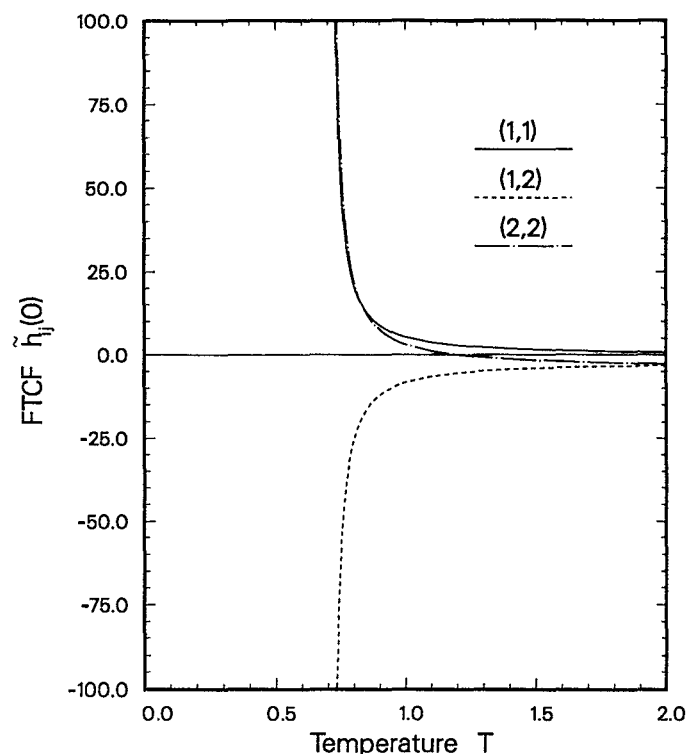


FIG. 26. Variation of the Fourier-transformed ($k=0$) total correlation functions (FTCF) $\tilde{h}_{ij}(0)$ with temperature for mixture M2 at $x_1 = 0.75$, $\eta = 0.54$. The spinodal (infinite range) temperature is $T_{sp} = 0.692$.

tively weaker (see Fig. 2) unlike-molecule potential. Therefore, in contrast to the case of mixture M1, here the driving force towards instability is molecular segregation into phases of different composition. In Fig. 4, for $x_1 = 0.75$ and $\eta = 0.54$, a decrease in temperature leads to a region of no-solution which corresponds to liquid-liquid separation.

Examples of RDFs on both sides of the spinodal temperature, $T_{sp} = 0.692$, are given in Figs. 27 and 28. For $T = 1.000$, Fig. 27 shows convergent RDFs. On the other hand, at $T = 0.685$ (Fig. 28) the RDFs do not converge to unity; both $g_{11}(r)$ and $g_{22}(r)$ stay above one [with the second slightly higher, which agrees with the $\tilde{h}_{ij}(0)$ in Fig. 26], while $g_{12}(r)$ remains below. Again, the tendency shown in Fig. 26 becomes so strong for $T \leq T_{sp}$ that it forces the RDFs beyond the limits imposed by the average densities.

The change in Gibbs free energy upon mixing, ΔG_{mix} , for mixture M2 is plotted in Fig. 29. The variation in packing fraction needed to keep pressure constant is presented in Fig. 30. The pressures were chosen to make all lines pass through $\eta = 0.54$ at $x_1 = 0.75$. The approximate equilibrium data are given in Table V. In this case, all packing fractions are clearly inside the liquid region, and their change with composition is relatively small. The difference between equilibrium values is more important for the composition, $x_2^{II} - x_2^I$, than for the packing fractions, $\eta^{II} - \eta^I$. Thus it is the change in composition that plays the more significant role in this liquid-liquid equilibrium.

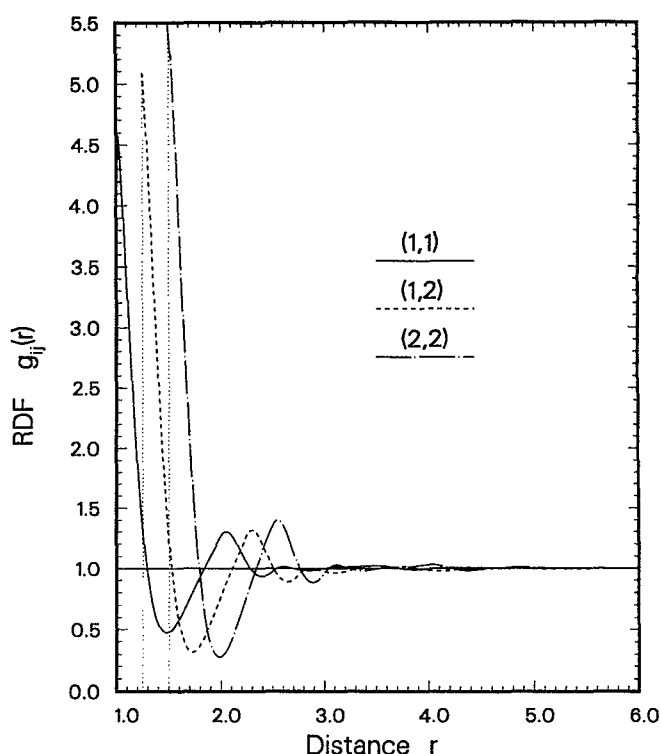


FIG. 27. Stable, convergent RDF for mixture M2 at $x_1 = 0.75$, $\eta = 0.54$, $T = 1.000$.

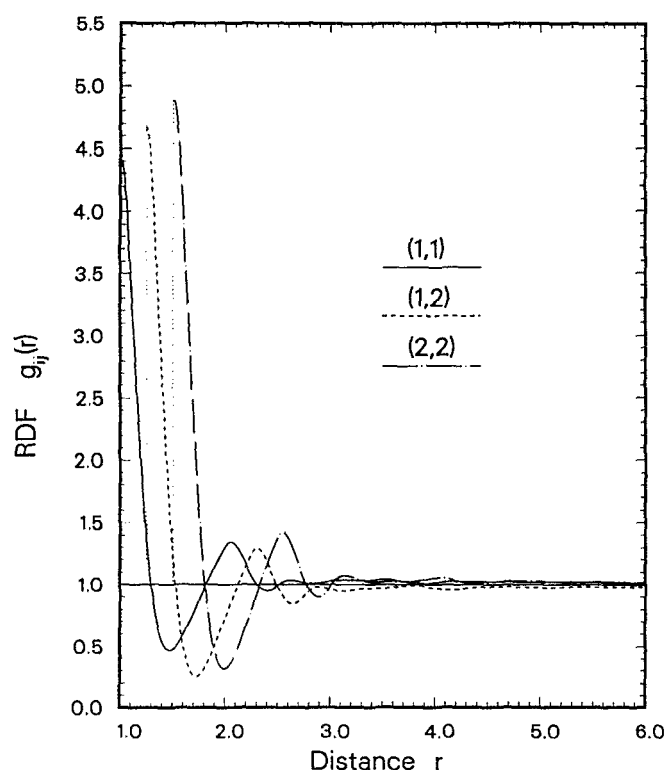


FIG. 28. Unstable, nonconvergent RDF for mixture M2 at $x_1 = 0.75$, $\eta = 0.54$, and $T = 0.685$.

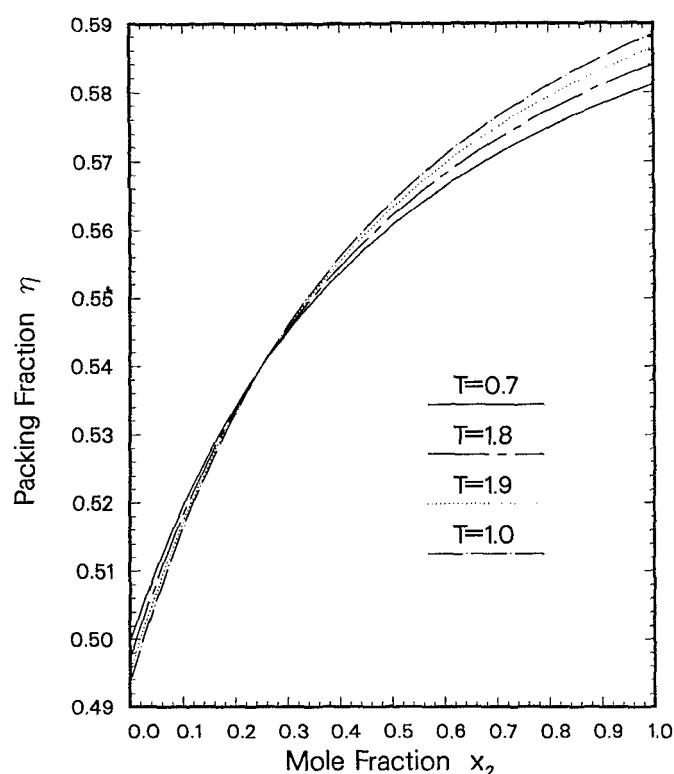


FIG. 30. Isobaric variation of the packing fraction with composition for mixture M2 at the temperatures indicated. The pressures, packing fraction range, and equilibrium data are given in Table V.

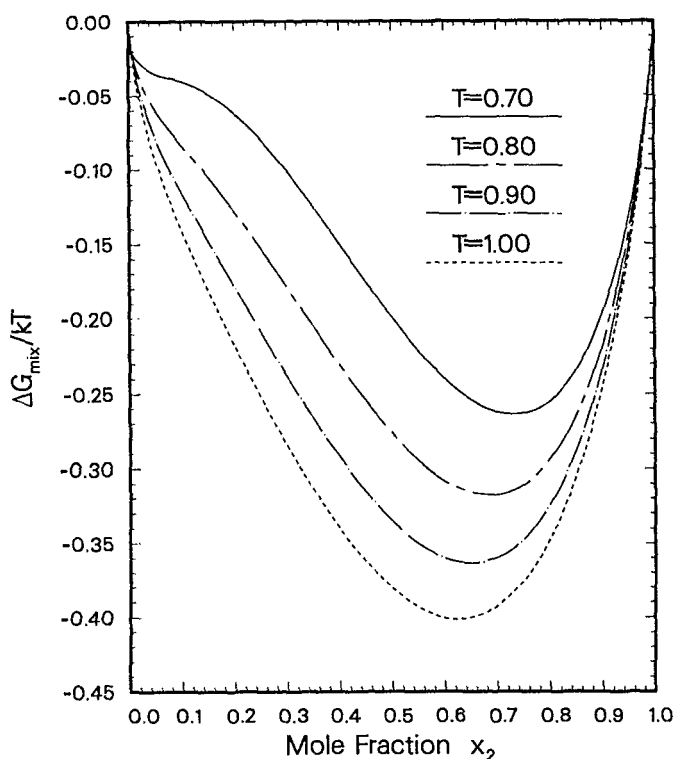


FIG. 29. Change of Gibbs free energy upon mixing $\Delta G_{\text{mix}}/kT$, for mixture M2 at the temperatures indicated. The pressures, packing fraction range, and equilibrium data are given in Table V.

Due to the thermodynamic inconsistency of the MSA, the virial, compressibility and energy equations will produce different results. In particular, Figs. 22, 23, 29, and 30 have been determined using the MSA energy equation (which, in contrast to the compressibility equation, yields the chemical potentials analytically). In these figures, the change of Gibbs free energy upon mixing was calculated, for a specific temperature and pressure (T, P) combination, through

$$\frac{\Delta G_{\text{mix}}}{kT}(\rho, x) \Big|_{T, P} = \sum_{i=1}^n x_i \left[\frac{\mu_i^r(\rho, x) - G_i^r(\rho_i^0, x_i = 1)}{kT} + \ln \frac{\rho x_i}{\rho_i^0} \right]_{T, P}, \quad (71)$$

where the density residual chemical potentials for the mixture μ_i^r and for the pure components G_i^r were given by Eq. (41) (plus the CMSL¹⁶ hard-sphere contribution), and where ρ and ρ_i^0 are, respectively, the mixture and pure component densities needed to produce pressure $P (= P^E)$ at temperature T .

In all cases observed the energy-derived mechanical and material instability points (e.g., the inflexion points in the curves given by Figs. 22 and 29) lie in the proximity but outside both the virial- and the compressibility-determined unstable regions. Therefore they correspond to proper solutions of the OZ equation. In Table IV, all points exhibit both mechanical and material stability from the MSA energy standpoint (and thus also according to the compressibility

and virial equations). However, point (M2, $x_1 = 0.50$, $\eta = 0.30$, $T = 1.70$) is very close to material instability, and both this point and (M1, $x_1 = 0.25$, $\eta = 0.34$, $T = 1.70$) are inside the energy-determined vapor–liquid envelope.

Some general conclusions can be drawn from the two examples studied above. From any given stable solution, a simple temperature derivative can yield, through $\partial R^{-1}(0)/\partial T$ and $\partial R^{-1}(0)/\partial(1/T)$, two complementary estimates of the instability point, see Figs. 17 and 18 (or Figs. 24 and 25). [Although the spinodal temperature itself is best determined using $\Delta(0)$, the temperature derivatives of the inverse correlation range give much better estimates.] For instance, at point (M1, $x_1 = 0.25$, $\eta = 0.34$, $T = 1.70$) the inverse correlation range is $R^{-1}(0) = 4.4436$ and a numerical derivative with respect to temperature yields $\partial R^{-1}(0)/\partial T = 5.9343$ and therefore $\partial R^{-1}(0)/\partial(1/T) = -17.1501$. The resulting estimates of the spinodal temperature are 0.9512, from the T derivative, and 1.1802, from the $(1/T)$ derivative, both close to the real value $T_{sp} = 1.1236$. Generally, the closer the stable solution is to the spinodal line, the smaller the difference between the estimates will be, yielding in turn a more accurate estimation. Thus one can estimate the distance (in temperature) from any stable solution to the instability point (and in a more general way, to the onset of phase separation). In addition, a similar temperature derivative of the FTCF, $\partial \hat{h}_{ij}(0)/\partial T$ (see Figs. 19 and 26), will indicate the type of phase separation to be expected for those conditions.

Therefore a calculation using few densities and compositions, taking a temperature derivative at each point, can produce a sufficiently accurate spinodal surface. This surface will reveal the shape and approximate location of the phase equilibrium envelope. The shape (see Figs. 3 to 6) will determine whether the mixture exhibits liquid–liquid equilibrium or not. The temperature derivative of the FTCF will produce an accurate picture of the type of equilibrium for each composition and density. Obviously, this information can be used to great advantage when determining the exact phase equilibrium envelope.

At high densities or packing fractions, however, there may exist no spinodal point. Pure fluids and ideal mixtures (which behave in the same qualitative way) show no instability $R^{-1}(0) = 0$ beyond a certain limit $\eta > \eta_{fs}$; here this limit, η_{fs} , will be called *forced stability packing*. As η increases, the spinodal temperature T_{sp} , for which $R^{-1}(0) = 0$, approaches the no-solution temperature T_{ns} (see Figs. 3 and 4). Eventually, at $\eta = \eta_{fs}$, both temperatures appear to coincide. From that point on, $R^{-1}(0)$ remains strictly positive for all temperatures, exhibiting minima whose value and location (T) increase with the packing fraction η . [Figure 31 shows this for mixture M1 at $x_1 = 0.50$. The inverse correlation ranges in this plot have been normalized, at each packing fraction, through division by the corresponding hard-sphere (or infinite temperature) quantity, $R_{hs}^{-1}(0)$.] Table VI gives the forced stability packing values, η_{fs} , for the two mixtures at the five compositions studied in this work. As can be seen, there is no limit for mixture M2 at the intermediate compositions, those which show liquid–liquid separation. Also worth noting, there is a

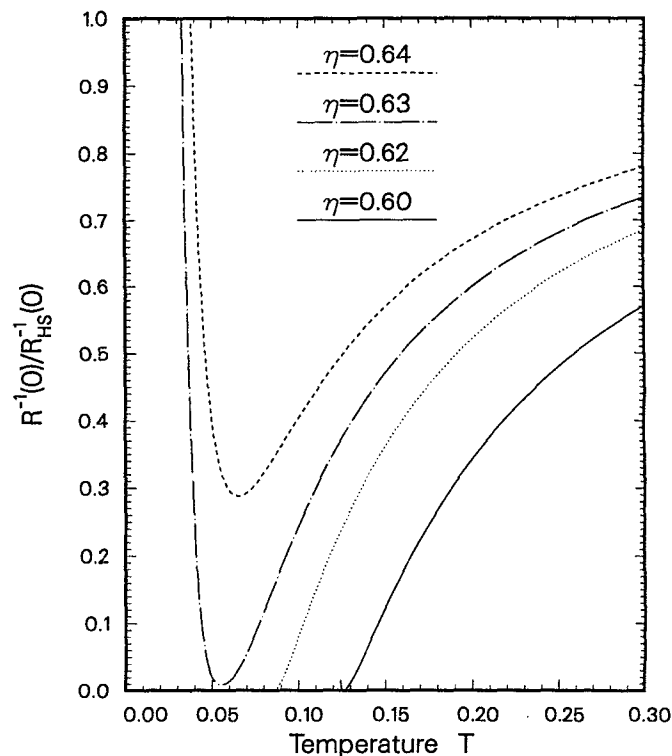


FIG. 31. Variation of the inverse correlation range $R^{-1}(0)$ (normalized by the corresponding hard-sphere quantity) for mixture M1 at $x_1 = 0.50$ and the packing fractions indicated. For this composition, M1 reaches forced stability at $\eta_{fs} = 0.629$.

significant difference between the η_{fs} values of the two first components of both mixtures. Their multi-Yukawa interactions, $\phi_{11}(r)$, were fitted to the same model Lennard-Jones potential, $\phi_{11}^{LJ}(r)$, but the results of the fitting are slightly different.

There are two possible sources of instability for a fluid: a density-driven vapor–liquid separation (the only possibility for pure components and ideal mixtures), and a composition-driven liquid–liquid separation. These instabilities, result from a balance between potential and kinetic energies in a dense fluid (i.e., a liquid) as its temperature is decreased at a constant packing fraction η (or for a given amount of fluid occupying a specified volume V).

Let us study first the case of vapor–liquid separation. As the temperature decreases, the diminished kinetic energy of molecules leaves them increasingly confined to lower potential energies, i.e., to shorter molecular distances (higher densities of saturated fluid). At the same time, the vapor molecules must move farther apart to avoid succumbing to the attractive forces. This explains the bell shaped form of vapor instability regions in Figs. 3 and 4.

TABLE VI. Forced stability packing, η_{fs} .

| Mixture | x_1 | | | | |
|---------|-------|-------|-------|-------|-------|
| | 1.00 | 0.75 | 0.50 | 0.25 | 0.00 |
| M1 | 0.534 | 0.647 | 0.629 | 0.599 | 0.544 |
| M2 | 0.541 | ... | ... | ... | 0.544 |

The forced stability packing, η_{fs} , depends on the shape of the interaction potential. For example, the first component of mixture M1, ($M1, i = 1$), has a lower η_{fs} than ($M2, i = 1$) because the minimum of its fitted three-Yukawa potential occurs at a slightly larger relative distance r/σ than that of the four-Yukawa interaction of ($M2, i = 1$). For pure components with attractive one-Yukawa interactions (for which the potential is minimum at $r = \sigma$), forced stability does not appear until $\eta_{fs} = 1$. In the MSA (or PY), $\eta = 1$ is the packing fraction at which hard spheres, completely devoid of any kinetic energy ($T = 0$), manage to occupy the full volume.

The MSA value of η_{fs} can only be taken as a qualitative indication of the true physical value, not only because the MSA underestimates the volume occupied by spherical hard cores, but also because the true configuration of minimum energy is likely to exhibit some ordered molecular arrangement (which cannot be represented through the MSA). In fact, for all compositions of both mixtures studied in this work, the nonzero minima of $R^{-1}(0)$ appear outside the fluid range, see the next section.

[Note: although the initial estimates given by Eqs. (23) and (24) are completely reliable in the search for fluid solutions, they may fail, for $\eta \sim \eta_{fs}$, at the extremely low temperatures studied in Fig. 31, yielding a nonphysical solution with $\Delta(0) < 0$. For these nonfluid conditions, one should start at a moderately low T , about one-tenth of the highest T_{sp} for a particular composition, and then use a stepwise solution method reducing T by small intervals ΔT . In any case, for these very low temperatures classical approach has to be replaced by quantum statistical mechanics.]

A second source of instability is possible for nonideal mixtures at high densities: liquid-liquid separation. This is why there is no forced stability packing, η_{fs} , for the intermediate compositions of mixture M2. In this case, as T decreases at constant η and a specific composition x_i , the effect of the interaction forces on the molecules grows stronger, and so does any possible imbalance between them, i.e., between the like- and unlike-particle attractions. If the latter are relatively weaker, as for mixture M2, a low T may make the specified composition unstable, forcing the molecules to segregate into two phases of different composition. An increased packing fraction will lead to shorter intermolecular distances, for which the interaction forces (and any imbalance) are more pronounced. Thus instability will be reached earlier, at a higher temperature T_{sp} . This results in the positive slope of the liquid-liquid instability curves of Fig. 4.

VI. HIGH DENSITY LIMITS

This section determines the high density limits beyond which the MSA solutions are no longer physically valid. Both the MSA itself and the CMSL¹⁶ equation, used for the hard-sphere contributions, continue to produce finite compressibility factors, $P/\rho kT$, up to $\eta = 1$, i.e., until the whole volume is occupied by the hard molecular cores. However, it is geometrically impossible to exceed the crystal close packing value, $\eta_{cp} = 0.7405$ (for pure hard-sphere components). Furthermore, the MSA can describe only nonordered, amorphous phases, thus it should not be used beyond the

density limit of those phases: random closest packing, η_{rcp} . For pure hard-sphere components, Tobochnik and Chapin²⁰ used Monte Carlo simulations with hyperspherical boundary conditions (which discourage crystal nucleation) to obtain $\eta_{rcp} = 0.69$.

More stringent limits can be obtained from the requirement that the RDFs, $g_{ij}(r)$, be non-negative at all distances r . The MSA does not always satisfy that requirement, as can be seen in Figs. 13, 15, 32, and 33. Two different types of violations can be distinguished according to the part of the RDF that first becomes negative: the contact value, $g_{ij}(\sigma_{ij})$, or the first depression or valley. These two types of nonphysical RDF are discussed below.

The temperature vs packing fraction lines of zero RDF contact values, $g_{ij}(\sigma_{ij}) = 0$, are given in tabular form by Table VII. For a given composition and packing fraction, Table VII gives the temperature below which the lowest RDF contact value becomes negative. For both binary mixtures M1 and M2 at intermediate compositions, of the three different RDFs, $g_{ij}(r)$, it is the one corresponding to correlations between molecules of component 2, $g_{22}(r)$, that first yields a zero contact value. Table VII starts, at each composition, with the first point of the zero contact line that emerges out of the unstable region. Thus for all four pure components, the zero contact point at $\eta = 0.49$ lies inside the unstable region.

At low temperatures, molecules may not have enough kinetic energy to overcome the short-range repulsion. In that case, no hard-core contacts will be possible. Under those conditions, the RDF of a "real" hard-core fluid will remain equal to zero for some small distance beyond the hard-core diameter σ . The MSA, however, neither has the physical constraint $g_{ij}(r) \geq 0$ built-in, nor is capable of producing a sudden change in the slope of the RDFs (except at $r = \sigma$). Therefore, while the MSA correctly reflects that, as distance

TABLE VII. Temperature limit for positive RDF contact values.

| η | x_1 in M1 | | | | | x_1 in M2 ^a | |
|--------|-------------|--------|--------|--------|--------|--------------------------|--------|
| | 1.00 | 0.75 | 0.50 | 0.25 | 0.00 | 1.00 | 0.00 |
| 0.51 | 0.1288 | ... | ... | ... | 0.2668 | 0.1339 | 0.2724 |
| 0.52 | 0.1190 | ... | ... | ... | 0.2476 | 0.1241 | 0.2527 |
| 0.53 | 0.1096 | ... | ... | ... | 0.2289 | 0.1145 | 0.2336 |
| 0.54 | 0.1005 | ... | ... | ... | 0.2113 | 0.1052 | 0.2152 |
| 0.55 | 0.0918 | ... | ... | 0.1949 | 0.1941 | 0.0964 | 0.1974 |
| 0.56 | 0.0836 | ... | ... | 0.1792 | 0.1778 | 0.0879 | 0.1806 |
| 0.57 | 0.0758 | ... | ... | 0.1638 | 0.1622 | 0.0799 | 0.1645 |
| 0.58 | 0.0685 | ... | ... | 0.1494 | 0.1474 | 0.0723 | 0.1493 |
| 0.59 | 0.0616 | ... | ... | 0.1356 | 0.1334 | 0.0652 | 0.1350 |
| 0.60 | 0.0552 | ... | ... | 0.1226 | 0.1203 | 0.0585 | 0.1216 |
| 0.61 | 0.0493 | 0.1173 | 0.1134 | 0.1104 | 0.1080 | 0.0522 | 0.1091 |
| 0.62 | 0.0437 | 0.1064 | 0.1022 | 0.0990 | 0.0966 | 0.0465 | 0.0974 |
| 0.63 | 0.0386 | 0.0961 | 0.0917 | 0.0883 | 0.0860 | 0.0411 | 0.0866 |
| 0.64 | 0.0340 | 0.0864 | 0.0818 | 0.0786 | 0.0761 | 0.0362 | 0.0766 |
| 0.65 | 0.0297 | 0.0773 | 0.0727 | 0.0694 | 0.0671 | 0.0317 | 0.0674 |

^a Mixture M2 at $x_1 = 0.75$ and $x_1 = 0.50$ shows no negative RDF contact values. Mixture M2 at $x_1 = 0.25$ shows zero RDF contact values along an approximately straight line between ($\eta = 0.524, T = 0.2429$) and ($\eta = 0.556, T = 0.1856$).

decreases and contact is approached, the RDF must become zero at some point $r > \sigma$, it cannot stop the RDF from continuing into the negative region.

An increase in packing fraction pushes the molecules closer together, increasing thus the RDF contact values. Such an increase can be eliminated, though, by a decrease in temperature. Table VII shows the mutually compensating changes in packing fraction and temperature needed to maintain a zero RDF contact value.

The deeper the energy well of the potential, ϵ_{ij}^L , the more kinetic energy (temperature) will be needed by the molecules to climb from the preferred minimum potential energy to the $\phi_{ij}(\sigma_{ij}) = 0$ level. This is why the first RDF to produce a zero contact value, $g_{22}(r)$, corresponds to the interaction with the deepest energy well, ϵ_{22}^L . Had the fitting of multi-Yukawa potentials to the Lennard-Jones models been perfect, the four pure components studied here would have been exactly equal except for the difference in the σ_{ij} (or density) and ϵ_{ij}^L (or temperature) scales. (The former is normalized by the use of packing fractions.) Thus taking mixture M2 as an example, since $\epsilon_{22}^L = 2\epsilon_{11}^L$, one would expect the zero contact temperature for pure component 2 to be approximately twice that of pure component 1 at the same packing fraction. This is what is observed in Table VII.

In general, the appearance of negative MSA RDF contact values may restrict severely the range of physical validity of the MSA. In this work, that problem has been minimized by the choice of interaction potentials; particularly, by the avoidance of positive potentials $\phi_{ij}(r)$ beyond the hard cores $r = \sigma_{ij}$.

At high densities, the first depression of the RDF may become negative, see Fig. 15. This phenomenon was already noted for PY hard-sphere RDFs by Ree *et al.*²¹ and even before by Alder (Ref. 31 in Ree's work²¹). As the density increases, the appearance of nonphysical negative intervals in the RDF calculated from the OZ equation can only be avoided through a specially tailored, increasingly longer ranged direct correlation function $c(r)$. This increased range of $c(r)$ has been found experimentally by Tobochnik and Chapin²⁰ and showed necessary by the theoretical analysis

of Song *et al.*²² These latter investigators concluded that as random closest packing is approached, the range of $c(r)$ must diverge to infinity while that of $h(r)$ remains finite. Therefore the usual closures of the OZ equation (such as PY or MSA) fail to provide an exact account of dense amorphous phases. This does not mean, however, that their results are devoid of any physical significance.

A real RDF cannot be negative, but at sufficiently high densities, may tend to zero for some intervals. Then a forbidden spherical shell appears around each molecule surrounding it with a permanent first layer of neighbors.

Tables VIII and IX show the *confinement* packing fractions η_{cf} at several temperatures for mixtures M1 and M2, respectively. These tables also give the confinement radius r_{cf} [$g(r_{cf}) = 0$ at $\eta = \eta_{cf}$] and the energy-derived compressibility factor. At higher densities, $\eta > \eta_{cf}$, the first depression of the RDF becomes strictly negative. For both mixtures M1 and M2, confinement occurs first for the second component (whenever it is present), as $g_{22}(r)$ is the RDF with the lowest first depression. In Tables VIII and IX, the confinement line for each composition starts at the lowest temperature producing a stable MSA solution. In a mixture, the larger molecules (those of component 2 for the mixtures studied here) are more easily confined.

As the packing fraction increases beyond η_{cf} , the confinement volume around each molecule contracts, the forbidden shell grows thicker, and eventually a second forbidden shell appears separating the second layer of neighbors from the rest of the fluid. The appearance of the successive forbidden shells (their number does not need to be limited), will require far smaller increases in density than those suggested by the MSA RDFs. In a real fluid, the onset of each shell will accelerate the appearance of the next. Those small increases in density, however, will be difficult to achieve without an increasingly ordered packaging of molecules.

Generally, the confinement packing fraction η_{cf} diminishes with a decrease in temperature. Such a decrease in T is equivalent to an increase in the effective hard-core diameter of the molecules because it augments the average separation between any two neighbors. The variation of η_{cf} with T is

TABLE VIII. Confinement points; mixture M1.

| kT/ϵ_{11}^L | $x_1 = 1.00$ | | | $x_1 = 0.75$ | | | $x_1 = 0.50$ | | | $x_1 = 0.25$ | | | $x_1 = 0.00$ | | |
|----------------------|--------------|----------|--------|--------------|----------|-------|--------------|----------|-------|--------------|----------|-------|--------------|----------|--------|
| | η_{cf} | r_{cf} | Z^E | η_{cf} | r_{cf} | Z^E | η_{cf} | r_{cf} | Z^E | η_{cf} | r_{cf} | Z^E | η_{cf} | r_{cf} | Z^E |
| 0.110 | 0.5237 | 1.406 | -19.84 | ... | ... | ... | ... | ... | ... | ... | ... | ... | ... | ... | ... |
| 0.125 | 0.5382 | 1.395 | -10.90 | ... | ... | ... | ... | ... | ... | ... | ... | ... | ... | ... | ... |
| 0.150 | 0.5545 | 1.380 | -0.76 | ... | ... | ... | ... | ... | ... | ... | ... | ... | ... | ... | ... |
| 0.220 | 0.5777 | 1.358 | 13.12 | 0.5534 | 1.581 | 0.23 | ... | ... | ... | ... | ... | ... | 0.5289 | 1.629 | -20.95 |
| 0.250 | 0.5829 | 1.352 | 16.08 | 0.5582 | 1.576 | 3.73 | 0.5510 | 1.594 | -2.18 | 0.5452 | 1.608 | -7.72 | 0.5417 | 1.618 | -12.49 |
| 0.330 | 0.5915 | 1.341 | 20.72 | 0.5697 | 1.561 | 10.68 | 0.5669 | 1.576 | 7.37 | 0.5646 | 1.588 | 4.31 | 0.5629 | 1.597 | 1.52 |
| 0.500 | 0.5997 | 1.333 | 24.79 | 0.5810 | 1.543 | 17.18 | 0.5820 | 1.555 | 16.09 | 0.5826 | 1.565 | 15.10 | 0.5830 | 1.574 | 14.23 |
| 1.000 | 0.6066 | 1.320 | 27.88 | 0.5894 | 1.525 | 22.11 | 0.5938 | 1.535 | 22.64 | 0.5970 | 1.543 | 23.16 | 0.5994 | 1.551 | 23.69 |
| 1.750 | 0.6094 | 1.315 | 29.01 | 0.5923 | 1.518 | 23.88 | 0.5978 | 1.527 | 24.86 | 0.6021 | 1.534 | 25.86 | 0.6054 | 1.541 | 26.82 |
| 2.500 | 0.6103 | 1.314 | 29.37 | 0.5933 | 1.515 | 24.53 | 0.5994 | 1.523 | 25.71 | 0.6040 | 1.530 | 26.83 | 0.6076 | 1.537 | 27.92 |
| ∞ (PY) | 0.6125 | 1.310 | 30.21 | 0.5951 | 1.508 | 25.89 | 0.6025 | 1.515 | 27.44 | 0.6082 | 1.522 | 28.88 | 0.6125 | 1.528 | 30.21 |
| ∞ (LL) | 0.6379 | 1.292 | 30.21 | 0.6192 | 1.488 | 25.89 | 0.6271 | 1.495 | 27.44 | 0.6332 | 1.501 | 28.88 | 0.6379 | 1.508 | 30.21 |

TABLE IX. Confinement points; mixture M2.

| kT/ϵ_{11}^{LJ} | $x_1 = 1.00$ | | | $x_1 = 0.75$ | | | $x_1 = 0.50$ | | | $x_1 = 0.25$ | | | $x_1 = 0.00$ | | |
|-------------------------|--------------|----------|--------|--------------|----------|-------|--------------|----------|-------|--------------|----------|--------|--------------|----------|--------|
| | η_{cf} | r_{cf} | Z^E | η_{cf} | r_{cf} | Z^E | η_{cf} | r_{cf} | Z^E | η_{cf} | r_{cf} | Z^E | η_{cf} | r_{cf} | Z^E |
| 0.110 | 0.5197 | 1.405 | -24.67 | ... | ... | ... | ... | ... | ... | ... | ... | ... | ... | ... | ... |
| 0.125 | 0.5344 | 1.395 | -15.47 | ... | ... | ... | ... | ... | ... | ... | ... | ... | ... | ... | ... |
| 0.150 | 0.5512 | 1.381 | -4.73 | ... | ... | ... | ... | ... | ... | ... | ... | ... | ... | ... | ... |
| 0.220 | 0.5753 | 1.359 | 10.34 | ... | ... | ... | ... | ... | ... | 0.5394 | 2.067 | -14.57 | 0.5254 | 2.101 | -23.63 |
| 0.250 | 0.5809 | 1.353 | 13.69 | ... | ... | ... | ... | ... | ... | 0.5507 | 2.053 | -7.34 | 0.5391 | 2.085 | -14.62 |
| 0.330 | 0.5900 | 1.342 | 18.95 | ... | ... | ... | ... | ... | ... | 0.5690 | 2.027 | 4.33 | 0.5615 | 2.057 | 0.26 |
| 0.450 | 0.5970 | 1.333 | 22.75 | ... | ... | ... | 0.5884 | 1.968 | 14.82 | 0.5821 | 2.005 | 12.53 | 0.5781 | 2.032 | 10.97 |
| 0.500 | 0.5987 | 1.331 | 23.66 | ... | ... | ... | 0.5894 | 1.964 | 15.84 | 0.5853 | 1.999 | 14.50 | 0.5824 | 2.025 | 13.63 |
| 0.720 | 0.6034 | 1.325 | 26.02 | 0.5958 | 1.905 | 20.07 | 0.5929 | 1.953 | 18.81 | 0.5935 | 1.983 | 19.41 | 0.5930 | 2.006 | 19.99 |
| 1.000 | 0.6061 | 1.320 | 27.33 | 0.5898 | 1.907 | 19.64 | 0.5951 | 1.945 | 20.65 | 0.5981 | 1.972 | 22.10 | 0.5992 | 1.995 | 23.47 |
| 1.750 | 0.6091 | 1.316 | 28.70 | 0.5860 | 1.905 | 20.23 | 0.5970 | 1.937 | 22.50 | 0.6026 | 1.961 | 24.70 | 0.6053 | 1.982 | 26.71 |
| 2.500 | 0.6101 | 1.314 | 29.16 | 0.5846 | 1.904 | 20.57 | 0.5976 | 1.933 | 23.21 | 0.6043 | 1.956 | 25.66 | 0.6076 | 1.976 | 27.86 |
| ∞ (PY) | 0.6125 | 1.310 | 30.21 | 0.5814 | 1.901 | 21.53 | 0.5988 | 1.925 | 24.81 | 0.6077 | 1.946 | 27.65 | 0.6125 | 1.964 | 30.21 |
| ∞ (LL) | 0.6379 | 1.292 | 30.21 | 0.6042 | 1.877 | 21.53 | 0.6230 | 1.900 | 24.81 | 0.6326 | 1.920 | 27.65 | 0.6379 | 1.938 | 30.21 |

much more pronounced at very low temperatures, where a small decrease ΔT in T results in a large increase in $(1/T)$ and therefore a large decrease in energy $\phi(r)$ [to keep $\phi(r)/kT$ constant]; this decrease in energy leads, in turn, to a much larger increment of the molecular separation distance r if the energy level (or the temperature) is low.

Although the previous reasoning explains the observations for pure components, the behavior of mixtures (the intermediate compositions) is more complicated. In this case, the η_{cf} values given in the tables correspond to the confinement of the larger molecules of component 2. Component 1 is still free to move around and between the molecules of 2. A certain decrease in temperature (and energy) will affect the different separation distances r_{ij} according to the corresponding interactions $\phi_{ij}(r)$: neglecting the relatively minor role played by the diameter σ_{ij} , for LJ-like potentials one can state that the smaller the energy well depth, ϵ_{ij}^{LJ} , the larger the change in r_{ij} will be. For mixtures M1 and M2, a decrease in temperature produces larger increases of both r_{11} and r_{12} (especially for M2) than of r_{22} . Therefore, as the temperature diminishes, the general trend of increasing effective hard-core diameters (which lowers η_{cf}) is combined with a faster increase of the those effective diameters (r_{11} and r_{12}) that tend to push the molecules of 2 farther apart from each other, making their confinement more difficult (which tends to increase η_{cf}). The second effect grows more important as the mole fraction of the "dispersant" component 1 increases. Under very favorable conditions, such as for mixture M2 at $x_1 = 0.75$, this dispersing effect may reverse the general trend, resulting in a confinement packing fraction η_{cf} that increases with lower temperatures.

Again, the scaling relations among the four pure components are clear. For example, in mixture M2 the confinement packing fraction of pure component 1 at $T = 0.50$, $\eta_{cf} = 0.5987$, is approximately equal to that of pure component 2 at $T = 1.00$ (equal scaled temperature kT/ϵ_{ii}^{LJ}), $\eta_{cf} = 0.5992$.

The confinement lines given in Tables VIII and IX have been determined from the MSA RDFs. These RDFs are

known to be of relatively poor accuracy. It is possible to estimate the effect of that inaccuracy in the confinement measurements by examining the infinite temperature limit. In that limit, the MSA (or Percus-Yevick) RDF can be compared to the more accurate Lee-Levesque²³ (or Verlet-Weis²⁴ for pure components) RDF for hard spheres. Tables VIII and IX give both the PY and LL confinement packing fractions for the infinite temperature limit. The LL RDFs yield slightly higher values of η_{cf} , the difference over the PY values being small and almost constant, ~ 0.0250 .

Confinement does not imply molecular ordering (although it is certainly exhibited by crystals) but it does involve some sort of semirigid packing. Indeed, for pure components, one can compare the infinite temperature values of η_{cf} given in Tables VIII and IX, 0.6125 (PY) and 0.6379 (LL), to the experimentally determined random packing values of equal-sized steel spheres. For that system, Scott²⁵ found a range of random packing densities between $\eta = 0.601$, loose, and $\eta = 0.637$, dense random packing (these two values were found reproducible to within 0.2%).

Although the fluids studied here have hard, impenetrable cores, the concept of confinement is not exclusive to them. Soft core molecules are certain to exhibit forbidden shells or empty gaps (confinement) in their RDFs at appropriate densities and temperatures. The main difference between the two types of fluids will be their response to increasing temperatures. At a given constant density, a sufficient increase in temperature will reduce the effective molecular diameter of a soft core fluid (and therefore its effective packing fraction) to the point where its molecules will be able to escape confinement. In practical terms, however, the required temperature, at constant density, may generate a pressure not easy to contain.

The physical implications of confinement are more easily understood in the case of pure components. Therefore, initially the discussion will be limited to pure fluids.

The onset of confinement in the RDF of a real fluid has drastic consequences for the mobility of the confined molecules: no such a molecule is free to move within the system.

For most real substances, as the density increases the stable fluid phase undergoes a transition into a stable crystalline solid phase. The MSA, not being able to account for ordered molecular arrangements, cannot provide the liquid with that early exit to the stable crystal. As a result, the MSA presents a continuous variation in density, with the fluid phase being extended into a metastable region.

Although it is established that only invoking dynamic properties (particularly mode-mode coupling, see, Götze and Sjögren²⁶) can correctly describe metastable fluid or glassy state,²⁷ in this paper we assume that static approach may have limited validity at the onset of the metastable region.

From a molecular viewpoint, the transition from fluid to glass is characterized by a halt to self-diffusion and by "structural arrest," see Pusey and van Megen.²⁸ Confinement obviously makes self-diffusion impossible. Structural arrest consists in the appearance of permanent, nonfluctuating features in the RDF, which is normally obtained as the time average of continuously fluctuating fluidlike configurations. The zero value of the RDF at confinement (being the average of zero values) is one such permanent feature. [The occurrence of both negligible self-diffusion and structural arrest in a fluid will generally precede the appearance of confinement in its exact RDF. In this MSA model, we assume that occurrence to be simultaneous with confinement in the MSA RDF (which will be reached earlier than in the exact RDF).]

From a thermodynamic viewpoint, the glass transition is second order (Rowlinson²⁹). There are no sudden volumetric or energetic changes. But, at constant pressure, the rate of change of volume and enthalpy with temperature, i.e., $(\partial V/\partial T)_p$ and $c_p = (\partial H/\partial T)_p$, suddenly drops as the glassy state is entered. At constant density, that drop appears in $[\partial P/\partial(kT)]_\rho$ and $(c_v/k) = [\partial U/\partial(kT)]_\rho = \frac{3}{2} + [(\partial U^c/\partial(kT))_\rho]$. Such a drop is not observed in the MSA thermodynamic properties.

Figures 32 and 33 present the variation with temperature of the MSA RDF of pure component 1 in mixture M1 at $\eta = 0.5829$. Qualitatively, this variation is entirely similar to that observed by Wendt and Abraham³⁰ in their Monte Carlo study of the glass transition region for a Lennard-Jones fluid. In particular, the MSA RDFs indicate the appearance of the split second peak (due to short-range molecular ordering) typical of dense amorphous phases. The heat capacity c_v of a real fluid will drop suddenly as that fluid crosses the confinement line (at constant density) to become a glass. We can mimic this behavior if $g(r)$ is kept equal to zero at regions where MSA gives negative values of $g(r)$ beyond confinement line. This procedure gives discontinuous configurational energy as shown in Fig. 34. Based on the MSA RDFs, we formulate the following MSA model of glass transition: the MSA is assumed to give a reasonable representation of real substance behavior up to the confinement point η_{cr} ; beyond this point, a physical continuation is defined in which the MSA $g(r)$ is restricted to non-negative values.

For pure hard-sphere components, metastable phases can be found in the range of densities from freezing

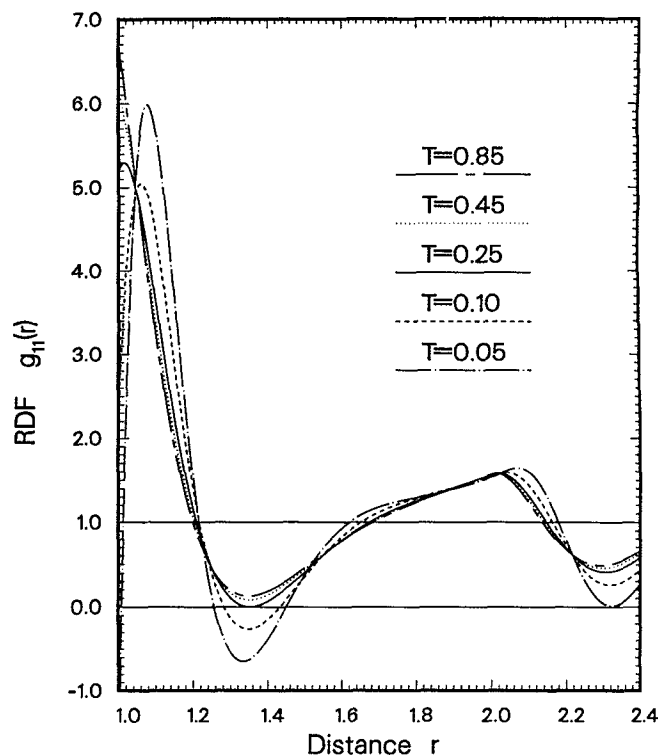


FIG. 32. Variation of the radial distribution function of M1, $x_1 = 1.0$, with temperature at $\eta = 0.5829$. At this packing fraction, confinement is reached for $T = 0.25$.

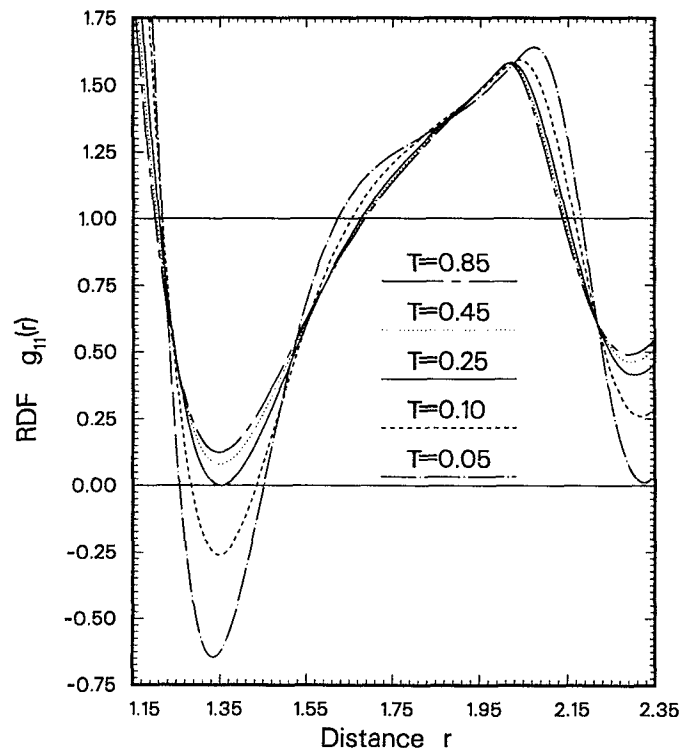


FIG. 33. Medium range detail of the RDF shown in Fig. 32.

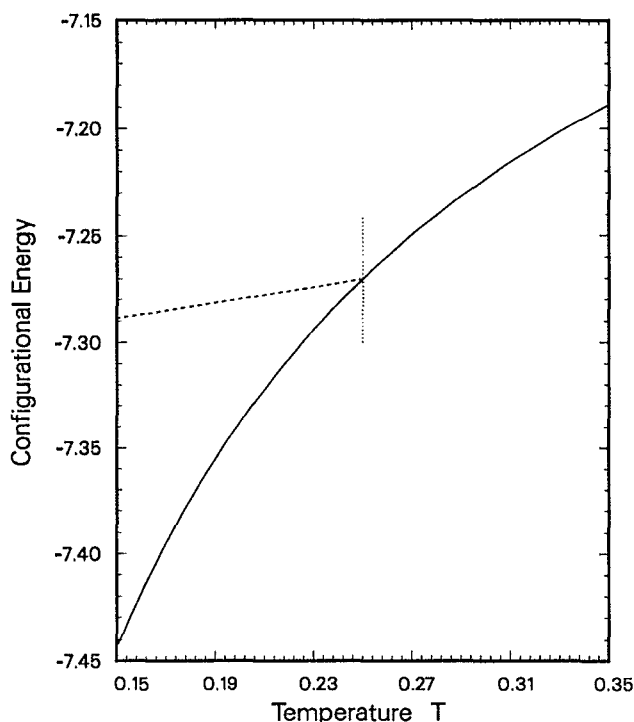


FIG. 34. Observed variation (continuous curve) of MSA configurational energy as the confinement line (vertical dots) is crossed. The dashed line represents the expected variation for physical substances, i.e., for configurations producing non-negative radial distribution functions.

$\eta_{tz} = 0.494$ (Hoover and Ree³¹) to random closest packing, $\eta_{rcp} = 0.69$ (Tobochnik and Chapin²⁰). At some density η_g , these metastable phases will be separated into fluid and amorphous solid by the glass transition. Woodcock³² used molecular dynamics (MD) to study the glass transition in the hard-sphere fluid. His volumetric data suggest a sudden change in the slope of pressure with increasing density at $\eta_g = 0.574$. This technique, however, due to the extremely fast rates of compression (or cooling) required in MD, significantly underestimates the transition density³³ (or overestimates the transition temperature). On the other hand, using Doolittle's expression³⁴ to extrapolate Woodcock's self-diffusion coefficients down to zero, the glass transition is placed at $\eta_g = 0.637$. More recent MD simulations of fluids with a purely repulsive LJ potential³⁵ yield self-diffusion coefficients in general agreement with those of Woodcock.

Some experimental measurements are available for real systems composed of spherical particles of approximately equal size with steep, repulsive interactions. Pusey and van Megen²⁸ investigated colloidal suspensions, in which they observed structural arrest at $\eta_g = 0.59$ and 0.56 for two different systems. Chen and Huang,³⁶ in their study of microemulsions, used the initial decay rate of the density correlation function to detect the onset of structural arrest at $\eta_g = 0.62$ (at a temperature of 23.5°C).

In general, the density (and pressure) at the glass transition will depend on temperature. Fox and Andersen³⁷ used MD to study the relation between temperature and pressure along the glass transition line for a pure fluid with a truncat-

ed and shifted LJ potential [$\phi(r) = \phi^{LJ}(r) + c$ for $r < 1.5\sigma$ and $\phi(r) = 0$ at longer distances, c ensures the continuity of the potential at the truncation distance]. They identified the location of the glass transition with the meeting point of the essentially linear variations of density and enthalpy in the metastable fluid and glass regions when cooling at constant pressure. The transition pressure P_g was found to be a linear function of the temperature T_g . Here we give that function and compare it with the similar relation for the confinement line of pure component 1 of mixture M2 (the one most closely resembling a LJ fluid with $\sigma = 1$, $\epsilon^{LJ} = 1$),

$$P_g \sigma^3 / \epsilon^{LJ} = 37.74 (kT_g / \epsilon^{LJ}) - 10.46 \quad (\text{Ref. 37}), \quad (72)$$

$$P_g \sigma^3 / \epsilon^{LJ} = 36.43 (kT_g / \epsilon^{LJ}) - 5.00 \quad (\text{this work}). \quad (73)$$

[Our results were obtained through a least squares fit ($R^2 = 0.9997$) of the (M2, $i = 1$) confinement data in the temperature range from 0.22 to 1.75.] The difference in the slope arises because our hard-core potential is slightly less sensitive to temperature changes than the soft-core interaction used by Fox and Andersen. The intercept obtained by these authors reflects the fact that their technique underestimates the real glass transition density and pressure for a given temperature.²⁹ As they point out, a Doolittle extrapolation of their self-diffusion data would predict a glass transition at a significantly higher pressure than that given by Eq. (72).

To conclude, the overall limits beyond which the MSA gives nonphysical results are summarized here. Figures 35 to 37 present those limits for mixtures M1 and M2. At each composition, two parts can be distinguished in the limit lines. The first part signals the limit of thermodynamic stability. The second part is the limit of positive radial distribution functions.

Below the stability limit (at lower temperature), the range of the molecular correlations becomes infinite and no solution of the OZ equation (no proper MSA solution) can be found. The stability limit can be subdivided into two sections. The first, bell-shaped section corresponds to vapor-liquid instability. For a given density (which determines the average molecular separation), only temperatures above this section of the instability limit provide the molecules with sufficient kinetic energy to avoid collapsing under their mutual attractions (which would make impossible for them to fill the specified volume). The second section—the raising slope after the bell—corresponds to liquid-liquid instability. This section appears whenever the unlike-particle attractions are weaker than the like-particle ones. In that case, only temperatures above the limit provide sufficient kinetic energy for the molecules to overcome that imbalance and avoid segregation into phases of different composition.

The positive RDF limit can also be subdivided into two sections. The first of these sections corresponds to zero RDF contact values. Its slope is always negative in the temperature vs packing fraction diagram. Its position is very much dependent on the contact value of the interaction potential, $\phi(\sigma)$ (where σ is the hard-core diameter, always needed in the MSA), and the difference between that contact value and the minimum value of the potential. The second section of the positive RDF limit corresponds to zero minima of the

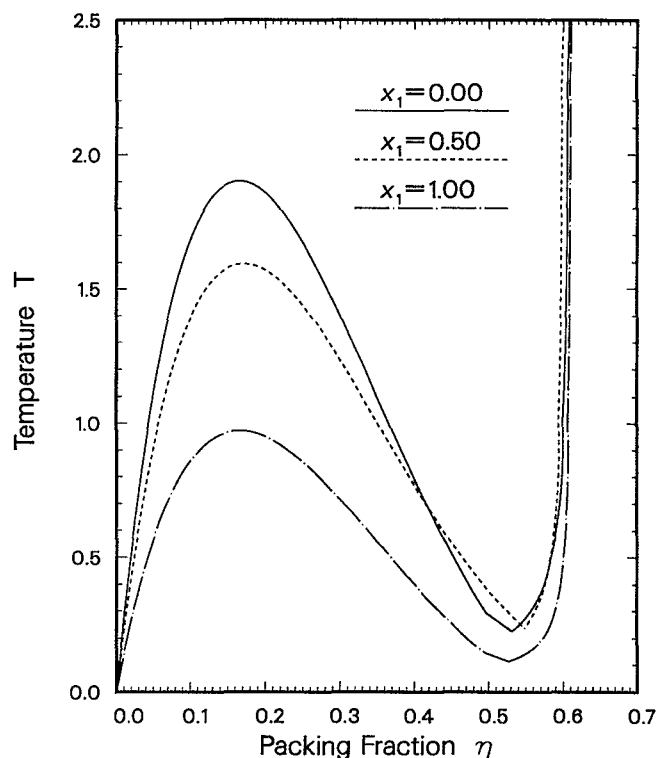


FIG. 35. Limits of the fluid range (above and to the left of the curves) for mixture M1 at the compositions indicated. The bell-shaped vapor-liquid instability limit is followed (except for $x_1 = 0.50$) by a short, straight interval corresponding to zero RDF contact values, and later by the confinement or fluid-glass transition line.

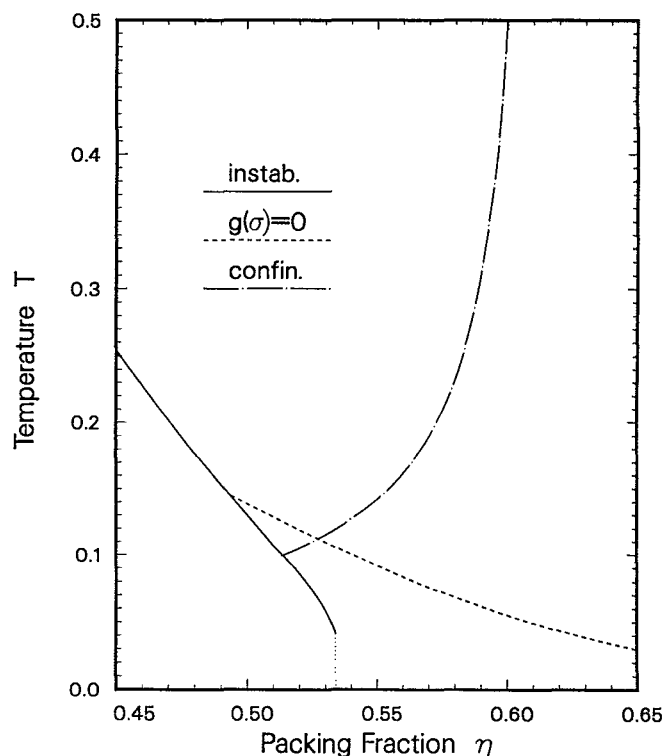


FIG. 36. High-density fluid limits for the first component ($x_1 = 1.0$) of mixture M1. This plot shows the line of vapor-liquid instability (which at this scale is indistinguishable from the no-solution line) ending at the forced stability packing (vertical dots), the zero RDF contact value line, and the confinement line.

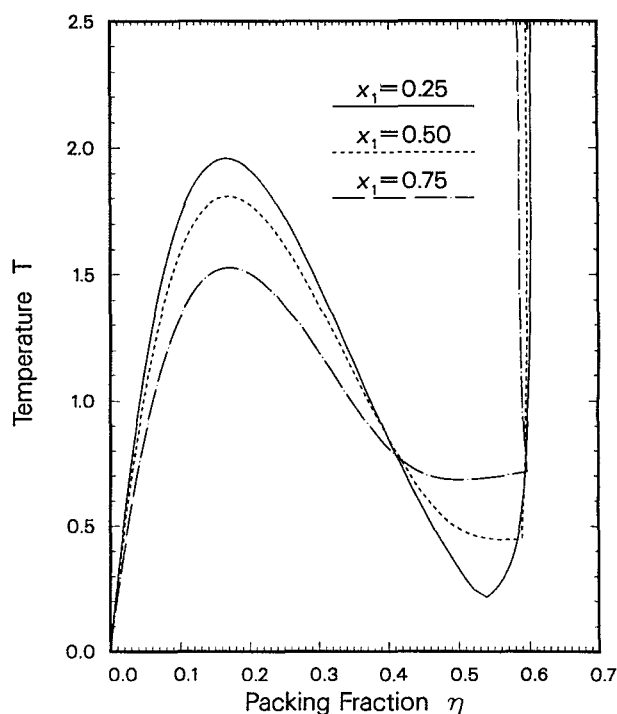


FIG. 37. Limits of the fluid range (above and to the left of the curves) for mixture M2 at the compositions indicated. The bell-shaped vapor-liquid instability limit joins (except for $x_1 = 0.25$) the liquid-liquid instability limit before reaching the confinement or fluid-glass transition line.

first depression. For a given temperature (which determines the effective hard-core diameters), densities beyond this limit no longer correspond to fluids but to glasses (or gels) exhibiting molecular confinement. The MSA cannot describe those glassy states correctly.

Finally, we would like to mention a significant work of Bernu *et al.*³⁸ These authors studied a mixture described by repulsive soft sphere potentials. They compared the MD results with the results of thermodynamically self-consistent equation of Rogers and Young (RY).³⁹ In the supercooled region the MD pressures were significantly higher than pressures from the RY equation. Although the MD branch was not unique, MD-generated “glassy” states fell on the same curve independently of an initial preparation and nearly independently of a concentration.

VII. CONCLUSIONS

This work has presented a complete, efficient numerical algorithm for solving the Blum and Høye³ (BH) mean spherical approximation (MSA) equations for multicomponent mixtures interacting through multi-Yukawa potentials. Most of the calculations involved are analytic and explicit. The only numerical part of the algorithm is the solution of a system of nonlinear equations. By starting from a physically based initial estimate, however, the algorithm solves this nonlinear system in just a few iterations (usually two or three). Moreover, for all cases studied in the fluid region, the algorithm is found to yield the unique, physical

solution whenever it exists. In regions of thermodynamic instability, the algorithm may declare the absence of solutions or, less often, may yield an unstable solution—both cases being an indication that no homogeneous single phase may exist for the specified conditions. For the latter case, a simple procedure is provided to detect the instability of such a solution.

The Yukawa-MSA algorithm developed in this work puts the MSA solution of realistic fluid mixtures at almost the same level of practical convenience as that of hard-sphere systems. It makes possible an indirect, quasianalytic solution for *any* isotropic potential in the MSA: the multi-Yukawa potential, through an indefinite number of Yukawa tails, can represent any interaction with arbitrary accuracy. The algorithm provides not only the solution of the BH nonlinear equations, but it also yields all thermodynamic properties (through analytic expressions) and the radial distribution functions, RDF, of the fluid mixture (through the appropriate modification of Perram's algorithm¹⁰ for hard spheres).

The qualitative capabilities of the MSA have been investigated by using the Yukawa-MSA algorithm to study two specific binary multi-Yukawa mixtures. These mixtures were characterized by realistic interaction potentials that included significant repulsion intervals. [However, positive interactions (which the MSA can handle only to a limited extent) were avoided completely; instead, hard cores were used for the close range ($r < \sigma$) repulsions.]

This investigation has found the MSA able to make a clear and immediate distinction between ideal and nonideal mixtures. By determining the region in which no solutions exist for the BH equations, or even better (and faster), by finding the spinodal or thermodynamic instability lines, the Yukawa-MSA algorithm reveals the shape and approximate location of the phase equilibrium envelope. The shape of this envelope shows whether a given mixture exhibits liquid-liquid separation, in addition to the always present vapor-liquid equilibrium.

Particular attention has been given to the physical significance of the range of the correlation functions, given by the algorithm as $R^{-1}(0)$ and $\tilde{h}_{ij}(0)$ (Sec. V). It has been shown that, for any stable solution, a simple temperature derivative of these quantities can be used to estimate the distance (in temperature) from that solution to the unstable region, and to predict the type of phase separation corresponding to that unstable region.

Last, this work has determined the high-density limit beyond which the first depression of the RDF becomes negative. That limit signals the end of the fluid range; beyond, only amorphous (glassy) or ordered (crystalline) solids can be found. The limit itself has been interpreted as the transition from metastable fluid to metastable glass.

The computational convenience with which the quasianalytic Yukawa-MSA algorithm can treat realistic dense fluid mixtures makes this method a most appropriate tool for the use of statistical mechanics in practical, engineering applications.

In addition, the existence of the Yukawa-MSA algorithm makes possible the utilization of multi-Yukawa mix-

tures as a reference fluid for perturbation theories. Such a reference fluid is much more realistic than the usual hard-sphere fluid; yet, its solution is almost as simple to obtain. By properly adjusting the multi-Yukawa potential, the difference between the reference interaction and the potential of interest can be minimized, especially in the attractive region (not so much in the repulsive region, where, because of the MSA, the reference potential must present, at some point, a hard core). The soft, positive repulsion exhibited by real fluids can be accounted for by a proper choice of hard-core diameter and a slightly modified negative repulsion. Thus the perturbation will involve only a relatively minor difference (much smaller than that present when hard spheres are used) in the repulsive part of the interaction. Because the accuracy of perturbation methods is strongly affected by the magnitude of the difference between actual and reference potentials, the use of multi-Yukawa reference fluids seems highly advantageous.

Finally, it is worth noting that the capabilities of the Yukawa-MSA algorithm can be further extended. First, a cluster expansion method, such as EXP,⁴⁰ can be used to improve the relatively poor MSA radial distribution functions. Second, a generalized mean spherical approximation (GMSA) type of approach may further increase the accuracy of the MSA and, more important, enhance significantly its ability to handle positive repulsions. Last, the Yukawa-MSA algorithm can be adapted, through the site-site formalism,⁴¹ to nonspherical, polyatomic molecules.

A subsequent paper will analyze the quantitative accuracy of the MSA by comparing its results to those obtained from Monte Carlo simulations for the same mixtures studied here.

ACKNOWLEDGMENTS

We thank Dr. H. C. Anderson, Dr. B. E. Gammon, Dr. J. Gryko, Dr. J. S. Rowlinson, and Dr. W. A. Steele for many useful discussions. This work was supported by the GRI Grant No. 5086-260-1240. C. Jedrzejek acknowledges a travel grant through the Polish Ministry of Education and Science Project No. CPBP 01.03.3.4.

APPENDIX A

Expressions for the coefficients appearing in Eqs. (13) and (14) are given here. Note that the quantities $\{\rho_i\}$, $\{\sigma_{ij}\}$, $\{K_{vij}\}$, and z_v constitute the data of the problem. The symbol $\{\delta_{ij}\}$ represents Kronecker's delta. The following parameters correspond to the hard-sphere case:

$$A_j^0 = \frac{2\pi}{(1 - \xi_3)^2} (1 - \xi_3 + 3\sigma_j\xi_2), \quad (\text{A1})$$

$$B_j^0 = \frac{2\pi}{(1 - \xi_3)^2} (-\frac{3}{2}\sigma_j^2\xi_2), \quad (\text{A2})$$

$$b_{ij}^0 = \frac{2\pi}{(1 - \xi_3)^2} [\frac{3}{2}\sigma_i\sigma_j\xi_2 + \sigma_{ij}(1 - \xi_3)], \quad (\text{A3})$$

where

$$\xi_\alpha = \frac{\pi}{6} \sum_i \rho_i \sigma_i^\alpha. \quad (\text{A4})$$

Obviously, ξ_3 is equal to the packing fraction η . The functions

$$\vartheta_1(x) = 1 - x - e^{-x}, \quad (\text{A5})$$

$$\vartheta_2(x) = 1 - x + \frac{1}{2}x^2 - e^{-x}, \quad (\text{A6})$$

are also needed in the determination of the following coefficients:

$$M_{\tau m}^{(a)} = 1 + z_\tau \sigma_m, \quad (\text{A7})$$

$$L_{\tau m j}^{(a)} = 1 + z_\tau \sigma_{mj} + \frac{1}{2} z_\tau^2 \sigma_m \sigma_j, \quad (\text{A8})$$

$$H_{v l j}^{(a)} = z_v b_{l j}^0 \vartheta_1(z_v \sigma_l) + A_j^0 \vartheta_2(z_v \sigma_l), \quad (\text{A9})$$

$$G_{v l j}^{(a)} = z_v A_l^0 \vartheta_1(z_v \sigma_l) - \frac{4}{\sigma_j^2} B_j^0 \vartheta_2(z_v \sigma_l), \quad (\text{A10})$$

$$F_{\tau m l j}^{(a)} = L_{\tau m j}^{(a)} G_{v l j}^{(a)} - z_\tau M_{\tau m}^{(a)} H_{v l j}^{(a)}, \quad (\text{A11})$$

$$E_{\tau m l j}^{(a)} = (1 + z_\tau \lambda_{jm}) G_{v l j}^{(a)} - z_\tau H_{v l j}^{(a)}, \quad (\text{A12})$$

$$D_{\tau m j l}^{(a)} = \frac{1}{(z_v z_\tau)^3} [\rho_m F_{\tau m j l}^{(a)} + \delta_{mj} (z_v z_\tau)^2 \times \left(1 - \frac{z_\tau}{z_v + z_\tau} e^{-z_v \sigma_j} \right)], \quad (\text{A13})$$

$$C_{\tau m j l}^{(a)} = \frac{1}{(z_v z_\tau)^3} \left\{ \rho_m (E_{\tau m j l}^{(a)} - F_{\tau m j l}^{(a)} e^{-z_v \sigma_m}) + \delta_{mj} \frac{(z_v z_\tau)^2}{z_v + z_\tau} [z_v (1 - e^{-z_v \sigma_j}) - z_\tau e^{-z_v \sigma_j} (1 - e^{-z_v \sigma_j})] \right\}, \quad (\text{A14})$$

$$A_{v i j}^{(4)} = 2\pi K_{v i j}, \quad (\text{A15})$$

$$A_{v l j}^{(3)} = \frac{1}{z_v^3} \rho_l H_{v l j}^{(a)} - \delta_{l j}, \quad (\text{A16})$$

$$A_{\tau m j l}^{(2)} = \rho_l D_{\tau m j l}^{(a)}, \quad (\text{A17})$$

$$A_{\tau v k m j l}^{(1)} = \frac{2\pi}{z_\tau^2} \rho_k \rho_l C_{\tau v m j l}^{(a)}, \quad (\text{A18})$$

$$H_{v i j}^{(b)} = b_{i j}^0 + \frac{1}{z_v} A_j^0, \quad (\text{A19})$$

$$G_{v i j}^{(b)} = A_i^0 - \frac{1}{z_v} \frac{4}{\sigma_j^2} B_j^0, \quad (\text{A20})$$

$$F_{\tau m i j}^{(b)} = L_{\tau m j}^{(a)} G_{v i j}^{(b)} - z_\tau M_{\tau m}^{(a)} H_{v i j}^{(b)}, \quad (\text{A21})$$

$$E_{\tau m i j}^{(b)} = (1 + z_\tau \lambda_{jm}) G_{v i j}^{(b)} - z_\tau H_{v i j}^{(b)}, \quad (\text{A22})$$

$$D_{\tau m i j}^{(b)} = \frac{1}{2\pi} \left[\frac{1}{z_\tau^3} \rho_m F_{\tau m i j}^{(b)} + \delta_{im} \frac{z_v}{z_v + z_\tau} \right], \quad (\text{A23})$$

$$C_{\tau v k i j}^{(b)} = \frac{1}{2\pi} \frac{1}{z_\tau^3} [\rho_k (E_{\tau v k i j}^{(b)} - F_{\tau v k i j}^{(b)} e^{-z_v \sigma_k}) - \delta_{ik} \frac{z_v z_\tau^3}{z_v + z_\tau} e^{-z_v \sigma_i}], \quad (\text{A24})$$

$$B_{v i j}^{(6)} = \frac{1}{2\pi} H_{v i j}^{(b)}, \quad (\text{A25})$$

$$B_{v l j}^{(5)} = \frac{1}{z_v^3} \rho_l H_{v l j}^{(a)} - \delta_{l j}, \quad (\text{A26})$$

$$B_{\tau m i j}^{(4)} = D_{\tau m i j}^{(b)}, \quad (\text{A27})$$

$$B_{\tau v m l j}^{(3)} = \rho_l D_{\tau v m l j}^{(a)}, \quad (\text{A28})$$

$$B_{\tau v m k i j}^{(2)} = \frac{2\pi}{z_\tau^2} \rho_m C_{\tau v k i j}^{(b)}, \quad (\text{A29})$$

$$B_{\tau v k m l j}^{(1)} = \frac{2\pi}{z_\tau^2} \rho_k \rho_l C_{\tau v m l j}^{(a)}. \quad (\text{A30})$$

APPENDIX B

This Appendix evaluates the MSA energy-derived second virial coefficients B_{ij} for the binary mixtures studied in this work. Both the truncated Lennard-Jones models and the fitted multi-Yukawa potentials are considered. For hard-core potentials such as these, the second virial coefficients are given by

$$B_{ij} = \frac{2\pi}{3} \sigma_{ij}^3 - \frac{2\pi}{3kT} \rho \int_{\sigma_{ij}}^{\infty} \phi'_{ij}(r) g_{ij}(r) r^3 dr, \quad (\text{B1})$$

where the RDF $g_{ij}(r)$ must be evaluated at $\rho = 0$. In the MSA, the zero density RDF is approximated by

$$g_{ij}(r) = 1 - \frac{\phi_{ij}(r)}{kT} \quad (\rho = 0), \quad (\text{B2})$$

which must be taken to Eq. (B1). Since Eq. (B2) does not give the *real* zero density RDF, the MSA second virial coefficients are different from the *real* ones. Furthermore, since one normally would use the more accurate energy-derived pressures, an additional term is needed to account for the contribution from the RDF contact values, see Eq. (39). Evaluating those contact values (MSA and Percus-Yevick) at zero density, the following expression is obtained for the MSA energy-derived second virial coefficients:

$$B_{ij} = \frac{2\pi}{3} \sigma_{ij}^3 + \frac{\pi}{3} \sigma_{ij}^3 \{ [1 - \phi_{ij}(\sigma_{ij})/kT]^2 - 1 \} - \frac{2\pi}{3kT} \rho \int_{\sigma_{ij}}^{\infty} \phi'_{ij}(r) [1 - \phi_{ij}(r)/kT] r^3 dr. \quad (\text{B3})$$

For the Lennard-Jones model potentials $\phi_{ij}(\sigma_{ij})$ is zero, and the second term on the right-hand side is not needed. However, this is not necessarily so for the fitted multi-Yukawa interactions. [Actually, none of the multi-Yukawa $\phi_{ij}(\sigma_{ij})$ in this work are exactly zero, although all of them are small enough to give an almost negligible contribution to the B_{ij} 's.] Performing the operations indicated in Eq. (B3) one obtains the following MSA energy-derived second virial coefficients for both the truncated Lennard-Jones model (LJ) and for the fitted multi-Yukawa (ω Y) potentials:

$$B_{ij} = \frac{2\pi}{3} \sigma_{ij}^3 \left[1 - \frac{\alpha_{ij}}{kT} - \frac{\beta_{ij}}{(kT)^2} \right], \quad (\text{B4})$$

where, for the truncated Lennard-Jones potential,

$$\alpha_{ij}^{\text{LJ}} = \frac{8}{3} \epsilon_{ij}^{\text{LJ}}, \quad (\text{B5})$$

$$\beta_{ij}^{\text{LJ}} = \frac{64}{105} (\epsilon_{ij}^{\text{LJ}})^2, \quad (\text{B6})$$

and, for the multi-Yukawa potential,

$$\alpha_{ij}^{\omega Y} = 3 \sum_{\nu} \epsilon_{\nu ij} \frac{1 + z_{\nu} \sigma_{ij}}{(z_{\nu} \sigma_{ij})^2}, \quad (\text{B7})$$

$$\beta_{ij}^{\omega Y} = \sum_{\nu\tau} \epsilon_{\nu ij} \epsilon_{\tau ij} \frac{(z_{\nu} + 2z_{\tau})\sigma_{ij} + (1/2)(z_{\tau}^2 - z_{\nu}^2)\sigma_{ij}^2}{(z_{\nu} + z_{\tau})^2 \sigma_{ij}^2}, \quad (\text{B8})$$

where ν and τ vary between 1 and ω , the total number of Yukawa tails.

Table X compares the MSA energy-derived second virial coefficients for the truncated Lennard-Jones and the multi-Yukawa interactions. In all cases, $\alpha_{ij}^{\omega Y} < \alpha_{ij}^{\text{LJ}}$, the reason being that the long-range exponential Yukawa tail vanishes faster with distance than the Lennard-Jones r^{-6} term. The agreement between model and fitted potentials is better for mixture M2, despite the larger size difference between its components, thanks to the additional Yukawa tail. The better agreement is most clearly seen by comparing the first components (B_{11}) of both mixtures. [The intermolecular attractions in comp. 1 of M1, (M1, $i = 1$), are weaker than those in (M2, $i = 1$), which produces a corresponding difference in their MSA compressibility-determined critical points (the peaks of the instability curves in Figs. 3 and 4), whose $kT_c/\epsilon_{11}^{\text{LJ}}$ are 0.97 and 1.01, respectively.]

In retrospect, it is clear that whenever a good quantitative agreement is needed, the fitted potential should have exactly the same contact value $\phi_{ij}(\sigma_{ij})$ as the model one, and the second virial coefficient should be included, with a heavy weight, in the fitting procedure. For the purposes of this study, however, the good agreement evidenced by Table X is more than sufficient to ensure that the multi-Yukawa potentials used were qualitatively realistic.

APPENDIX C

This Appendix explains the detailed calculation of the $\{G'_{vij}\}$ quantities defined by Eq. (38). Taking the appropriate derivatives in Eq. (33) of Blum and Høye's paper³ and rearranging, one arrives at the following linear system:

$$\sum_l S_{vij} G'_{vil} = T_{vij}. \quad (\text{C1})$$

Solving it the desired $\{G'_{vij}\}$ are obtained. What follows is the determination of the coefficients appearing in this equation:

$$S_{vij} = 2\pi(\delta_{ij} - \rho_l \hat{Q}_{vij}), \quad (\text{C2})$$

where \hat{Q}_{vij} is given by Eq. (18).

On the other hand,

$$T_{vij} = 2\pi \sum_l \rho_l G_{vil} \hat{Q}'_{ij} - R_{vij}, \quad (\text{C3})$$

where

$$R_{vij} = \frac{2 + z_{\nu} \sigma_{ij}}{z_{\nu}^2} a_{ij} + \frac{1 + z_{\nu} \sigma_{ij}}{z_{\nu}} b_{ij} - \sum_{\tau} \frac{z_{\nu} + z_{\tau} (z_{\nu} + z_{\tau}) \sigma_{ij}}{(z_{\nu} + z_{\tau})^2} C_{\tau ij}, \quad (\text{C4})$$

and

$$\hat{Q}'_{vij} = - \int_{\lambda_{ji}}^{\infty} t e^{-z_{\nu}(t - \lambda_{ji})} Q_{ij}(t) dt. \quad (\text{C5})$$

In order to calculate this quantity the following recursive functions are needed:

$$\psi_0(x, y) = -1, \quad (\text{C6})$$

$$\psi_n(x, y) = n\psi_{n-1}(x, y) - (xy)^n. \quad (\text{C7})$$

Now one can write

$$\begin{aligned} \hat{Q}'_{ij} = & \frac{1}{2z_{\nu}^4} a_{ij} [\psi_3(z_{\nu}, \lambda_{ji}) - \psi_3(z_{\nu}, \sigma_{ij}) e^{-z_{\nu} \sigma_{ij}}] - \frac{1}{z_{\nu}^3} (a_{ij} \sigma_{ij} - b_{ij}) [\psi_2(z_{\nu}, \lambda_{ji}) - \psi_2(z_{\nu}, \sigma_{ij}) e^{-z_{\nu} \sigma_{ij}}] \\ & + \frac{1}{z_{\nu}^2} \left(\frac{1}{2} a_{ij} \sigma_{ij}^2 - b_{ij} \sigma_{ij} - \sum_{\tau} \frac{1}{z_{\tau}} C_{\tau ij} \right) [\psi_1(z_{\nu}, \lambda_{ji}) - \psi_1(z_{\nu}, \sigma_{ij}) e^{-z_{\nu} \sigma_{ij}}] \\ & - \sum_{\tau} \frac{1}{z_{\tau} (z_{\nu} + z_{\tau})^2} C_{\tau ij} \psi_1(z_{\nu} + z_{\tau}, \sigma_{ij}) e^{-z_{\nu} \sigma_{ij}} + \sum_{\tau} \frac{1}{z_{\tau} (z_{\nu} + z_{\tau})^2} f_{\tau ij} \psi_1(z_{\nu} + z_{\tau}, \lambda_{ji}). \end{aligned} \quad (\text{C8})$$

APPENDIX D

The following is a stepwise algorithm for the calculation of the radial distribution functions. Let us define

$$\theta_{ij}(r) = r g_{ij}(r), \quad (\text{D1})$$

and

$$\check{\theta}_{ij}(k) = \theta_{ij}(\sigma_{ij} + ks), \quad (\text{D2})$$

$$\check{Q}_{ij}(k) = Q_{ij}(\lambda_{ji} + ks), \quad (\text{D3})$$

TABLE X. MSA energy-derived second virial coefficients.

| | | B_{11} | | B_{12} | | B_{22} | |
|---------|-----------|---------------|--------------|---------------|--------------|---------------|--------------|
| Mixture | Potential | α_{11} | β_{11} | α_{12} | β_{12} | α_{22} | β_{22} |
| M1 | LJ | 2.6667 | 0.6095 | 3.6941 | 1.1697 | 5.1173 | 2.2446 |
| | Y3 | 2.5112 | 0.6091 | 3.5374 | 1.1696 | 4.9226 | 2.2460 |
| M2 | LJ | 2.6667 | 0.6095 | 3.1490 | 0.8500 | 5.3333 | 2.4381 |
| | Y4 | 2.5948 | 0.6092 | 3.0465 | 0.8484 | 5.2468 | 2.4389 |

where s is the step size and k is the number of steps. For each step k , $\check{\theta}_{ij}(k)$ is obtained by solving the linear system

$$\sum_{\tau} A_{ij}^{(\tau)} \check{\theta}_{ij}(k) = B_{ij}^{(\tau)}(k), \quad (\text{D4})$$

where

$$A_{ij}^{(\tau)} = \delta_{ij} - \frac{1}{2} s \rho_i \check{Q}_{ij}(0), \quad (\text{D5})$$

and

$$B_{ij}^{(\tau)}(k) = \frac{b_{ij}}{2\pi} + \left(1 - \sum_{\tau} \rho_i \bar{Q}_{ij}\right) ks - \sum_{\nu} \frac{C_{vij}}{2\pi} e^{-z_{\nu} ks} + \frac{1}{2} s \sum_{\tau} \rho_i \sigma_{il} g_{il}(\sigma_{il}) \check{Q}_{ij}(k) + s \sum_{m=1}^{k-1} \rho_i \check{\theta}_{il}(m) \check{Q}_{ij}(k-m), \quad (\text{D6})$$

with \bar{Q}_{ij} given by Eqs. (45) and the RDF contact values $g_{ij}(\sigma_{ij})$ given by Eq. (31). If significant differences appear between $\theta_{ij}(r)$ and $\theta_{ji}(r)$, a smaller step size s should be used.

APPENDIX E

For multicomponent mixtures with a multi-Yukawa closure in the MSA, it is shown here that if the amplitudes K_{vij} of any Yukawa tail ν satisfy $K_{vij} = \pm \sqrt{K_{vii} K_{vjj}}$ then the parameters D_{vij} of the factor correlation functions $Q_{ij}(r)$ associate themselves into n groups of n variables each, according to $D_{v1i}/K_{v1i} = D_{v2i}/K_{v2i} = \dots = D_{vni}/K_{vni}$, for $i = 1, 2, \dots, n$. This relation arises independently of the amplitudes $K_{\tau ij}$ of all the other Yukawa tails.

After making the appropriate substitutions, one can write Eq. (8) outside the core [see the intermediate step Eq. (16)] as

$$\sum_{\tau} \left(\delta_{ij} - \rho_i \hat{Q}_{vij} \frac{K_{vil}}{K_{vij}} \right) D_{vil}^* = 1, \quad (\text{E1})$$

where

$$D_{vij}^* = \frac{D_{vij}}{2\pi K_{vij}}. \quad (\text{E2})$$

Defining the quantities

$$q_{vij} = \delta_{ij} - \rho_i \hat{Q}_{vij}, \quad (\text{E3})$$

Eq. (E1) can be written as

$$\sum_{\tau} q_{vij} \frac{K_{vil}}{K_{vij}} D_{vil}^* = 1, \quad (\text{E4})$$

one equation for each (ij) pair.

Each of the n groups of n “ i ” equations involves only n D_{vil}^* unknowns ($l = 1, 2, \dots, n$), and constitutes an independent system of n linear equations. In each of these systems, the q_{vij} coefficients in the “ j ” equations are the same. Let us assume that the corresponding ratios K_{vil}/K_{vij} are also the same for $i = 1, 2, \dots, n$, i.e.,

$$\frac{K_{vil}}{K_{vij}} = \frac{K_{vml}}{K_{vmj}}, \quad (\text{E5})$$

for any i, m, l, j . In particular, for $i = l$ and $j = m$,

TABLE XI. Scaled D_{ij}^* parameters for the first Yukawa tail.*

| Mixture | x_1 | η | kT/ϵ_{11}^H | D_{111}^* | D_{112}^* | D_{121}^* | D_{122}^* |
|-----------------|-------|--------|----------------------|-------------|-------------|-------------|-------------|
| M1 ^b | 0.25 | 0.34 | 1.40 | 0.7831 | 0.8400 | 0.7858 | 0.8395 |
| | 0.50 | 0.34 | 1.40 | 0.7855 | 0.8395 | 0.7875 | 0.8384 |
| | 0.50 | 0.34 | 1.70 | 0.7802 | 0.8297 | 0.7823 | 0.8286 |
| | 0.75 | 0.44 | 1.70 | 0.6728 | 0.7313 | 0.6746 | 0.7285 |
| M2 ^c | 0.25 | 0.30 | 2.10 | 0.9240 | 0.8505 | 0.9398 | 0.8361 |
| | 0.50 | 0.30 | 1.70 | 0.9094 | 0.8204 | 0.9223 | 0.7846 |
| | 0.50 | 0.40 | 1.70 | 0.8532 | 0.6845 | 0.8746 | 0.6267 |
| | 0.75 | 0.40 | 1.70 | 0.8051 | 0.5745 | 0.8197 | 0.4564 |

* Corresponding to the D_{1ij} values given in Table II.

^b For mixture M1, $K_{112} = -1.0079\sqrt{K_{111}K_{122}}$.

^c For mixture M2, $K_{112} = -1.1690\sqrt{K_{111}K_{122}}$.

$$K_{vij} = \pm \sqrt{K_{vii} K_{vjj}}, \quad (\text{E6})$$

since the cross direct correlation functions must be equal, $K_{vij} = K_{vji}$.

Thus if for a particular Yukawa tail ν all ij pairs satisfy Eq. (E6), then the coefficient matrix in the linear system given by Eq. (E4) is the same for all i groups; as a result, the scaled D_{vij}^* variables associate themselves into n groups of n variables each, according to

$$D_{v1i}^* = D_{v2i}^* = \dots = D_{vni}^*, \quad (\text{E7})$$

for $i = 1, 2, \dots, n$. This relation is specific to each tail ν , and is independent from whether the $K_{\tau ij}$ parameters of other Yukawa tails $\tau \neq \nu$ satisfy the same condition or not.

None of the Yukawa tails in the mixtures studied here complies exactly with Eq. (E6). However, the first tails ($\nu = 1$) in both mixtures satisfy it approximately. For these first tails, Table XI presents the values of the scaled D_{1ij}^* corresponding to the solutions given in Table II. The pairing of these parameters according to Eq. (E7) is evident.

In principle, it may appear advantageous to express the problem in terms of the scaled D_{vij}^* . This has the grave inconvenience, however, of spreading the temperature dependence—now contained exclusively in the $A_{vij}^{(4)}$ coefficients of Eqs. (13) and (14)—throughout the system of equations.

One case in which some relations analogous to Eq. (E6) arise naturally is the use of interaction-specific tails. That is, if tail ν is specific to interaction (1,1) then, for a binary mixture, $\epsilon_{v11} \neq 0$, and $\epsilon_{v12} = \epsilon_{v22} = 0$. In this case, however, Eq. (E1) does not apply since it would have been obtained after dividing by zero. Using the original Eq. (16) instead, one can assure that $D_{v21} = D_{v22} = 0$, but not D_{v12} . Of course, every tail τ specific to the cross interaction (1,2) would affect all $D_{\tau ij}$.

¹ J. S. Rowlinson, *Physica A* **156**, 15 (1989).

² L. S. Ornstein and F. Zernike, *Proc. Acad. Sci. Amsterdam* **17**, 793 (1914).

³ L. Blum and J. S. Høye, *J. Stat. Phys.* **19**, 317 (1978).

⁴ M. Ginoza, *J. Phys. Soc. Jpn.* **54**, 2783 (1985); **55**, 95, 1782 (1986).

⁵ G. Giunta, M. C. Abramo, and C. Caccamo, *Mol. Phys.* **56**, 319 (1985).

⁶ E. Arrieta, C. Jedrzejek, and K. N. Marsh, *J. Chem. Phys.* **86**, 3607 (1987).

⁷ D. Henderson, E. Waisman, J. L. Lebowitz, and L. Blum, *Mol. Phys.* **35**, 241 (1978).

⁸ G. Stell and J. J. Weis, *Phys. Rev. A* **21**, 645 (1980).

⁹ J. Konior and C. Jedrzejek, *Mol. Phys.* **63**, 655 (1988).

- ¹⁰J. W. Perram, *Mol. Phys.* **30**, 1505 (1975).
¹¹R. J. Baxter, *J. Chem. Phys.* **52**, 4559 (1970).
¹²G. Pastore, *Mol. Phys.* **63**, 731 (1988).
¹³J. Konior and C. Jedrzejek, *Mol. Phys.* **55**, 187 (1985).
¹⁴J. Konior and C. Jedrzejek, *Physica A* **161**, 339 (1989).
¹⁵K. S. Shing and K. E. Gubbins, *Mol. Phys.* **49**, 1121 (1983).
¹⁶G. A. Mansoori, N. F. Carnahan, K. E. Starling, and T. W. Leland, *J. Chem. Phys.* **54**, 1523 (1970).
¹⁷A. B. Bhatia and D. E. Thornton, *Phys. Rev. B* **2**, 3004 (1970).
¹⁸M. A. Abramo, C. Caccamo, and G. Giunta, *Phys. Rev. A* **34**, 3279 (1986).
¹⁹C. Hoheisel and R. Zhang, *Phys. Rev. A* **43**, 5332 (1986).
²⁰J. Tobochnik and P. M. Chapin, *J. Chem. Phys.* **88**, 5824 (1988).
²¹F. H. Ree, R. N. Keeler, and S. L. McCarthy, *J. Chem. Phys.* **44**, 3407 (1966).
²²Y. Song, R. M. Stratt, and E. A. Mason, *J. Chem. Phys.* **88**, 1126 (1988).
²³L. L. Lee and D. Levesque, *Mol. Phys.* **26**, 1351 (1973).
²⁴L. Verlet and J. J. Weis, *Phys. Rev. A* **5**, 939 (1972).
²⁵G. D. Scott, *Nature (London)* **188**, 908 (1960).
²⁶W. Götze and L. Sjögren, *Phys. Rev. A* **43**, 5442 (1991).
²⁷W. van Megen and P. N. Pusey, *Phys. Rev. A* **43**, 5429 (1991).
²⁸P. N. Pusey and W. van Megen, *Nature (London)* **320**, 340 (1986); *Phys. Rev. Lett.* **59**, 2083 (1987).
²⁹J. S. Rowlinson and F. L. Swinton, *Liquids and Liquid Mixtures* (Butterworths, London, 1982).
³⁰H. R. Wendt and F. F. Abraham, *Phys. Rev. Lett.* **41**, 1244 (1978); F. F. Abraham, *J. Chem. Phys.* **72**, 359 (1980).
³¹W. G. Hoover and F. H. Ree, *J. Chem. Phys.* **49**, 3609 (1968).
³²L. V. Woodcock, *Ann. N. Y. Acad. Sci.* **371**, 274 (1981).
³³C. A. Angell, J. H. R. Clarke, and L. V. Woodcock, *Adv. Chem. Phys.* **48**, 397 (1981).
³⁴A. K. Doolittle, *J. Appl. Phys.* **22**, 1471 (1951).
³⁵J. J. Ullo and S. Yip, *Phys. Rev. Lett.* **54**, 1509 (1985).
³⁶S. H. Chen and J. S. Huang, *Phys. Rev. Lett.* **55**, 1888 (1985).
³⁷J. R. Fox and H. C. Andersen, *J. Phys. Chem.* **88**, 4019 (1984).
³⁸B. Bernu, J. P. Hansen, Y. Hitawari, and G. Pastore, *Phys. Rev. A* **36**, 4891 (1987).
³⁹J. Rogers and D. A. Young, *Phys. Rev. A* **30**, 999 (1984).
⁴⁰H. C. Andersen and D. Chandler, *J. Chem. Phys.* **57**, 1918 (1972).
⁴¹D. Chandler and H. C. Andersen, *J. Chem. Phys.* **57**, 1930 (1972).